

INVESTIGATIONS OF THE INHOMOGENEITY OF A
POWDER-IN-TUBE Nb₃Sn CONDUCTOR

by

Christopher David Hawes

A thesis submitted in partial fulfillment of the
requirements for the degree of

MASTER OF SCIENCE
(MATERIALS SCIENCE)

at the

UNIVERSITY OF WISCONSIN-MADISON

2000

Acknowledgments

I would like to thank my advisor, David Larbalestier, for his support, patience, and guidance. I would also like to thank him for giving me the opportunity to work in a group with so many accomplishments and resources.

I would like to thank Kim Pierson, my advisor at the University of Wisconsin – Eau Claire for getting me started on this path, and his continued support.

I would like to thank ShapeMetal Innovations (Holland), J.H. Lindenhovius, and Andries den Ouden for donating the multifilamentary PIT wire.

I would like to thank Lance Cooley for helping me get started at ASC, Bill Starch for lending a hand and answering questions whenever necessary, Alex Squiteri for assistance with the inductive critical temperature measurements and heat capacity measurements, Peter Lee for his assistance with the microscopy, and Alex Gurevich for helping interpret the inductive critical temperature and heat capacity data.

I would like to thank Melinda Adams, and Kim Bass, who keep ASC running, and interesting.

I would like to thank Mike Naus for his help and for keeping the atmosphere in the office from getting too serious (sometimes), John Anderson and Robert Huessner for their help and support on getting me started at ASC, George Daniels for useful and interesting discussions, and Chris Pelto for helping me get through my classes and lending an ear.

I would like to thank all my friends (Jen, Matt, Jen, Jim, Erinn, Travis, Laura,, Eric, Fred, Jay, Dave, Jason, Samir, and Reid) for their support throughout my college career, and also making sure I never take myself too seriously.

I would also like to thank my family, especially my parents David and Susan, for their support and understanding, especially throughout my college years.

Table of Contents

<i>Acknowledgments</i>	<i>ii</i>
1. Introduction	1
1.1 Goal and Motivation	1
1.2 Theory of Superconductivity	2
2. Literature Review	17
2.1 A15 Structure	17
2.2 Nb-Sn Phase Diagram	21
2.3 Methods of Manufacturing	25
2.3.1 Vapor Phase A15 Formation (the RCA Process).....	25
2.3.2 Liquid Phase Formation.....	27
2.3.2a The Kunzler Method.....	27
2.3.2b The GE Tape Process.....	30
2.3.3 Solid State Diffusion.....	30
2.3.3a Bronze Process.....	30
2.3.3b External-Sn Process.....	31
2.3.3c Internal-Sn Process.....	34
2.3.3d Sn-Rich Powders.....	37
2.4 Summary	49
3. Investigations of the Inhomogeneity of a Powder-in-Tube Nb₃Sn Conductor	51
3.1 Preparation of Conductor	51
3.2 Experiment	51
3.2.1 Inductive Critical Temperature Measurements.....	52
3.2.2 Heat Capacity Measurements.....	52
3.3.3 SEM-BSE/EDX Measurements.....	52

- 3.3 Results..... 53**
 - 3.3.1 SEM-BSE/EDX Measurements..... 53*
 - 3.3.2 Inductive Critical Temperature Measurements..... 65*
 - 3.3.3 Heat Capacity Measurements..... 70*
- 3.4 Discussion..... 76**
- 3.5 Conclusion..... 80**

- 4. References.....82**

- 5. Appendix..... 86**
 - 5.1 Quantum Design SQUID Magnetometer-
Inductive Critical Temperature Measurements..... 86**
 - 5.2 Quantum Design Physical Properties
Measurements System-Heat Capacity..... 87**

1. Introduction

1.1 Goal and Motivation

Nb₃Sn superconducting composites can now be fabricated in long lengths and with high critical current density using the powder-in-tube, PIT, approach. Their value in magnets has been well demonstrated in their use for high field dipoles [1]. This design starts with NbSn₂ and Cu powder encased in Nb tubes, which are then stacked into a billet and either drawn or extruded to form a multifilamentary wire. PIT conductors using this ECN/SMI route have achieved non-copper J_c values of $>1200 \text{ A/mm}^2$ at 13 T and 4.2 K [2]. The flexibility of the PIT approach is suggested by another recent PIT design, which used a mixture of Nb₆Sn₅ / Nb powder in Ta tubes which were then groove and flat rolled into a tape, which achieved B_{c2} values of 24.7 T at 4.2 K and J_c values of 330 A/mm^2 at 20 T and 4.2 K [3].

PIT wires are interesting for a number of reasons, not least their high J_c values and their magnetically transparent design. As the maximum possible performance is sought in A15 compound wires, we must deal with the difficulty of simultaneously obtaining optimum stoichiometry, fine grain structure, and strain state throughout the whole A15 layer. Since conventional ways (e.g. bronze or internal Sn process) of making Nb₃Sn end with A15 layers that are typically less than 2 μm in thickness, of variable composition and grain morphology, and with a strong precompression from the bronze around each filament, it is seldom clear how much of each filament is actually carrying current, particularly at high fields. PIT conductors have several potential advantages for resolving such issues. One is that their “inside-out” design makes them magnetically transparent, since the highest T_c shell is on the

inside, exposing the T_c gradient to magnetic measurements. The second is that the precursor Sn-rich NbSn₂ phase of the core reacts rapidly to make an A15 layer that is thick enough to permit quantitative chemical analysis. A third advantage is that the Nb filament shell has a low thermal contraction coefficient, which is well matched to that of the Nb₃Sn, thus minimizing T_c and B_{c2} precompression effects applied by the continuous Cu matrix.

The specific heat measurements of A15 compounds found in the literature largely consist of measurements performed on bulk samples manufactured as close to stoichiometry as possible. These measurements are performed to determine such things as the Sommerfield Constant, Debye Temperature, and the electron density of states. In this experiment, heat capacity measurements were performed on a conductor with a known composition gradient to determine the homogeneity of the A15 layer. The data obtained in the heat capacity measurements is then compared with that from SEM analysis and inductive critical temperature measurements.

The rest of section 1 is a brief overview of the theory of superconductivity. Section 2 discusses the structural properties of A15 compounds, the Nb-Sn phase diagram, and different methods used to manufacture A15 conductors. In section 3 heat capacity measurements, inductive critical temperature measurements, and scanning electron microscopy are used to identify and characterize the composition and critical temperature gradient in a Nb-Sn PIT conductor.

1.2 Theory of Superconductivity

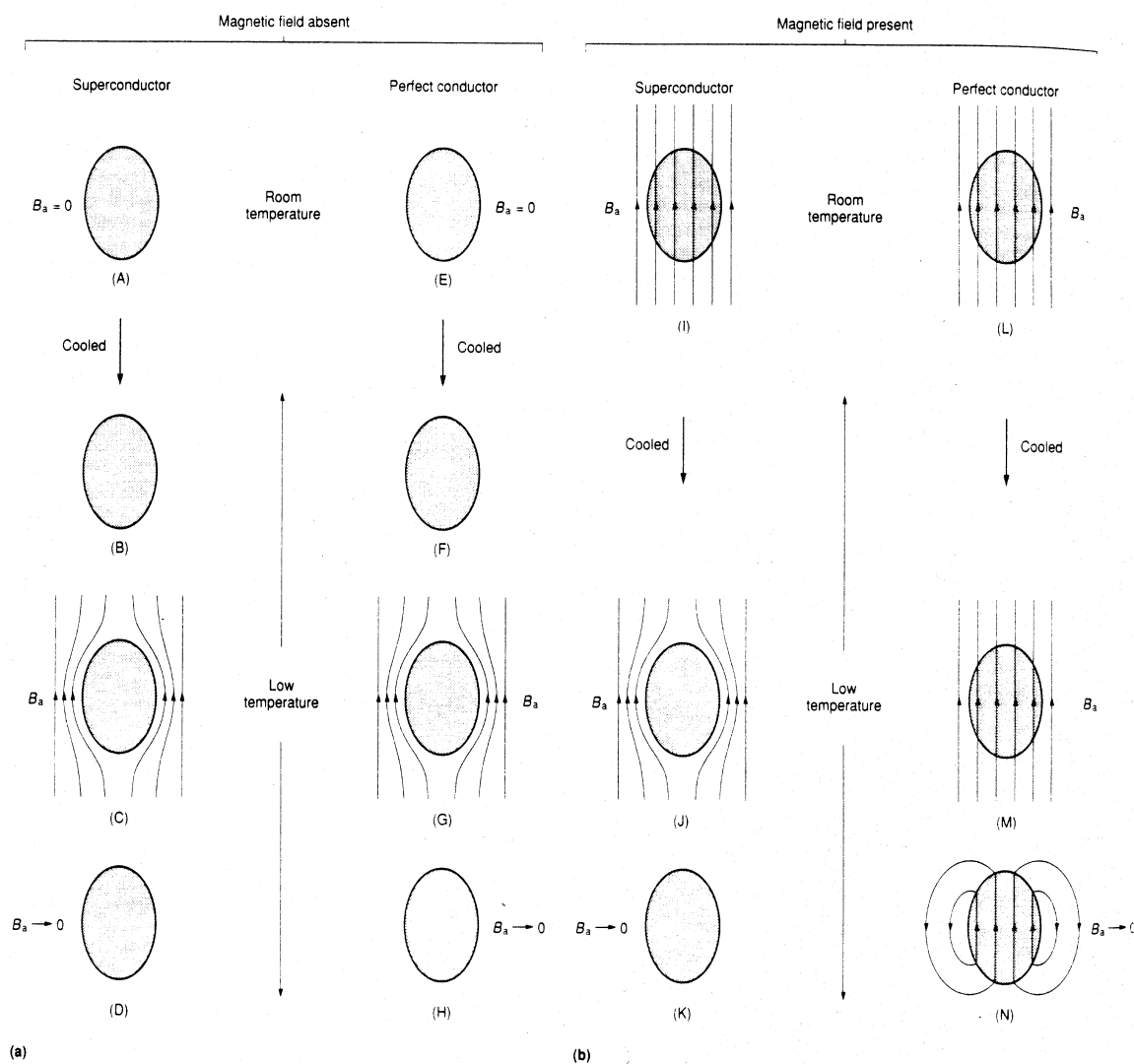


Fig. 1.1 Comparison of the magnetic field behavior of a superconductor to that of a perfect conductor. In (a), magnetic flux exclusion occurs in both a perfect conductor and superconductor when first cooled and then exposed to a magnetic field. In (b), exclusion occurs only in the superconductor (I, J, and K), when exposed to a field and then cooled. In a perfect conductor (L, M, and, N) the field is trapped when exposed to a field and then cooled [4].

This section is a general overview of the theory of superconductivity. Much of the information in this section was obtained from Lynton [5] and Tinkam [6], two excellent sources for information on the general theory of superconductivity.

In 1911 H. K. Onnes discovered that the electrical resistance of mercury disappeared when it was cooled to about 4 K. The disappearance of electrical resistance at some critical temperature, T_c , is one of the three critical properties of a superconductor. The second critical property, discovered by Meissner and Ochsenfeld in 1933, is that bulk superconductors display perfect diamagnetism, perfect diamagnetism occurs when a superconductor is cooled below T_c in a magnetic field. As long as the magnetic field is below some critical field, H_c , then all magnetic flux will be expelled from the superconductor. Fig. 1.1 is schematic diagram showing the difference between a perfect conductor and a superconductor. Both shield flux when a magnetic field is applied after being cooled below T_c , but a superconductor will expel flux if the field is applied and then cooled below T_c , whereas a perfect conductor will trap the flux if cooled below T_c after the field is applied. The temperature dependence of H_c is expressed in Eq. 1.1,

$$H_c \approx H_c(0) \left[1 - (T/T_c)^2 \right] \quad (1.1).$$

The reason for complete flux exclusion is that circulating supercurrents are induced on the surface of the superconductor. The supercurrent flows in such a direction as to create a magnetic field which opposes the applied magnetic field. Thus the applied field within the superconductor is nulled. The supercurrent flows on the surface of the superconductor to a

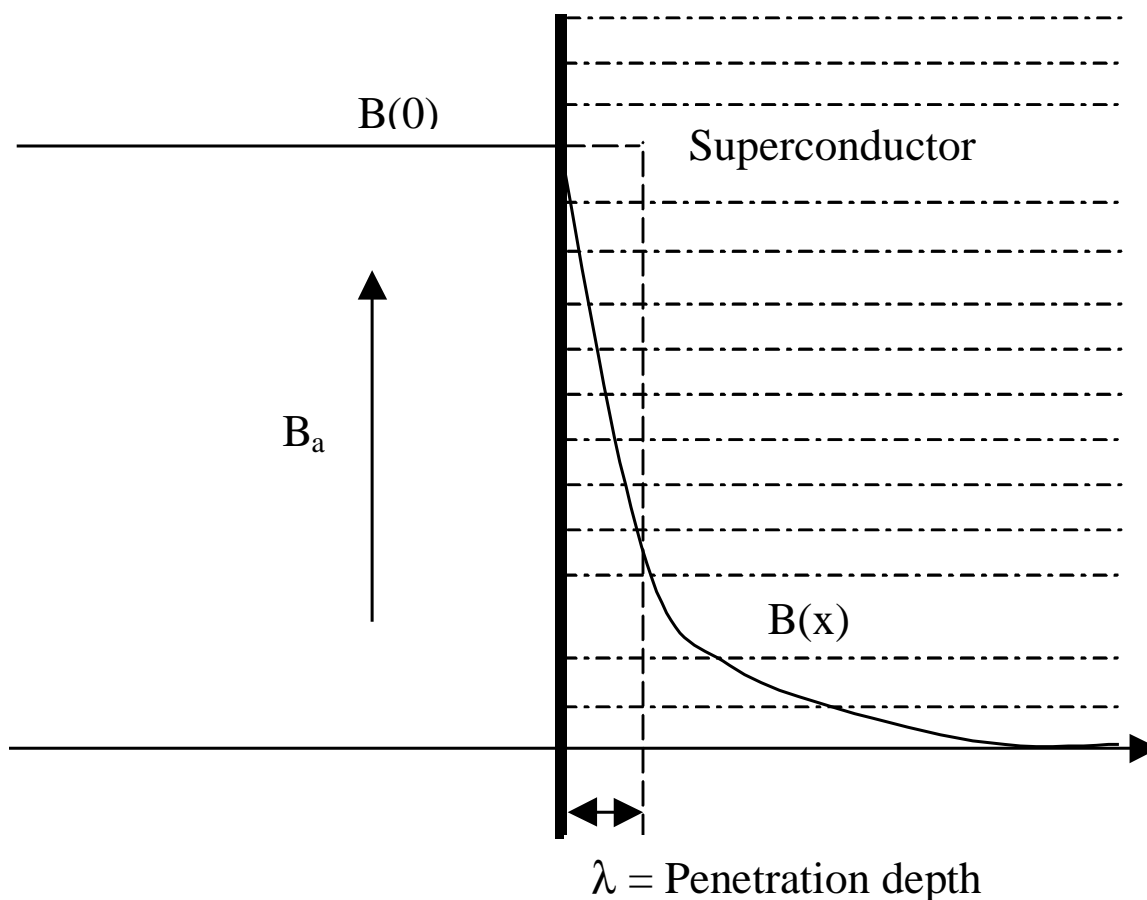


Fig. 1.2 Current flows on the surface of a superconductor in a direction that creates a magnetic field that opposes the applied field B_a and excludes this field from entering the superconductor. The penetration depth λ is the depth that the surface current penetrates the superconductor.

finite thickness, shown in Fig. 1.2, whose magnitude is the penetration depth λ , typically $0.01 \mu\text{m}$ to $0.5 \mu\text{m}$.

The third critical property of a superconductor is the critical current density, J_c . J_c is the maximum current density, amps per unit area, a superconductor can carry before dissipation occurs.

When these three critical properties, J_c , T_c , and H_c , are plotted on a three-dimensional graph they make up a surface known as the critical surface, Fig. 1.3. Below the critical

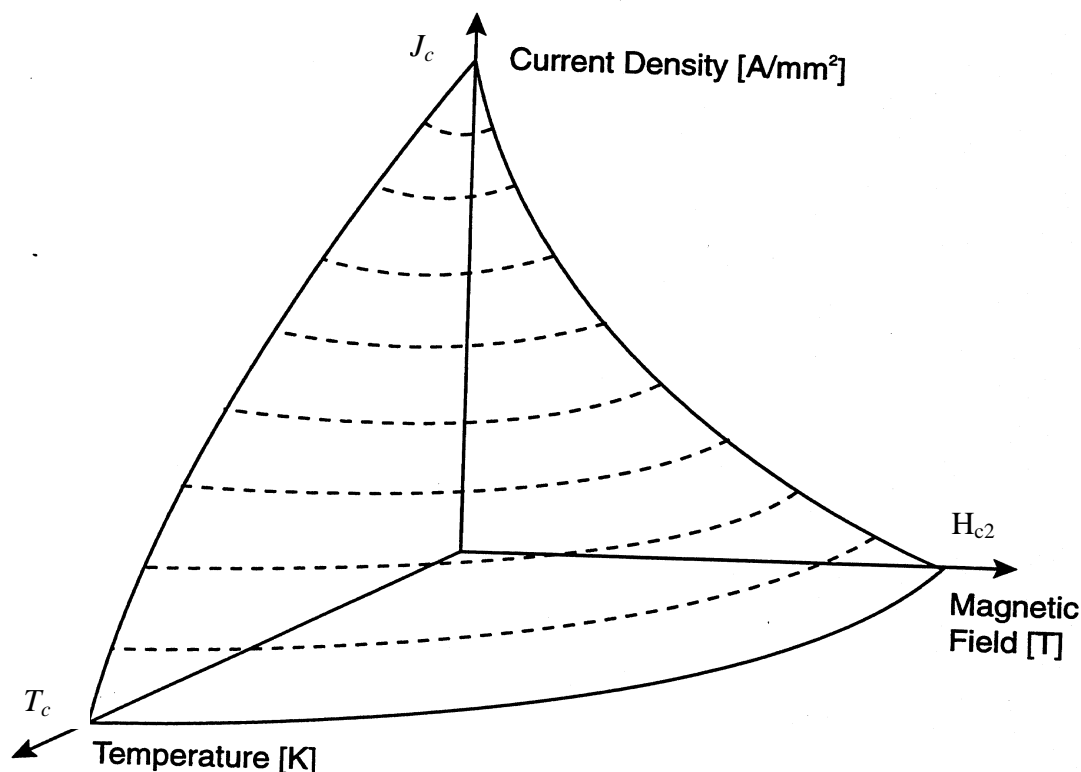


Fig. 1.3 Representation of the critical surface of a superconductor [7].

surface the material is superconducting and above the critical surface the material becomes dissipative. All three properties depend upon one another. The higher the temperature, or field, the lower the J_c .

There are two general types of superconductors, type I, the type discovered by Onnes, and type II, discovered by Shubnikov, the type which is used for most engineering purposes. Both types of superconductors obey the same microscopic theory developed by Bardeen, Cooper, and Schrieffer, BCS theory, in 1957. In the BCS theory, electrons at the Fermi level with equal and opposite spin and momentum condense into electron-electron pairs, known as Cooper pairs, below T_c . The attractive interaction of electrons occurs by an exchange of a

virtual phonon between electrons and intervening ions. The distance over which this interaction occurs is known as the coherence length, ξ_0 . ξ_0 is a strongly variable property of the superconductor, ranging from as little as 1 nm in high temperature superconductors to ~3 nm for Nb₃Sn, 5 nm for Nb47wt.%Ti to ~0.5 μ m for type I superconductors. The formation of Cooper pairs results in a decrease in the potential energy of the electron pair greater than the increase in the pair kinetic energy, which results in the formation of an energy gap that must be overcome to break the Cooper pair. This energy gap is

$$E_g(0) = 2\Delta(0) = 3.5kT_c \quad (1.2),$$

for $T/T_c \equiv t \rightarrow 0$.

Prior to BCS theory, F. and H. London described the microscopic electric and magnetic fields, within a superconductor using phenomenological electrodynamics

$$\mathbf{E} = \delta/\delta t(\Lambda \mathbf{J}_s) \quad (1.3),$$

$$\mathbf{h} = -c \text{curl} (\Lambda \mathbf{J}_s) \quad (1.4),$$

where

$$\Lambda = 4\pi\lambda_L^2 / c^2 = m / n_s e^2 \quad (1.5)$$

is a phenomenological parameter, n_s is the density of superconducting electrons, \mathbf{J}_s is the superconducting current density, and λ_L is the superconducting penetration depth. Equation

1.3 describes the perfect conductivity property of the superconducting state, and, when the Maxwell equation

$$\text{curl } \mathbf{h} = 4\pi\mathbf{J} / c \quad (1.6)$$

is applied to equation 1.4, this leads to

$$\nabla^2 \mathbf{h} = \mathbf{h} / \lambda^2 \quad (1.7).$$

The solution [6] to equation 1.7 for a semi-infinite slab is

$$\mathbf{h}(x) = \mathbf{h}(0)\exp(-x/\lambda) \quad (1.8),$$

which for $x \gg \lambda$, $\mathbf{h}(x) \approx 0$. This implies that the applied magnetic field is screened from the interior of the sample, as required by the Meissner effect. F. London then combined these two equations to obtain

$$\mathbf{J}_s = n_s e \langle \mathbf{v}_s \rangle = -n_s e^2 \mathbf{A} / mc = -\mathbf{A} / \Lambda c \quad (1.9),$$

where $\langle \mathbf{v}_s \rangle$ is the local average electron velocity in the presence of a field and \mathbf{A} is the London gauge, which is specified by requiring that $\text{div } \mathbf{A} = 0$ (so $\text{div } \mathbf{J} = 0$).

Using equation 1.9, Pippard developed the phenomenology further, introducing a second characteristic length, ξ_0 . ξ_0 describes the wavelength over which the superconducting electron pair varies from the uncertainty-principle as

$$\xi_0 = a(hv_F / kT_c) \quad (1.10),$$

where a is a numerical constant of order unity and v_F is the Fermi velocity. His experiments with dilute alloys of indium in tin lead to the discovery that a decrease in the normal electron mean free path, l , leads to an increase in the penetration depth. Pippard developed the following relation

$$\lambda = \lambda_L \sqrt{\frac{\xi_0}{\xi(l)}} \quad (1.11),$$

where λ_L is the penetration of the pure superconductor, ξ_0 is the coherence length of the pure superconductor, and $\xi(l)$ is the penetration depth of the alloyed superconductor, which is expressed as

$$1/\xi(l) = 1/\xi_0 + 1/\alpha l \quad (1.12),$$

where α is a constant of order unity.

Ginzburg-Landau introduced a complex wave function, ψ , as an order parameter for superconducting electrons, such that, the local density of superconducting electrons is given by

$$N_s = |\psi(x)|^2 \quad (1.13).$$

From the GL theory comes the temperature dependent coherence length

$$\xi(T) = \hbar / 2\pi |2m^* \alpha(T)|^{1/2} \quad (1.14),$$

which characterizes the distance over which the order parameter can vary without an increase

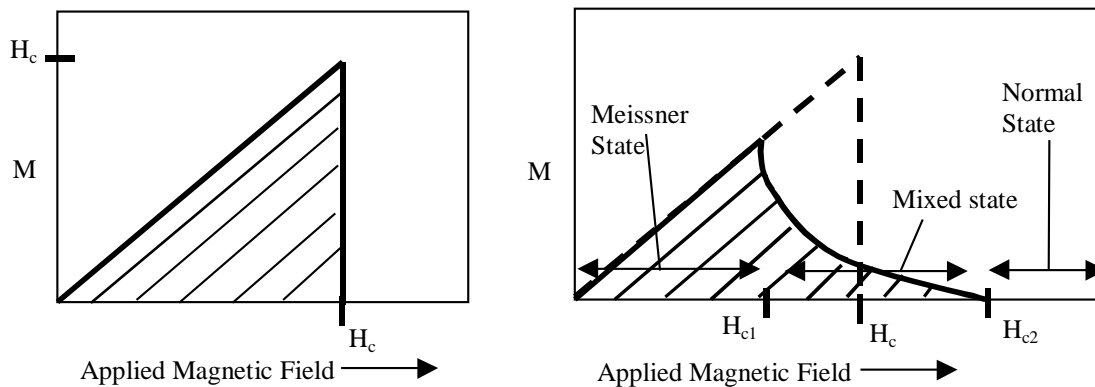


Fig. 1.4 Magnetization plots for a Type I superconductor, left, and Type II superconductor, right. The vertical axis, M , is the measured sample magnetization and the horizontal axis is the applied field. In the Type I superconductor complete flux exclusion, the Meissner effect, occurs up to some critical field H_c at which point flux enters and the material becomes a normal conductor. In the Type II superconductor the Meissner effect occurs up to some critical field H_{c1} , at this point flux enters the sample. The state when flux has penetrated the sample is known as the mixed state. As the applied field is increased more flux enters the sample until H_{c2} , at which point the sample is fully penetrated by field and becomes a normal conductor [4].

in energy. In a pure superconductor, when $T \ll T_c$, ξ behaves like the Pippard coherence length, equation 1.10, but near T_c the behavior is that of equation 1.14. The ratio of the penetration depth and the coherence length gives what is known as the Ginzburg-Landau parameter, or κ . It was discovered for type I superconductors that κ is

$$\kappa = \lambda / \xi < 1 / \sqrt{2} \quad (1.15).$$

For this condition the interface between the superconducting and normal regions has a positive surface energy and all flux is expelled from the superconductor up to a critical field H_c , above H_c the material becomes dissipative. Ginzburg-Landau investigated solutions for $\kappa \gg 1$, but rejected them as unphysical. Abrikosov later solved these equations for $\kappa \gg 1$, finding that the superconductor, by the formation of a triangular vortex lattice, would have negative surface energy. The negative surface energy maximizes the normal to superconductor interface area and causes the free energy to decrease instead of increase, like in a type I superconductor. In a type II superconductor the maximization of the normal to superconductor interface area results in full flux exclusion up to some critical field H_{c1} , which is lower than the thermodynamic critical field H_c . Flux enters the sample as quantized flux vortices or fluxons, maintaining the bulk superconducting state up to an upper critical field H_{c2} , which is higher than H_c . The magnetization curves in Fig. 1.4 show the difference between type I and type II superconductors, and how H_c , H_{c1} , and H_{c2} , are related. The relationship between n_s , the superconducting electron density, λ , and ξ , for a single fluxon are schematically displayed in Fig. 1.5. The state between H_{c1} and H_{c2} is known as the mixed

state, and the fluxons, modeled as cylindrical shells of superelectrons with a normal core and diameter 2ξ , form a triangular lattice with spacing

$$d_{\text{FLL}} = \sqrt{\frac{2\phi_0}{\sqrt{3}H_{\text{applied}}}} \quad (1.16),$$

where ϕ_0 is the magnetic flux associated with a single fluxon (2.067×10^{-15} Wb) and the field is in Tesla. H_c and H_{c2} are related by

$$H_{c2} = \sqrt{2} \kappa H_c, \quad (1.17),$$

and ξ and H_{c2} are related by

$$H_{c2} = \phi_0 / 2\pi\xi^2 \quad (1.18).$$

Shubnikov experiments, from the 1930's, and Abrikosov's theory, from the 1950's, both described and confirmed the existence of type II superconductor and the mixed state.

Fig. 1.6 is a schematic representation of the flux line lattice. If current is applied perpendicular to the applied magnetic field then a Lorentz force, Eq. 1.19, is exerted on the vortices in the superconductor,

$$\mathbf{F}_L = \mathbf{J} \times \mathbf{B}_a, \quad (1.19).$$

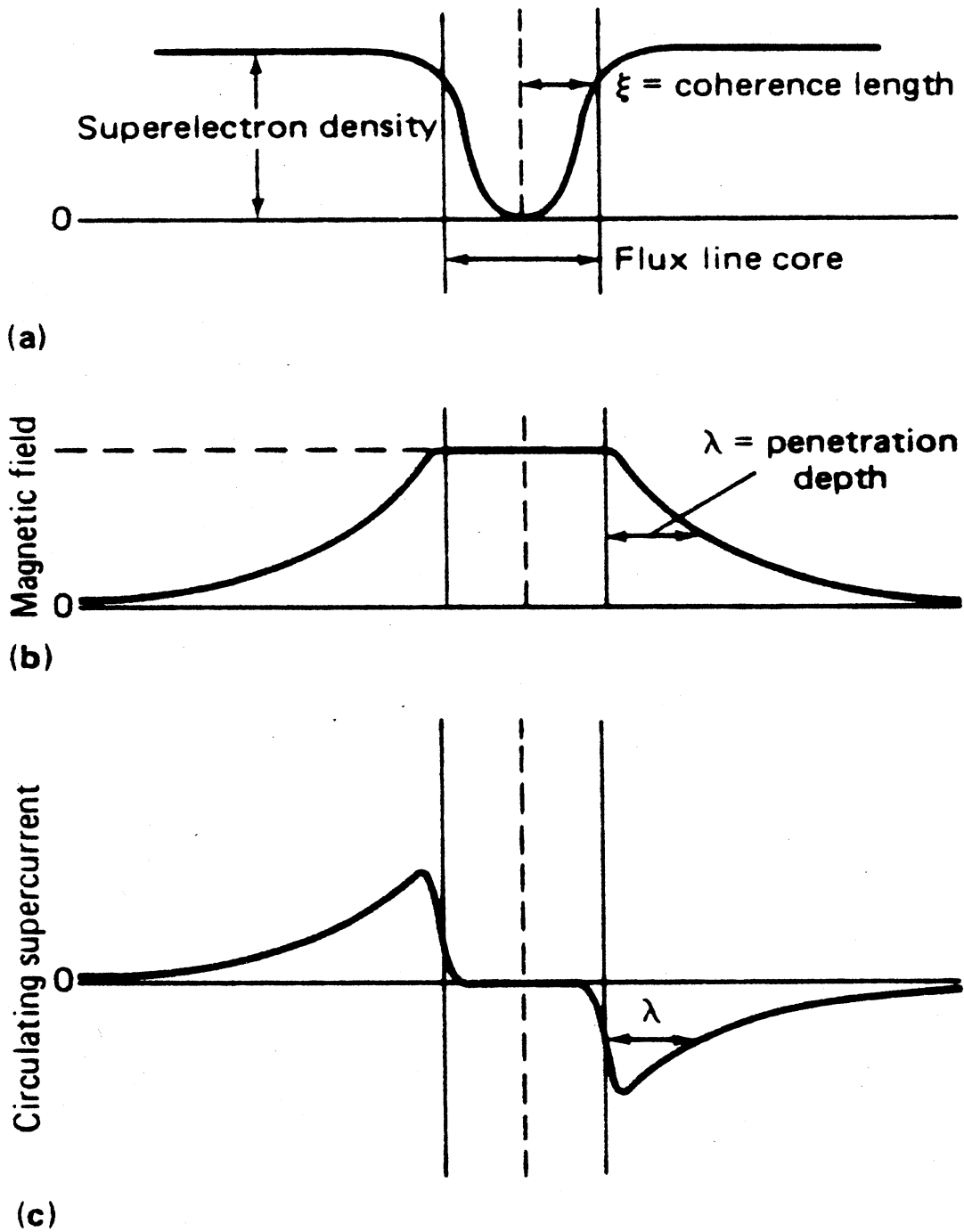


Fig. 1.5 Schematic diagram showing the different aspects of a single fluxon. (a) superelectron density of the fluxon. The maximum superelectron density is almost reached within a coherence length of the center of the core. (b) The magnetic field of the fluxon falls off within a penetration depth. (c) The magnetic field in the core is generated by the circulating supercurrent flowing within a penetration depth of the core [4].

The Lorentz force is resisted by the pinning force exerted by lattice defects, which anchor the fluxons. By Maxwell's equation, a bulk current requires a flux density gradient across the superconductor. This bulk current is the net current arising from the local vortex density gradient. The magnitude of the local current density around each vortex is the depairing critical current density, J_d . J_d occurs when the kinetic energy of the Cooper pair exceed Δ , and sets the absolute limit on the current a superconductor may carry. In BCS theory J_d is expressed as

$$J_d = \sqrt{\frac{2n_s^2 \Delta e^{*2}}{m^{*2}}} \quad (1.20),$$

and in G-L theory as

$$J_d = .544 \frac{H_c}{\lambda} \quad (1.21).$$

The depairing critical current density cannot be reached uniformly throughout the superconductor and is much greater than the depinning critical current density. Optimum flux pinning approaches 5-10% of J_d .

There are two general interactions which lead to flux pinning, [8] one with the vortex core and one through the interaction with vortex screening currents, the magnetic mechanism. As mentioned earlier, the fluxon can be modeled as a cylindrical shell of superelectrons surrounding a normal core, in which a condensation energy of the superconducting state must be destroyed. A portion of this energy can be conserved if the

fluxon passes through a region of material that is already normal, thus providing pinning. The ideal size of this material would be on the order twice the coherence length or the diameter of the fluxon. Pinning by this mechanism is known as core pinning. Inhomogeneities, such as interfaces, which perturb the current distribution of the fluxon also introduce a position dependence of the free energy, because the free energy of the fluxon is not only dependent upon the condensation energy of the core, but also the magnetic field energy and the kinetic energy of the Cooper pairs. Pinning by inhomogeneities which reduce the magnetic free energy of the fluxon is known as magnetic pinning.

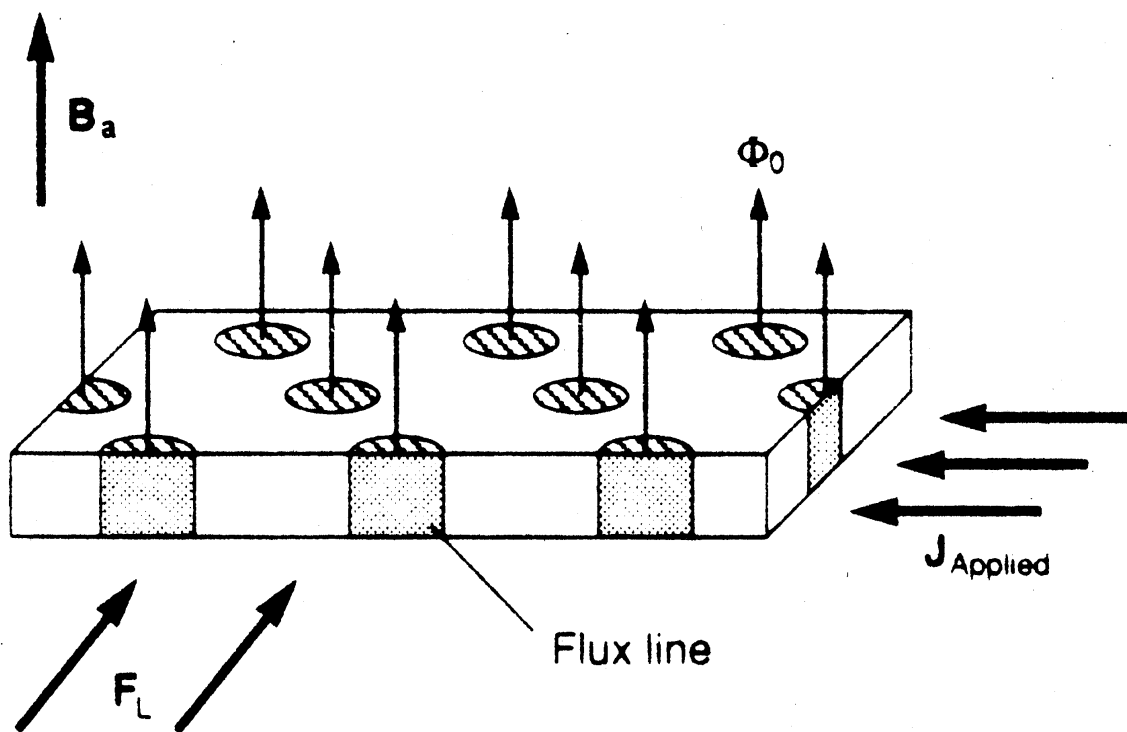


Fig. 1.6 Flux lattice in a Type II superconductor. Applied current, J_{Applied} , and field, B_a , result in a Lorentz force, $F = J_{\text{applied}} \times B_a$, that causes the fluxons to move through the superconductor. If the applied current or field is great enough flux motion will occur. J_c is determined by the condition $F_L = -F_p$, if F_L exceeds F_p flux motion and dissipation above J_c occurs [4].

2. Literature Review

2.1 A15 Structure

The generic formula structure of the A15 compounds is represented as A_3B , where the B atoms are arranged like a body centered cubic crystal with an additional two A atoms centered on every face, Fig. 2.1. In the commercially viable A15 compounds, A is usually a transition metal (Nb or V) and B is usually a Group III or Group IV element (Sn, Al, or Ga). Matthias has shown that the average electron-to-atom ration (e/a) is about 4.75 when the

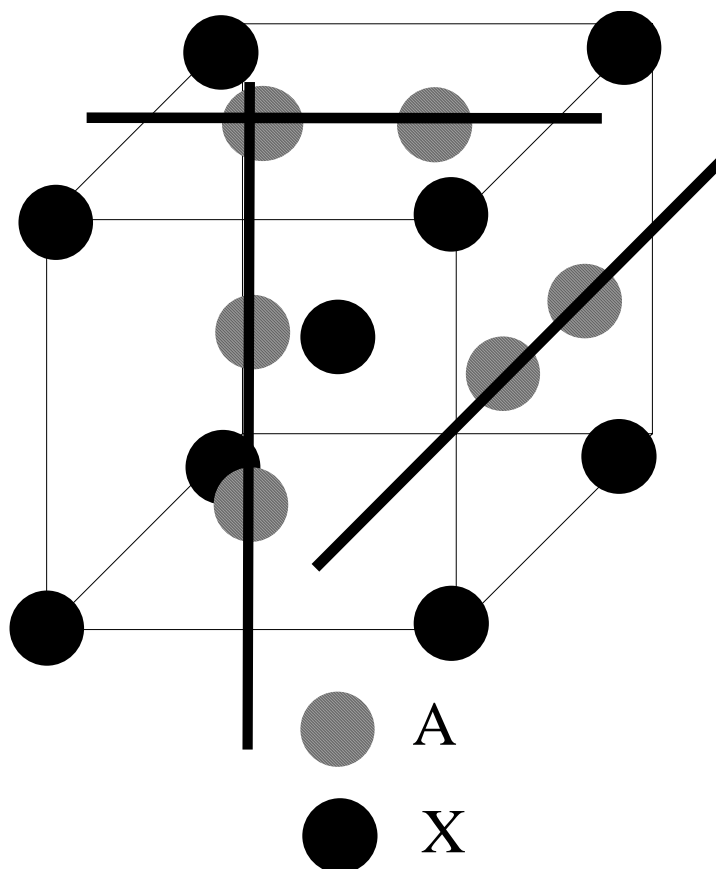


Fig. 2.1 Schematic representation of the A15 structure. X atoms are located on the BCC sites and the A atoms are located on the cube faces. A-A bonds are shorter than in pure A.

valence of the A atom is 5 and that of the B atom is 4. This combination of A and B atoms gives a maximum T_c of about 18.2 K for Nb_3Sn , Fig. 2.2 [9].

The A atoms in the A15 compounds are arranged in three linear orthogonal chains, with the A atoms 10 to 15% closer to each other than when found in the A metal [10]. The arrangement, ordering and distance, of the A atoms, with respect to each other, causes an increase in the d -band density of states, over that found in the A metal. This increase in density of states is related to the superconducting properties of the A15 compounds [11]. Disorder in the A15 lattice, particularly at the A site, will cause a decrease in the d -band density of states and a consequent degradation of the superconducting properties. Neutron irradiation studies of Nb_3Sn wire have shown the long range order parameter to drop to ~ 0.93 with a resulting 20% decrease in the critical temperature [12]. The long-range order

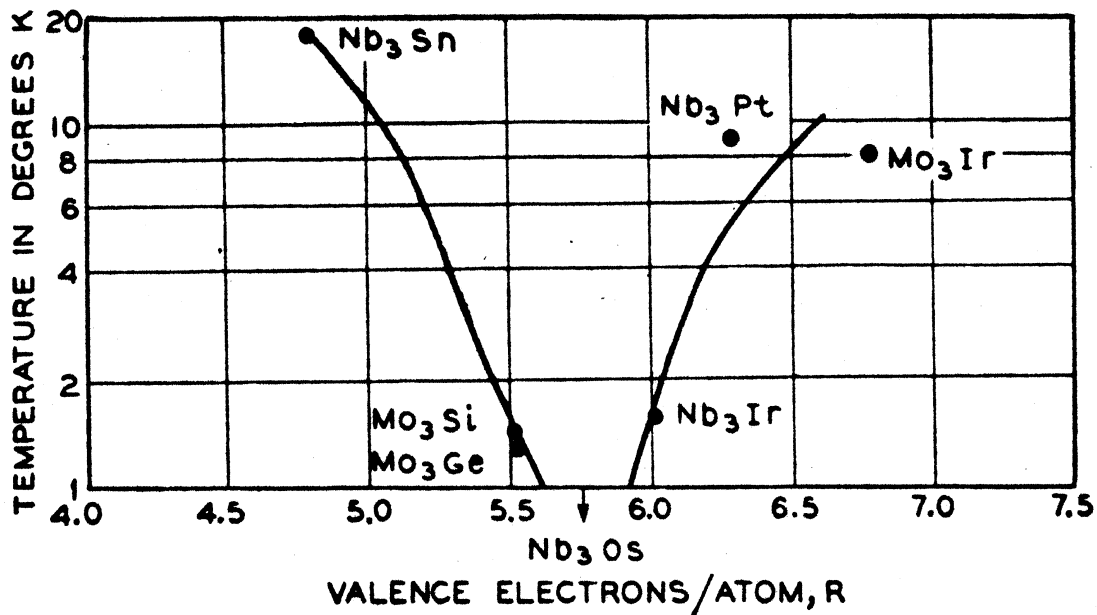


Fig. 2.2 Comparison of the critical temperature as a function of the average electron-to-atom ratio for several A15 compounds [9].

parameter is defined as:

$$S = \frac{r_A - F_A}{1 - F_A} \quad (1.20)$$

where r_A is the fraction of A sites occupied by A atoms, and F_A is the fraction of A atoms in the alloy. When the long-range order is perfect, $r_A = 1$ by definition, and $S = 1$. When the atomic arrangement is completely random, $r_A = F_A$ and $S = 0$ [13]. Junod et al. [14] have

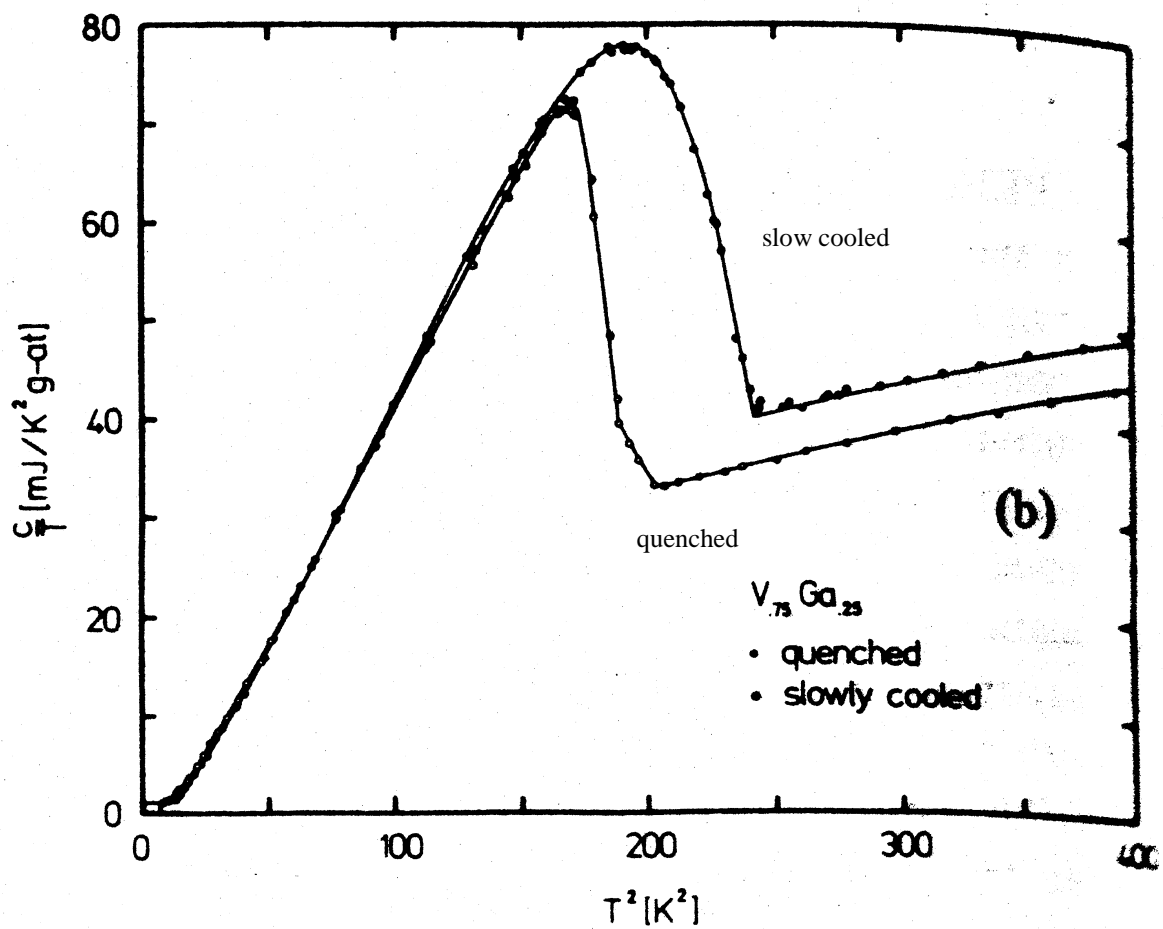


Fig. 2.3 Specific heat curves for V_3Ga that has been quenched and slowly cooled. The right-hand curve, displaying a higher T_c , is the slowly cooled and the left-hand curve is the quenched. The quenched sample is more disordered than the slowly cooled sample [14].

shown that the T_c in quenched V_3Ga is 1.1 K lower than in slow cooled V_3Ga , and that this variation is due to disorder in the lattice, Fig. 2.3. Flukiger and Jorda [15] performed a series of heat treatments and cool downs on Nb_3Ga and V_3Ga which separated the two variables, disorder and compositional variations, and showed that each affected T_c separately. In Nb_3Ga , T_c decreased as much as 1 K for disordering and as much as 10 K when there was only 20% Ga in Nb_3Ga , Figs. 2.4 and 2.5.

The A15 compounds have a low temperature martensitic phase transformation. Nb_3Sn displays a cubic to tetragonal phase transformation at approximately 43 K [16] and only at compositions above 24.5 at.% Sn [17]. Superconductivity occurs in both the tetragonal and cubic phases, but is depressed in the tetragonal phase. Devantay et al. [17]

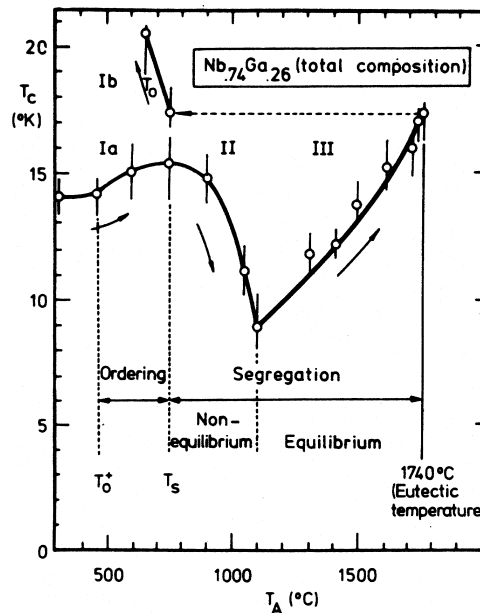


Fig. 2.4 The variation of T_c as a function of heat treatment temperature. Region I represents the region where long range ordering dominates. Region III represents the region where composition dominates. Region II is the mixed region. T_0 and T_s are the minimum ordering and segregation temperatures [15].

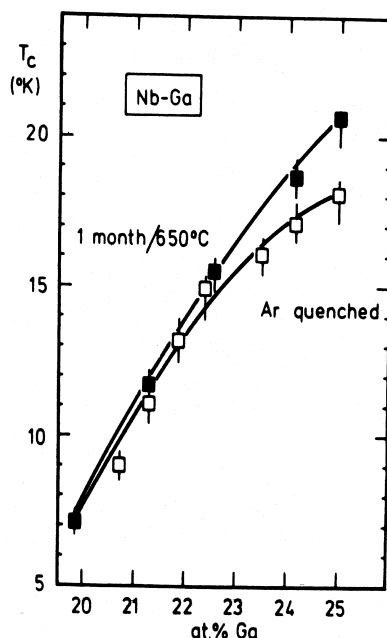


Fig. 2.5 Variation of T_c as a function of at.% Ga in the Nb-Ga A15 compound [15].

produced a range of bulk Nb-Sn A15 samples which displayed increasing T_c up to ~18 K at ~24.5 at.% Sn, at which point a shift to the tetragonal phase caused the T_c to decline to ~17 K, but T_c did climb back to ~18 K at the stoichiometric Nb-Sn composition.

2.2 Nb-Sn Phase Diagram

Fig. 2.6 shows the accepted Nb-Sn phase diagram from Charlesworth et al. [18], while Fig. 2.7 shows an earlier phase diagram from Shunk [19]. The phase diagram from Shunk shows the A15 phase to be unstable below ~775 °C. The phase diagram of Charlesworth shows the A15 phase to be stable at low temperatures, as is known to be the case, so this phase diagram is the one generally used for Nb-Sn. Both diagrams show no solid solubility of Nb in Sn. Charlesworth shows a maximum solubility of 9 at.% Sn in Nb at

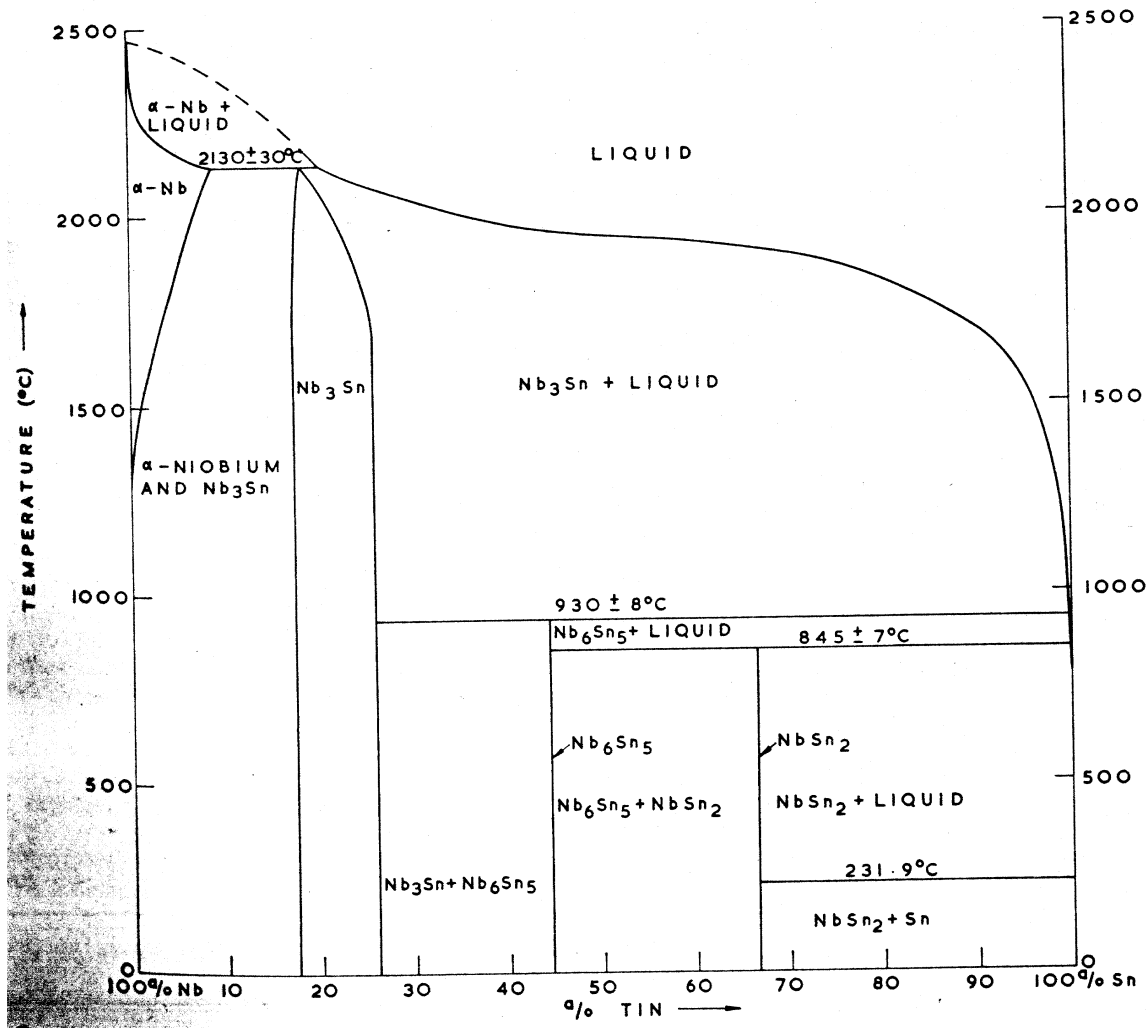


Fig. 2.6 Nb-Sn phase diagram [18].

the A15 peritectic temperature of 2130 °C. Below 2130 °C the solubility decreases to 1 at.% Sn at 1495 °C and eventually the Sn becomes insoluble below ~1300 °C.

Shunk shows a maximum solubility of 10-12 at.% Sn in Nb at the A15 peritectic, with solubility decreasing to about 2 at.% Sn below 1000 °C, but never becoming insoluble. The A15 phase forms peritectically at 2130 °C. The A15 phase field in Charlesworth extends from about 17 to 27 at.% Sn, while in Shunk it extends from about 17 to 25 at.% Sn. Shunk represents both Nb_6Sn_5 and NbSn_2 as phases with varying compositions, and Nb_6Sn_5 as

unstable at low temperature. In Charlesworth's diagram both Nb_6Sn_5 and NbSn_2 are line compounds, stable at low temperature, which form peritectically, Nb_6Sn_5 at $930\text{ }^\circ\text{C}$ and NbSn_2 at $845\text{ }^\circ\text{C}$, and culminate at a eutectic between NbSn_2 and Sn. Charlesworth does comment that many investigators find the NbSn_2 phase to be more Nb rich than stoichiometric, possibly up to $\sim 38\text{ at.}\%$ Nb.

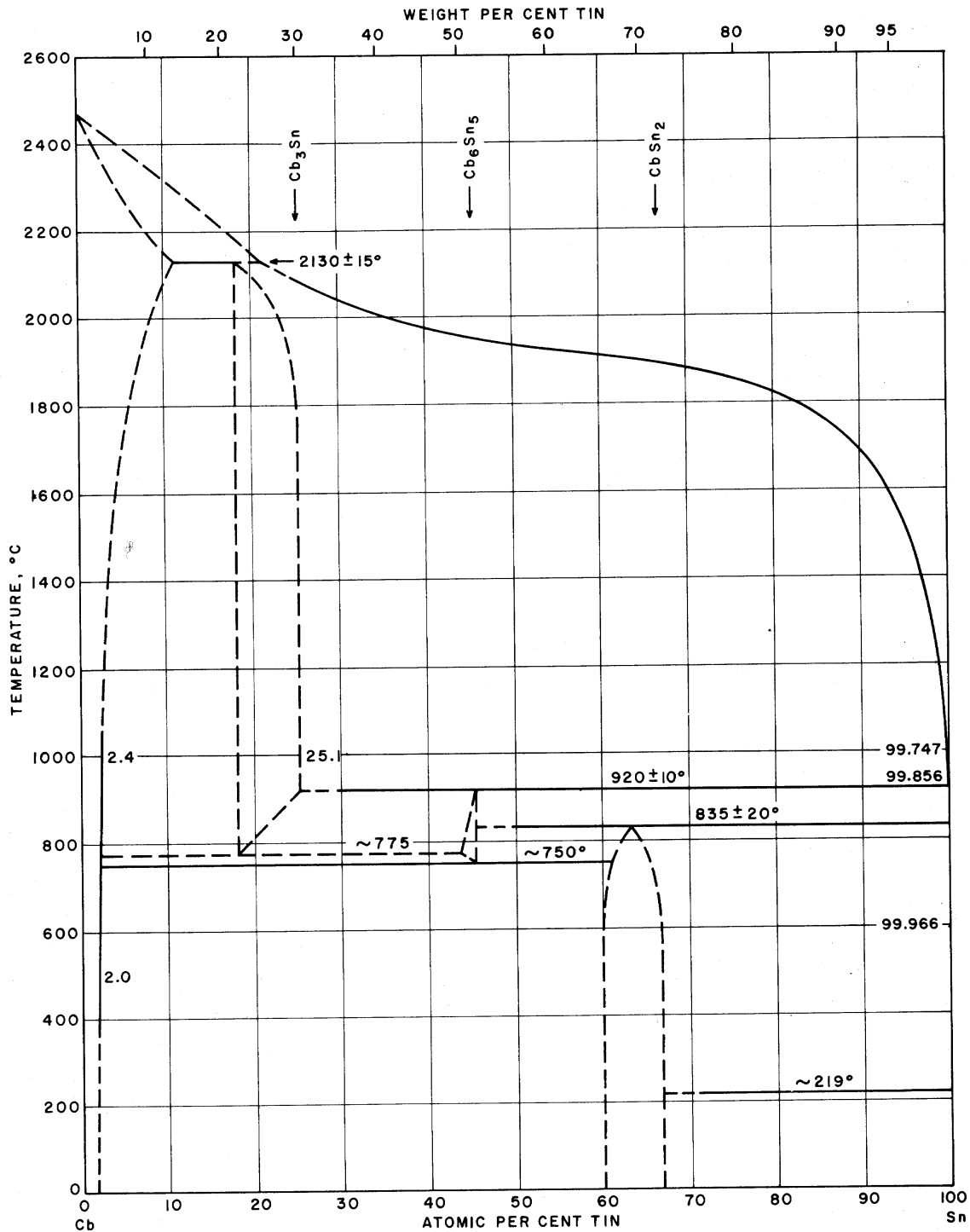


Fig. 2.7 Nb-Sn phase diagram from Shunk [19]. Note the absence of the Nb₃Sn phase field below ~775 °C, there is no Nb₆Sn₅ phase field below ~750 °C, and Nb₆Sn₅ and NbSn₂ are not line compounds.

2.3 Methods of Manufacturing A15 Conductors

The A15 phase can be formed by either vapor, liquid, or solid state diffusion methods. This section gives an overview of the processes used to form the A15 phase. Each of these processes uses one of three mechanisms mentioned above to form the A15 phase. Also, the performance (i.e. J_c , H_{c2} , T_c , etc.) of some of the materials are given for comparison.

2.3.1 Vapor Phase A15 Formation (*the RCA Process*)

In the early 1960s RCA developed a process for the deposition of Nb₃Sn from the hydrogen reduction of niobium and tin chlorides. Many different processes [20] have been developed, but the focus here will be on the one used to manufacture useful conductors. The Nb₃Sn was deposited either on a substrate made of Pt, Ni, or Ni alloy, or ceramic substrates made of magnesium silicate. These substrate are used because they have high melting points, are chemically inert, and have coefficients of thermal expansion that match well with the Nb₃Sn. The deposition process consists of the simultaneous hydrogen reduction of niobium and tin chlorides at the substrate surface to form Nb₃Sn. This reaction occurs at temperatures between 900 and 1200 °C. An example of the chemical reaction [21] used to form Nb₃Sn on Hastelloy is given below:



The ratio of the niobium chloride and tin chloride gas which are fed into the chamber is strongly dependent upon the reaction temperature, and the ratio strongly influences the composition of the deposited film. The grown films have a columnar structure with a density

that is 98 to 100% of the theoretical density of Nb₃Sn [22]. The range of critical temperatures for the films grown on ceramic substrates is shown on Fig. 2.8. The zero-field J_c values of these films ranged from 6.3×10^3 A/mm² for a film with 21.6 at.% Sn, to 2.8×10^4 A/mm² for a film with 23.2 at.% Sn. Nb₃Sn has been deposited in this manner on 300 m lengths of a refractory metal substrate [23]. This material displayed properties very similar to those previously mentioned. The critical temperature of the conductor was 17.8 K, ΔT_c 0.3 K, with a J_c of 1×10^4 at ~ 1 T and 4.2 K. The advantages of manufacturing a conductor by this method is that it requires no further treatment of any kind before or after winding it into a solenoid, and the wire can be easily coated with an insulating material.

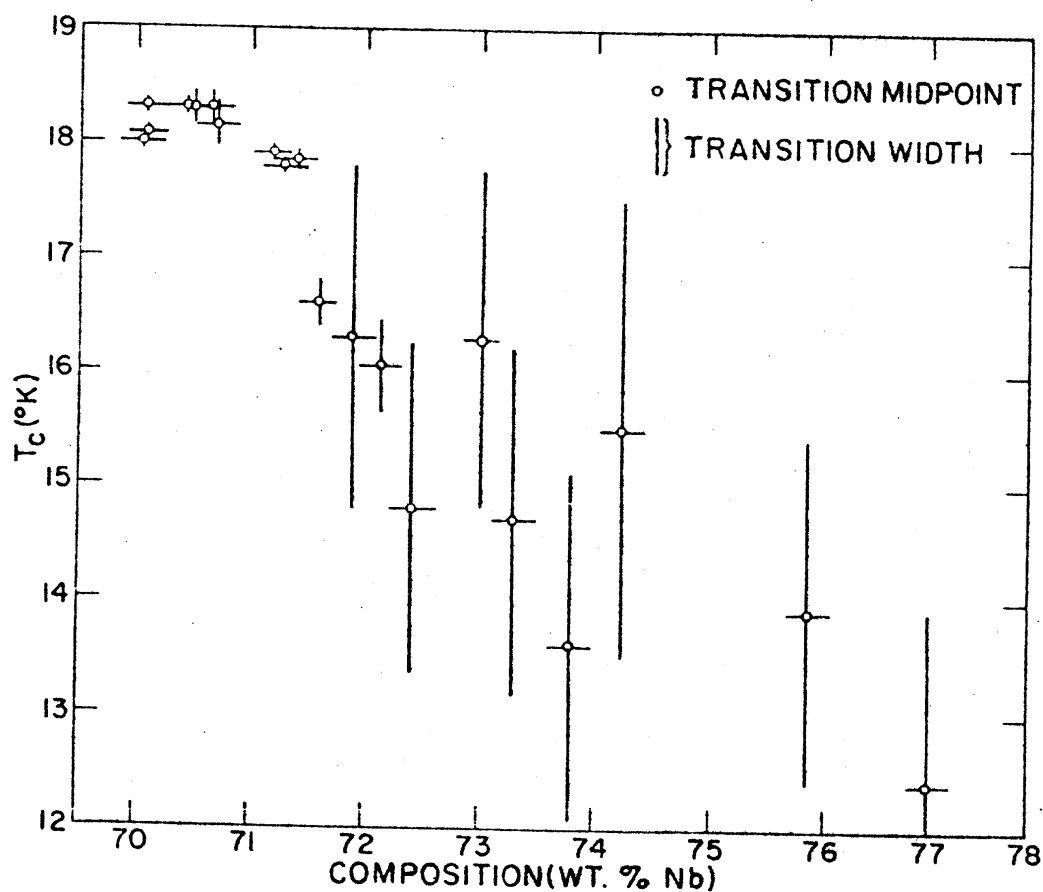


Fig. 2.8 Critical temperature as a function of wt.% Nb for samples made by the RCA process. 76 wt.% Nb is ~20 at.% Sn and 70 wt.% Nb is ~25 at.% Sn [22].

2.3.2 Liquid Phase Formation

2.3.2a The Kunzler Method

Kunzler et al. [24] made Nb_3Sn in two different ways. Rectangular rods of Nb_3Sn were made by sintering a stoichiometric mixture of Nb-Sn powders at 1800 °C and then melting the compact in a zirconia crucible in an argon atmosphere at about 2400 °C. A second method, suitable for making wires, was to fill Nb tubes with a mechanical mixture of

either Nb₃Sn powder + a 10 wt.% excess of powdered Sn, or a similar mixture of unreacted Sn and Nb powders. Each tube was then sealed with a Nb plug and then heat treated between 970 °C and 1400 °C for a period of time up to 24 hours. The highest J_c yielded by the sintering method was 30.4 A/mm² at 8 T and 4.2 K, while with the powder method the highest J_c yielded, using a stoichiometric mixture of Nb-Sn powders (3Nb+Sn), was 282 A/mm² at 8 T and 4.2 K, and with a stoichiometric mixture of Nb-Sn powders + 10% Sn powder (3Nb+Sn+10 wt.%Sn) the highest J_c was 1412 A/mm² at ~9 T and 4.2 K. The Nb₃Sn + excess Sn powder (Nb₃Sn + 10 wt.%Sn) sample was only tested at 1.5 K. The J_c of this sample was 508.5 A/mm² at 8 T. This can be compared with measurements of the stoichiometric mixture of Nb-Sn powders (3Nb+Sn) at 1.5 K which had a J_c of 395 A/mm² at 8 T. Kunzler noted that J_c values increased with decreasing temperature and that the powder core samples have higher J_c values because they form a filament structure, whereas the sintered samples do not.

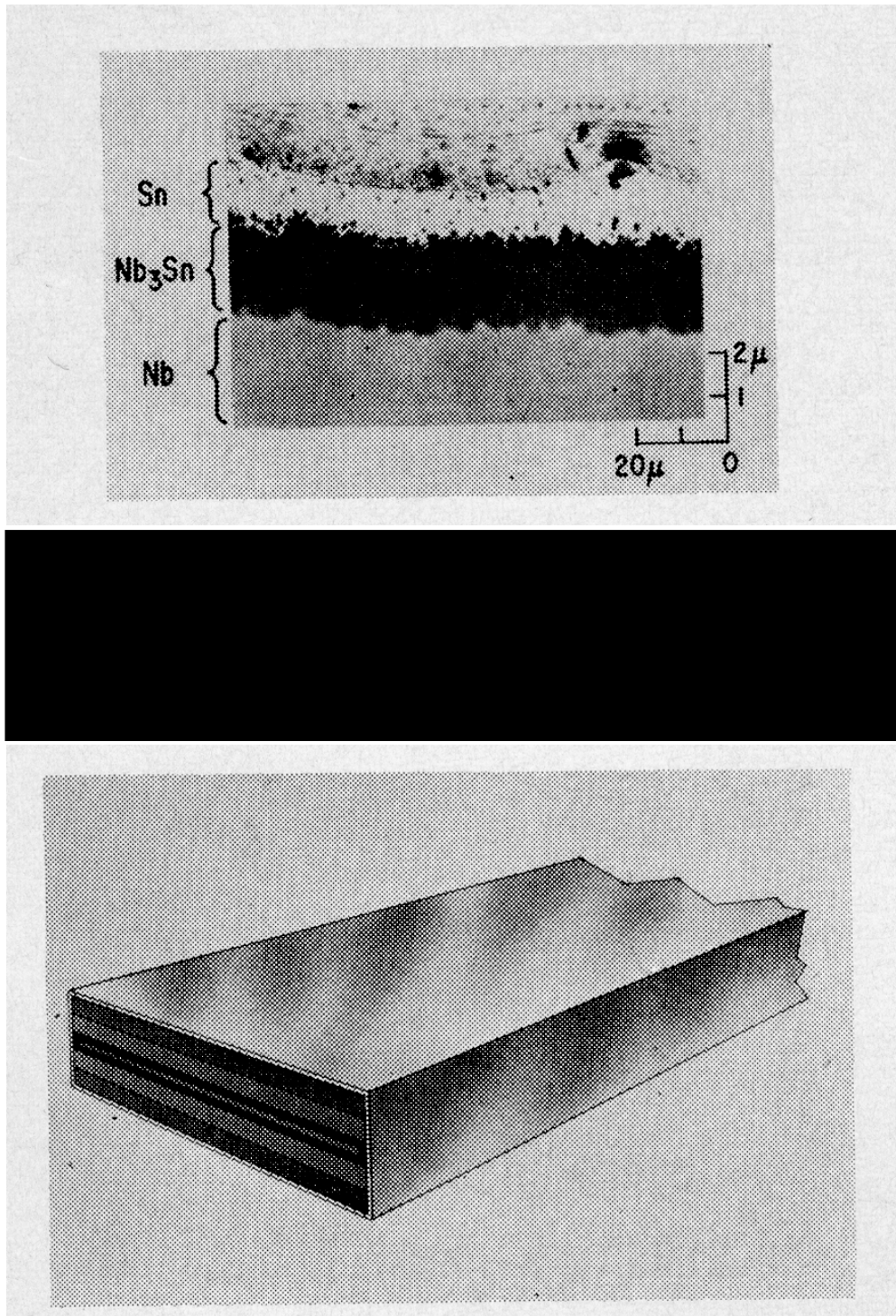


Fig. 2.9 Upper figure is photomicrograph of the diffusion layer of Nb₃Sn that forms between the Nb and Sn using the GE process. Lower figure is a schematic of the laminated conductor. The central region is Nb, then the Nb₃Sn, Sn, Cu, and then the stainless steel outer shell [25].

2.3.2b The GE Tape Process

The GE process, like the RCA process, was also developed in the 1960s. This process consists of taking a thin tape of Sn coated Nb and heat treating it at ~ 930 °C to form a layer of Nb₃Sn. What is left after the reaction is a layer of Nb₃Sn between a Nb core and the unreacted Sn. The conductor manufactured in [25] was 12.7 mm wide with a core region 10 μm thick surrounded by a Nb₃Sn layer 2.3 μm thick. This was fabricated into the laminate conductor by soldering it between two 25 μm thick Cu strips. Fig. 2.9 shows a photomicrograph and a schematic view of the finished conductor. This conductor had a J_c of 7×10^3 A/mm² at 4 T and 3.5×10^3 A/mm² at 8 T, both at 4.2 K. The GE process is similar to the external Sn process which is reviewed in section 1.4.3b.

2.3.3 *Solid State Diffusion*

2.3.3a Bronze Process

The bronze process consists of placing Nb or Nb alloy rods in into a high-Sn bronze tube or drilled high-Sn bronze ingot, Fig. 2.10. The bronze must be single phase high-Sn bronze, α -phase (0-9 at.% Sn, but must be 7-9 at.% to get good properties), to keep it ductile. During drawing the bronze work hardens, so an anneal at ~ 450 °C needs to be performed after every three draw passes, the reduction per draw pass is usually 20% [26]. Once the wire is drawn to its final size, it can then be heat-treated to form the Nb₃Sn layer by interdiffusion at the Nb / bronze interface. It is essential to carefully control the time and temperature of the deformation anneals so as to avoid significant A15 formation. Such pre-

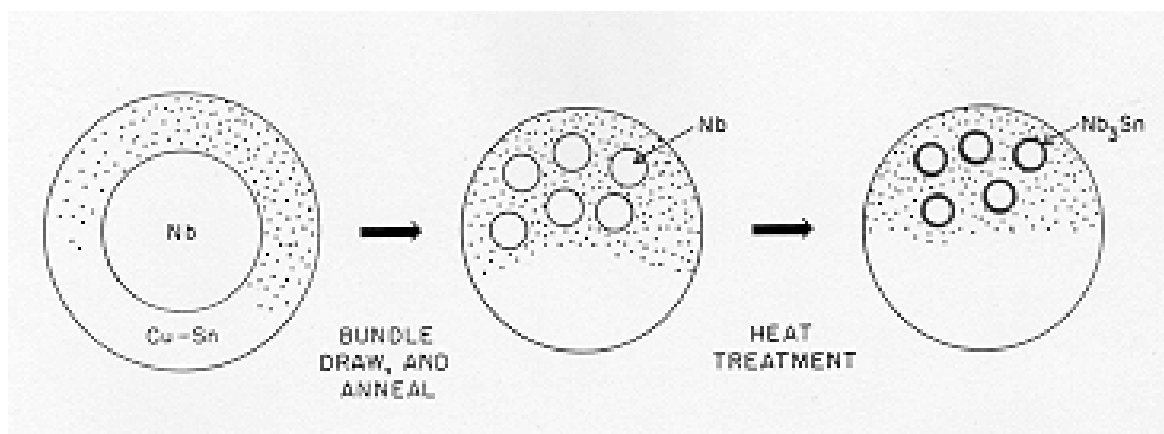


Fig. 2.10 Schematic diagram of the bronze process [27].

reaction can lead to degradation of J_c , resistive transition index, and even composite breakdown [26]. Fig. 2.11 is a cross-sectional image of a bronze-processed conductor. A comparison of bronze route conductors over the past decade shows an improvement in J_c from 850 A/mm^2 at 10 T and 4.2 K [28] to a J_c of $\sim 1200 \text{ A/mm}^2$ at 10 T and 4.2 K [29].

2.3.3b External-Sn Process

Tachikawa and Iwasa developed a method for manufacturing V_3Ga tape conductors, which avoids the need for bronze anneals [30]. A cold rolled tape, $50 \mu\text{m}$ thick and 3 mm wide, of vanadium is passed through a molten bath of gallium at 700°C , this creates both layers of V_3Ga_2 and VGa_2 on both surfaces of the substrate, the layers are about $4 \mu\text{m}$ thick. After the tape is passed through the gallium bath it is electroplated with a $5 \mu\text{m}$ thick layer of copper, then sealed in a quartz tube under Ar pressure of 500 Torr and heat treated. The copper plating enhances the diffusion of the vanadium in the V_3Ga_2 and increases the formation rate of the V_3Ga layer. The copper is not present in the V_3Ga layer and has no effect on its properties. The finished tape has a $30 \mu\text{m}$ thick layer of vanadium with $8\text{-}10 \mu\text{m}$

layers of V_3Ga on both sides. The entire conductor is enclosed by a layer of Cu-Ga alloy containing about 15% gallium and less than 1% vanadium. After heat treatment, the whole conductor is copper plated making a total conductor thickness of $\sim 90 \mu m$. Tapes manufactured by this process have upper critical fields of 21.5 T and J_c values of $1.1 \times 10^3 A/mm^2$ at fields of 20 T and 4.2 K. Conductors with 2% Zr alloyed in the original starting vanadium tapes have J_c values of $1.8 \times 10^3 A/mm^2$ at 20 T and 4.2 K. The Zr is believed to limit the grain size of the V_3Ga , thus increasing the grain boundary area. An increase in grain boundary area has been shown to increase flux pinning, thus increasing the current carrying capabilities of the conductor [31]. Adding a second heat-treatment at $600^\circ C$ has been shown to improve the T_C by 0.5 K and raise J_c to $2 \times 10^4 A/mm^2$ at 19 T and $1 \times 10^4 A/mm^2$ at 20 T and 4.2 K. The second heat treatment is believed to improve the ordering parameter of the A15 structure resulting in the improvement of the superconducting properties [32].

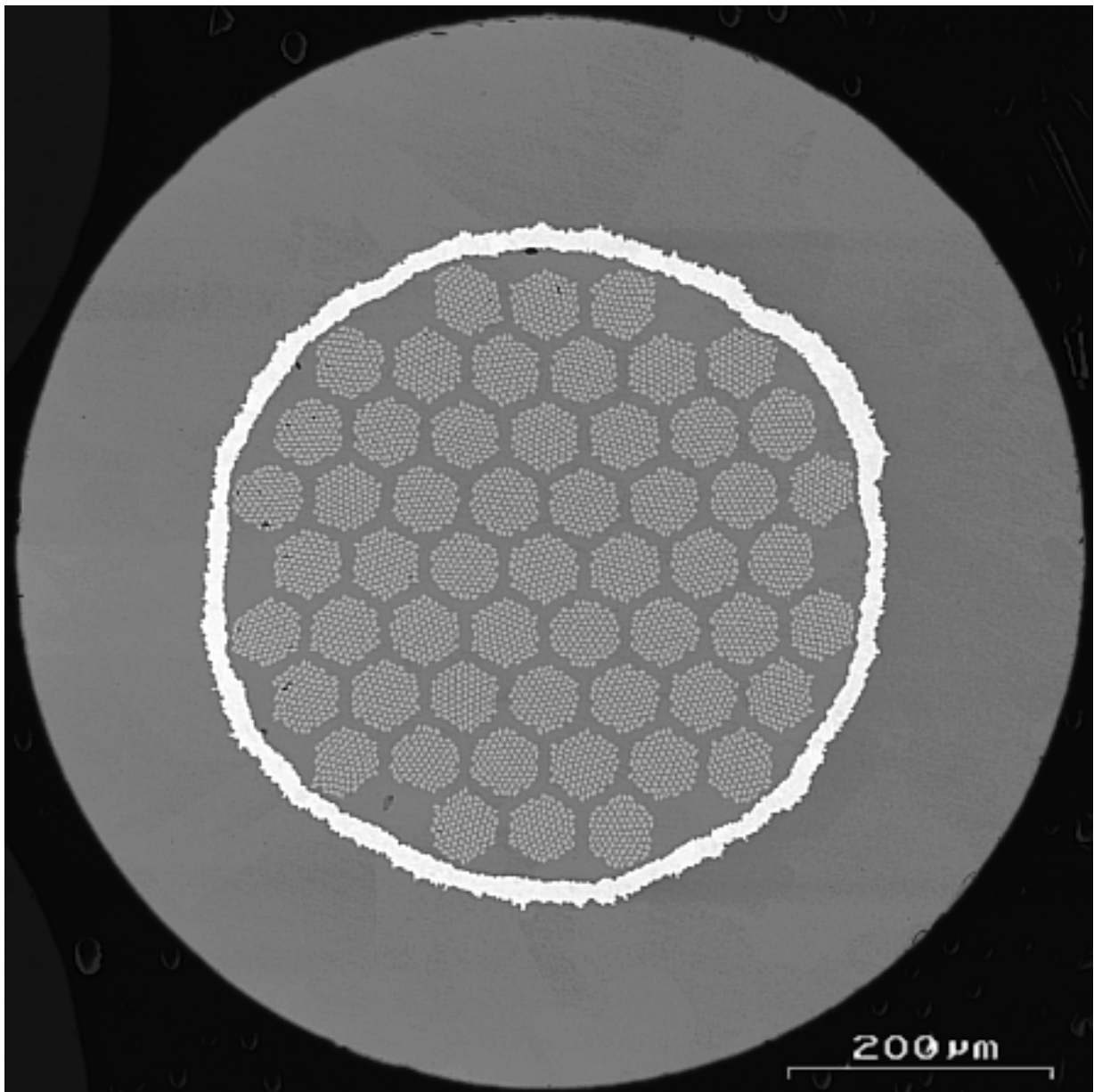


Fig. 2.11 Backscatter electron image of a modern day bronze processed conductor manufactured by Vacuumschmelze for ITER (International Thermonuclear Reactor Experiment). Image taken by Dr. Peter Lee, University of Wisconsin – Madison, Applied Superconductivity Center.

In the process, described by Suenaga and Sampson [33], Nb rods are inserted into a pure Cu matrix, this package is drawn to final size, and then coated with Sn by passing it through a molten Sn bath. The wire is then heat treated to transform the Cu into a bronze

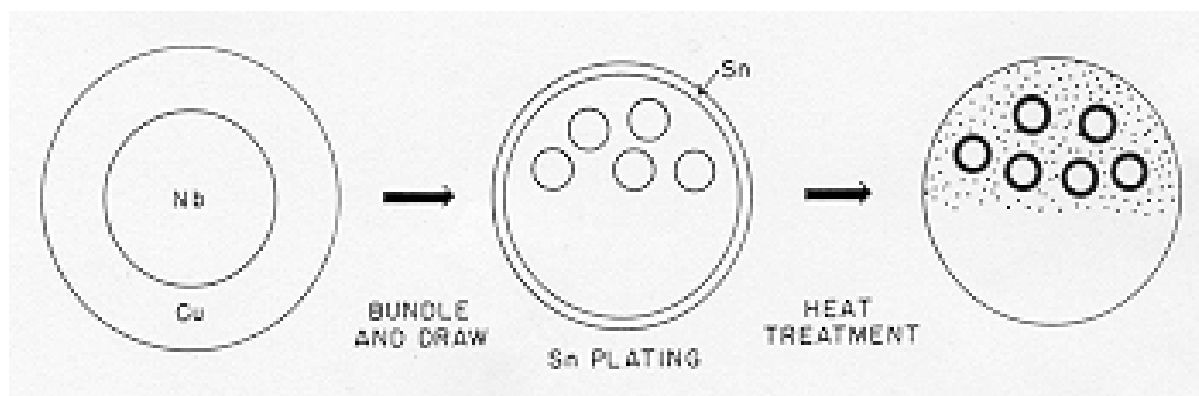


Fig. 2.12 Schematic diagram of the external Sn process [27].

matrix, and then a layer of Nb_3Sn forms around the Nb rods, Fig. 2.12. This process, known as the external Sn process, is similar to the bronze process, in that Nb tubes are inserted into a matrix, drawn, and heat-treated to form a layer of Nb_3Sn . The biggest difference is that the Cu does not work harden like the bronze, so no intermediate annealing steps are necessary between the drawing steps. A critical drawback of this method is the delamination of the Sn coating which occurs when the Sn thickness is greater than $\sim 5 \mu m$.

2.3.3c Internal-Sn Process

The delamination problem described above is a major constraint on the process since it limits the wire size to < 0.25 mm in diameter [34]. To address this problem the Sn can be incorporated internally; as first shown by Hashimoto, et al. This first variant of the internal Sn process consists of placing a Cu-clad (Sn-20 at.% Cu) alloy rod at the center of a Cu tube. Pure Sn rods can also be used, but tend to be too soft for reliable composite manufacture. Surrounding the alloy rod in the Cu tube are Cu-clad Nb bars, Fig. 2.13. The whole package is cold drawn to the final wire size and then heat treated to form Nb_3Sn at the Nb bars. Similar to the external diffusion process, there are no intermediate annealing steps necessary,

thus defining a distinct advantage as compared to the bronze process. An advantage over the external diffusion process is that the Cu stabilizer and Ta diffusion barrier can be placed on the outside of the wire, since the Sn is concentrated at the core of the wire. Some of the best internal Sn processed conductors to date are manufactured by Oxford Superconductor using an internal Sn modified jelly roll (MJR) process. This process consists of wrapping interleaved layers of Nb expanded metal and Cu around a Sn core to form a billet [35]. In the case of this particular conductor, known as CRE1912, the Nb expanded metal is an alloy of Nb0.8wt.%Ti. Fig. 2.14 is backscatter electron image of a Cre1912. Over the course of the past decade vast improvements in the performance of internal Sn conductors have occurred. The previously mentioned Oxford conductor, Cre1912, has a J_c of 3000 A/mm² at 10 T and 4.2 K [35], whereas a Vacuumschmelze internal Sn conductor, manufactured in 1990, has a J_c of 1010 A/mm² at 10 T and 4.2 K [28]. The improvements in performance can be attributed to third element additions which raise H_{c2} , the use of simpler manufacturing processes such as the modified jelly roll process, and the reduction of the overall Cu content in the Nb₃Sn formation package. The internal Sn conductors have higher J_c values than the bronze route conductors, see section 1.4.3a, but, in general, they also have higher hysteresis losses than bronze conductors, because of the tendency of filaments to grow together when the interweaving copper is removed from the Cu-Sn-Nb package, needed to form the A15 phase.

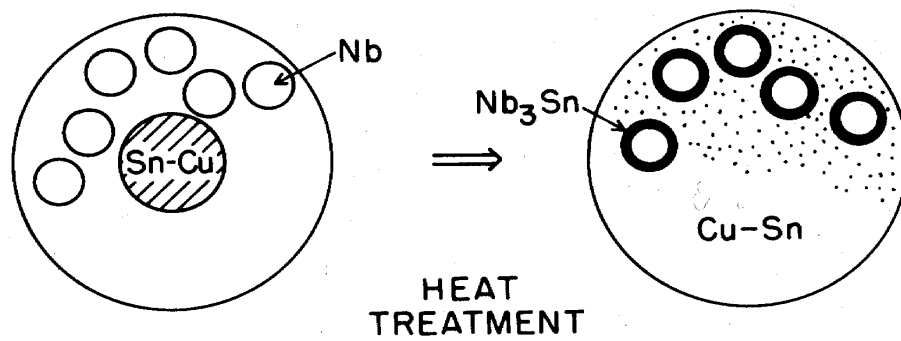


Fig. 2.13 Schematic diagram of an internal Sn conductor [36].

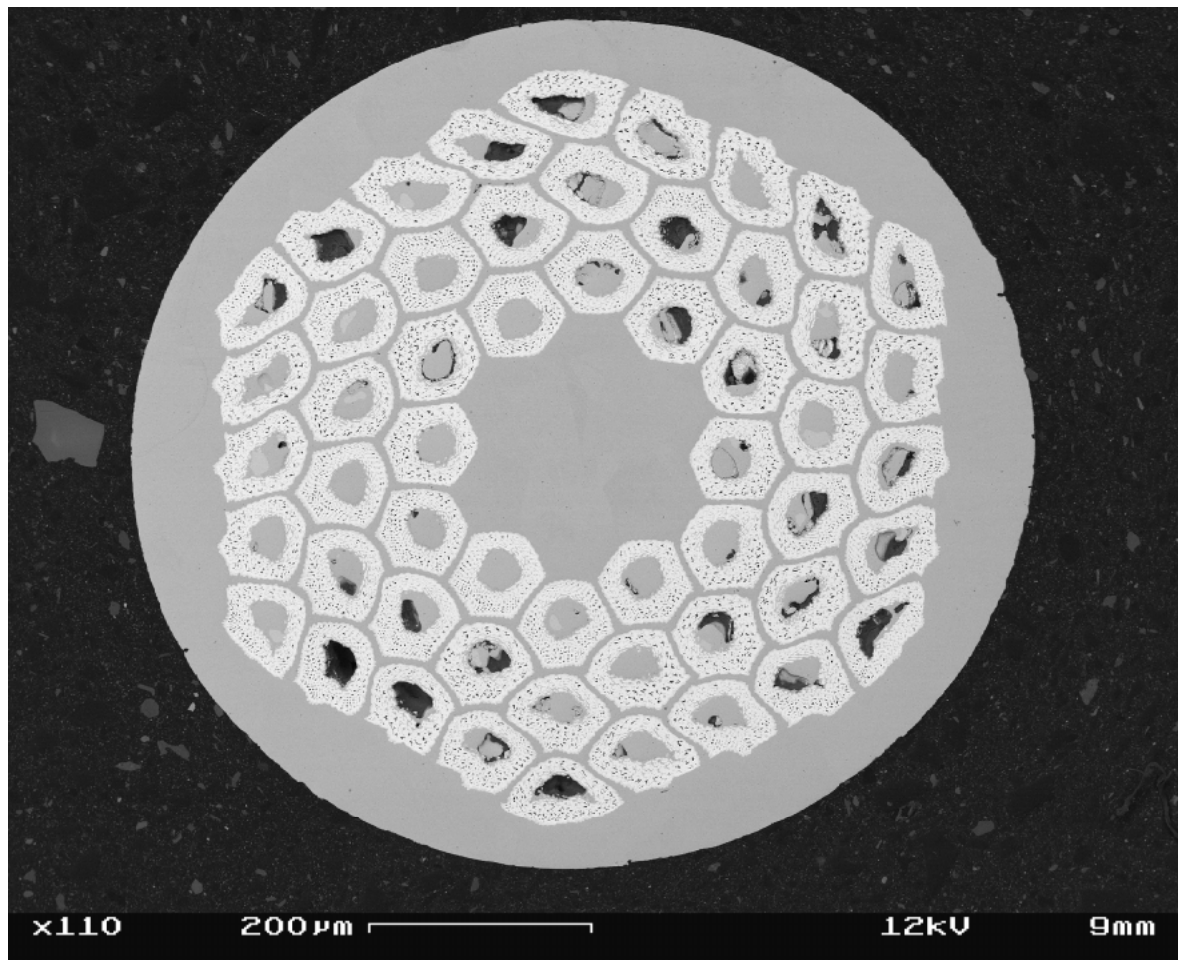


Fig. 2.14 Backscatter electron image of internal Sn conductor (Cre 1912) manufactured by Oxford Superconductor. Image taken by Dr. Peter Lee, University of Wisconsin – Madison.

2.3.3d Sn-Rich Powders

The powder-in-tube (PIT) process, used to make the PIT conductor investigated in this thesis, was developed at the Netherlands Energy Research Foundation (ECN). The PIT process has gone through many iterations, starting with a 36 filament, each filament $\sim 35 \mu\text{m}$ in diameter, cold rolled wire. This wire consisted of Nb tubes filled with $\text{NbSn}_2 + 15\% \text{Cu}$ powder [37], Fig. 2.15. To the modern day 504 filament, each filament $\sim 30 \mu\text{m}$ in diameter, wire, which consists of NbSn_2 powder, less than $3 \mu\text{m}$ in size, mixed with a Cu powder [38], Fig. 2.16. Cu powder enhances Sn diffusion, and it has been found that greater than 3 wt.%

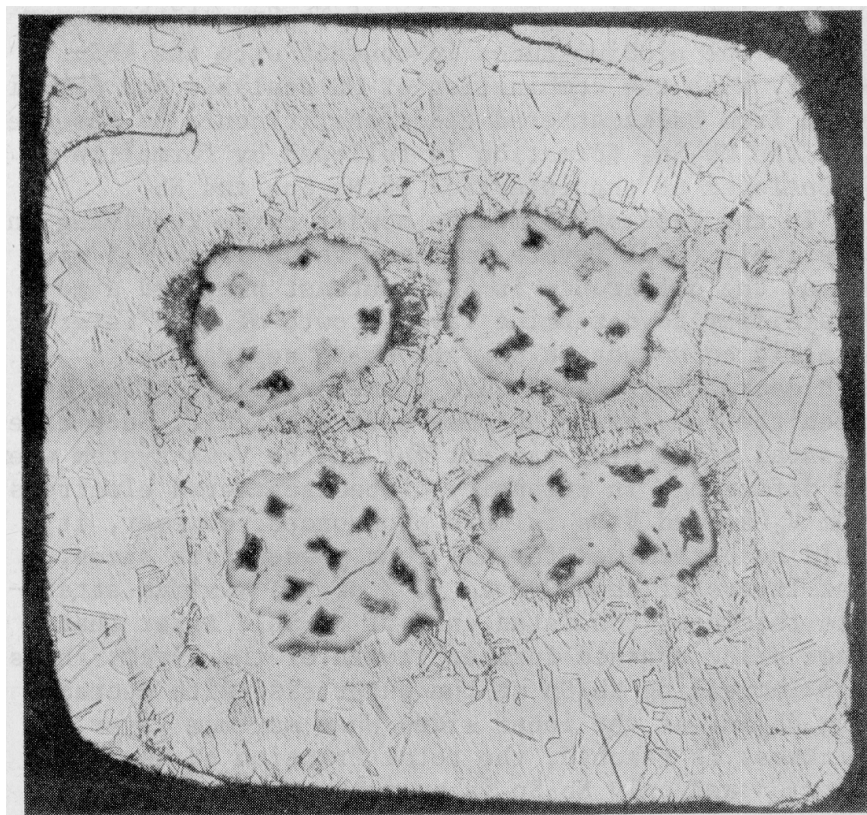


Fig. 2.15 1 mm square 36-filament PIT wire containing 3.3 vol. % powder. This wire was formed by inserting $\text{NbSn}_2 + \text{Cu}$ powder filled Nb tubes into the Cu matrix and then cold rolling the whole package [37].

Cu decreases the heat treatment temperature to below 700 °C [39]. An overview of the compositional and metallographic studies of the Nb₃Sn formed by the PIT process will be given and then a review the superconducting properties of the various wires.

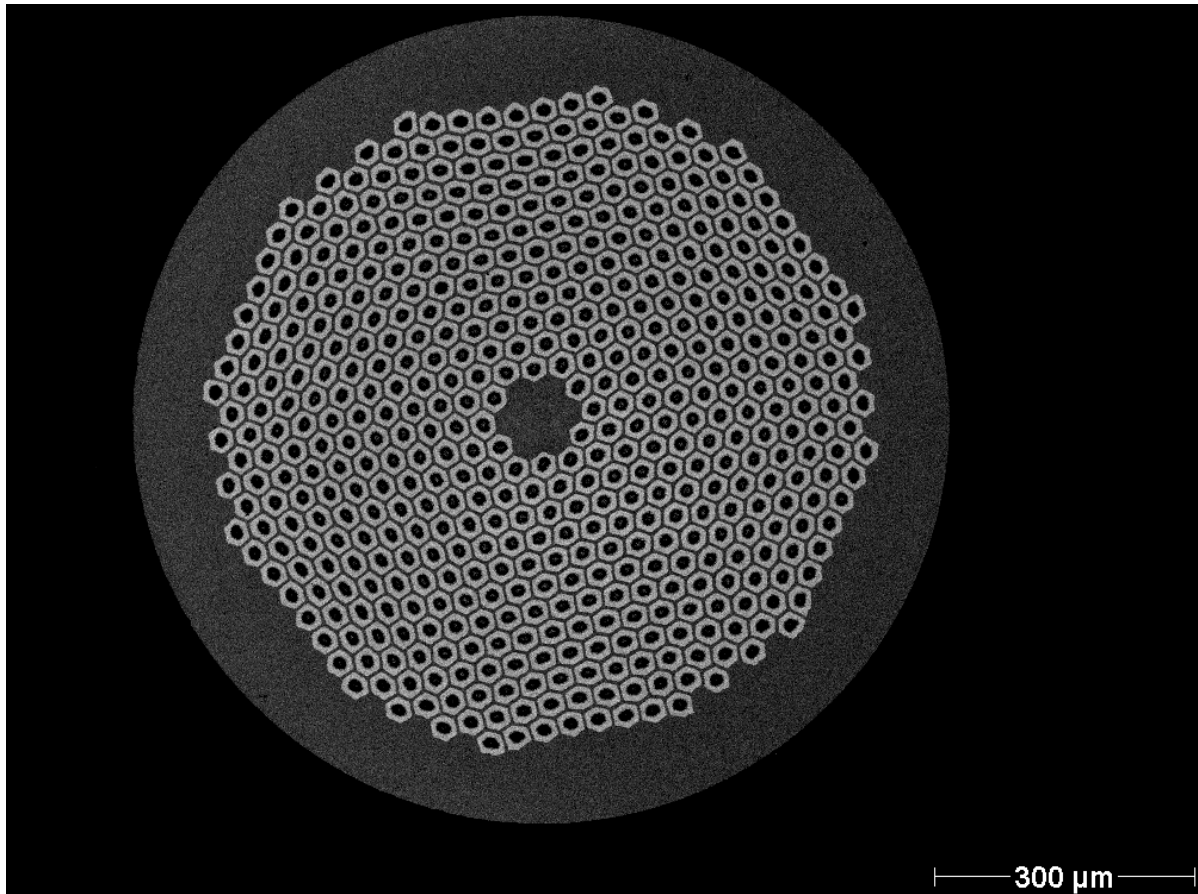


Fig. 2.16 Backscatter electron image of 0.9 mm in diameter ShapeMetal Innovations 504-filament Powder-In-Tube wire. Image taken by Christopher Hawes at the University of Wisconsin-Madison.

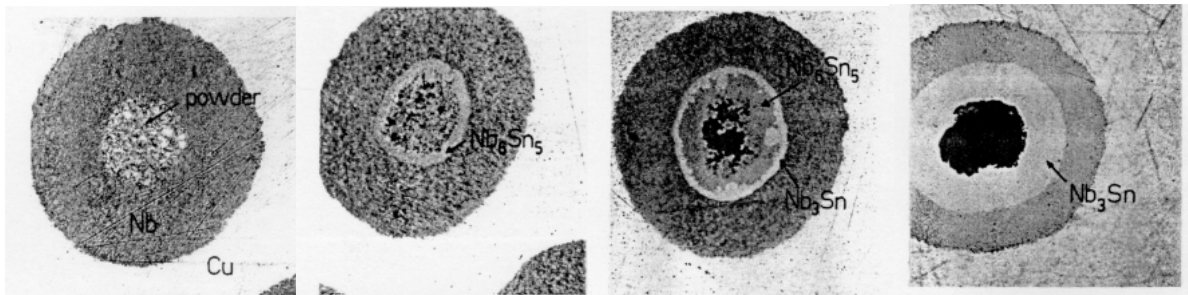


Fig. 2.17 Starting from the left image, the unreacted filament with the Nb tube, NbSn_2 and Cu powder core, and the Cu matrix can be seen. Filament diameter is $37\ \mu\text{m}$. The next image is after 1 hour at $700\ ^\circ\text{C}$. The Nb_6Sn_5 has formed a layer $1\ \mu\text{m}$ thick. The third image is after 16 hours at $700\ ^\circ\text{C}$. A thin layer of Nb_3Sn has begun to form. The final image is after 48 hours at $700\ ^\circ\text{C}$. The Nb_6Sn_5 layer has been consumed and the Nb_3Sn layer has taken its place. Some of the Nb tube remains to act as a diffusion barrier [40].

First, the NbSn_2 in the powder core reacts with the tube wall to form Nb_6Sn_5 . This reaction occurs quickly, within 1 hour a $4\ \mu\text{m}$ layer grows between the tube wall and the core [40]. The Nb_6Sn_5 that forms has a needle-like structure that allows rapid radial Sn transport [40]. After the Nb_6Sn_5 has grown to completion, the formation of Nb_3Sn occurs. The growth of the Nb_3Sn is from two sources, the depletion of Sn from the Nb_6Sn_5 and the diffusion of Sn into the Nb to form Nb_3Sn [40]. It has been observed that the Nb_3Sn formed from the Nb_6Sn_5 forms large grains ($\sim 2\ \mu\text{m}$) and the Nb_3Sn grains that form from the diffusion of Sn into the Nb tube are much smaller. It is believed the large grains of Nb_3Sn formed from the Nb_6Sn_5 because the Nb_3Sn is formed from a liquid bronze [39]. The fine and large grain Nb_3Sn form at the same rate because the mechanism controlling them is depletion of Sn from the Nb_6Sn_5 , in the presence of the liquid bronze, to form the Nb_3Sn in the diffusion reaction [40]. Fig. 2.17 presents time lapse steps in the growth of the Nb_3Sn layer, showing the growth of a ring of intermediate Nb_6Sn_5 phase. Fig. 2.18 presents magnified views of the reaction front, showing how the fine grained Nb_6Sn_5 transforms into a coarse grained A15 layer.

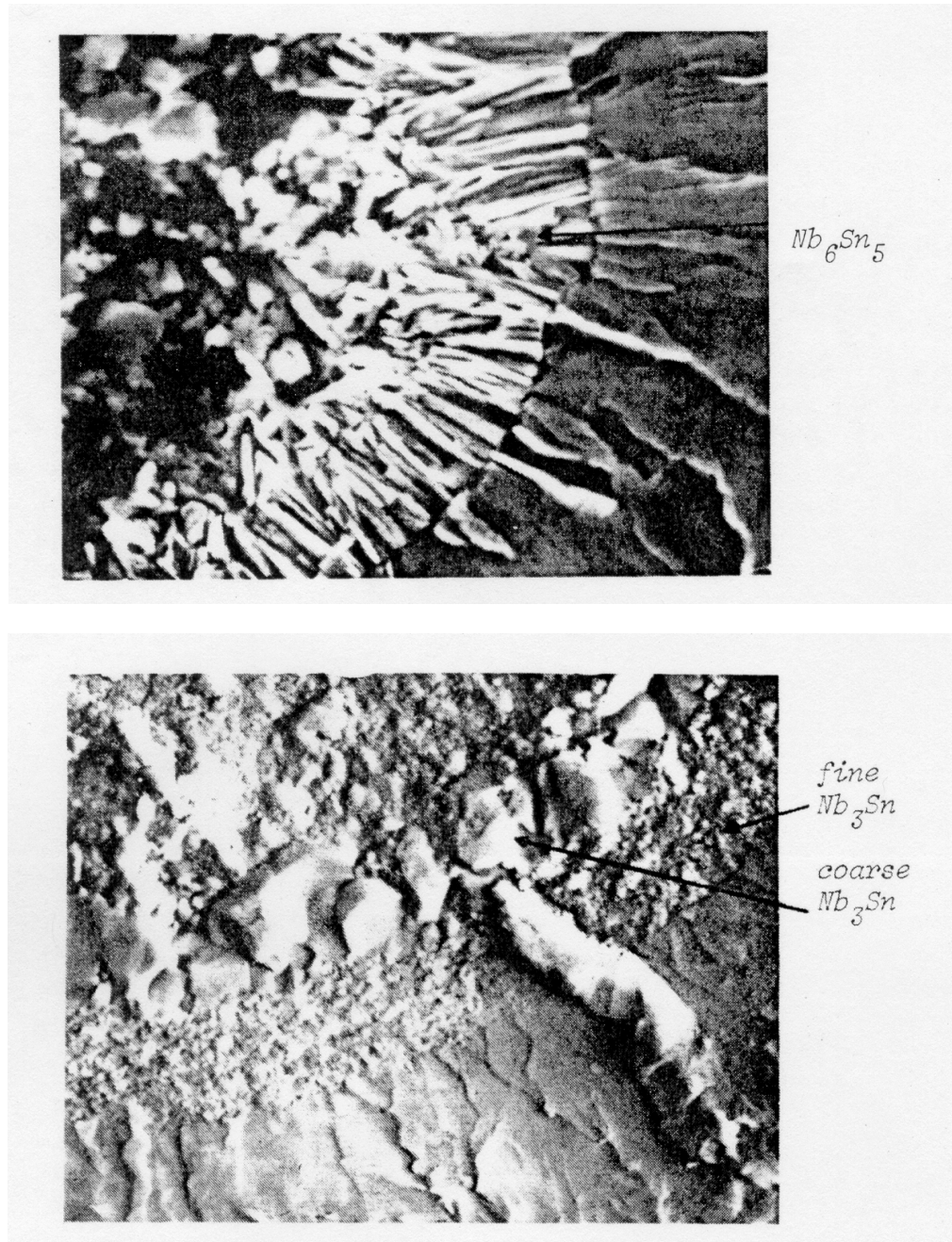


Fig. 2.18 Top image shows fine grains of Nb_6Sn_5 after 4 hours at 700 °C. To the right of the Nb_6Sn_5 is the Nb tube and to the left is the powder core. The lower image is after 48 hours at 700 °C. Coarse Nb_3Sn grains have formed near the core, where the fine Nb_6Sn_5 grains used to be, and fine grained Nb_3Sn has formed from the diffusion reaction between the Nb_6Sn_5 and Nb tube [40].

Figs. 2.19 and 2.20 present morphological and compositional studies on the layer growth of Nb_3Sn . Fig. 2.19 shows how the layer growth proceeds with time. We see that once the Nb_6Sn_5 has been depleted, the growth of the Nb_3Sn layer stops. This is believed to be due to the depletion of the Sn source. The graph on the left, in Fig. 2.20, shows the composition profile for a heat treatment at 675°C performed only until Nb_6Sn_5 formed while, on the right, is the composition profile for complete Nb_3Sn formation which occurred after 48 hours at 675°C . It appears from Fig. 2.19 that the coarse grained Nb_3Sn is slightly Sn rich compared to the finer grained. It was noted in [39], that Suenaga showed that the

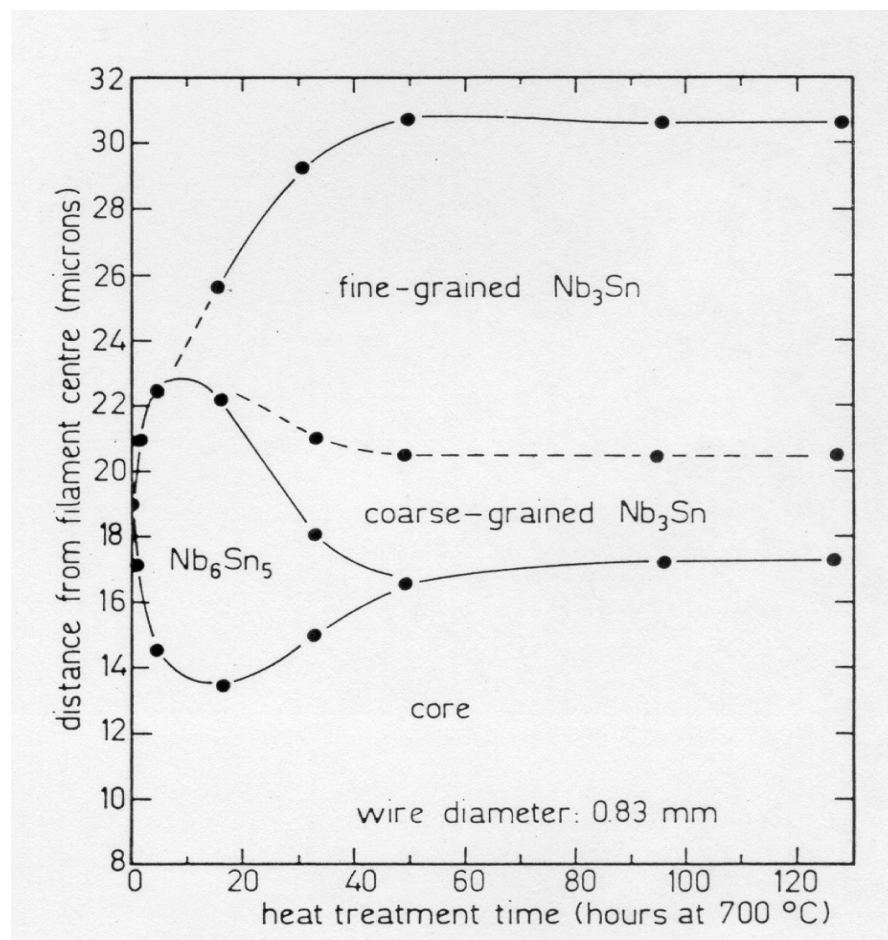


Fig. 2.19 Growth of Nb_6Sn_5 and Nb_3Sn layers as a function of heat treatment time [40].

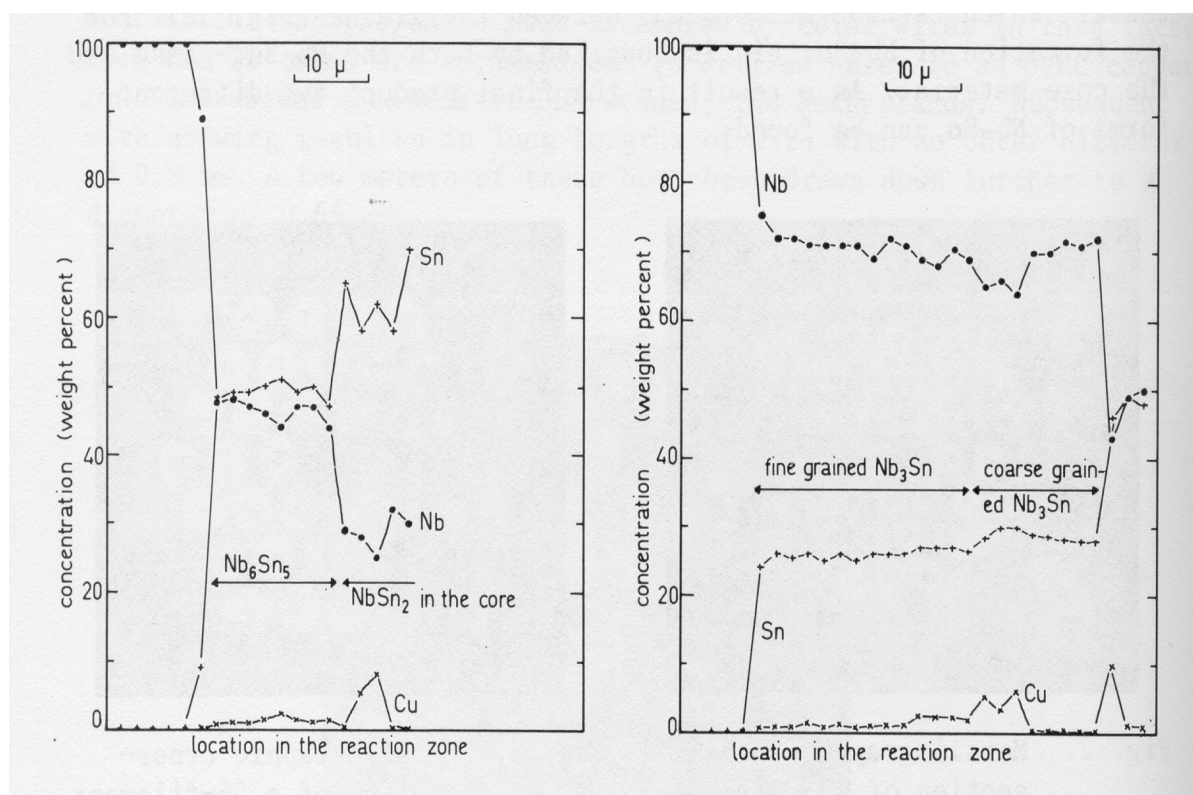


Fig. 2.20 The figure on the left is the concentration profile for the Nb₆Sn₅ layer. The figure on the right is the concentration profile of the Nb₃Sn layer. Note in both figures the core is on the right side and the Nb tube wall is on the left [39].

coarse grained material had a T_c of 18.2 K and the fine grained had a T_c of 17.7 K.

It is interesting to note improvements in the PIT process wires, starting with the 36-filament wire shown in Fig. 2.15. This wire had 7.5 μm thick Nb₃Sn layers, an 18 K resistive T_c , and a layer J_c of 3000 A/mm² at 12 T 4.2 K [37]. These results were after heat treatment times of 384 hours. A 180-filament, 2.3 mm diameter, Fig. 2.21, wire made with a variety of powder core diameters, 13, 18 and 26 μm, grew A15 layers ~ 5 μm thick after 136 hours. These wires had layer J_c values of 2500 A/mm² at 12 T. J.D. Elen et al. [41] worked on a drawn only 19-filament wire, 0.56 mm in diameter, with 31 μm powder core diameters, Fig. 2.22, and had the Cu to superconductor ratio of 6.0 to ensure stability. This wire had a

12 T overall J_c of 248 A/mm^2 and a Nb_3Sn layer J_c of 3270 A/mm^2 , with heat treatment times of only 96 hours at $700 \text{ }^\circ\text{C}$. Stabilized commercial scale, extruded and drawn, 18 and 36-filament Nb_3Sn PIT wires were investigated by [39]. Wire of this type were made in lengths of up to 1500 meters. The volume percentage of powder was varied in these wires, as was the final wire diameter. These wires had Kramer extrapolated H_{c2} values of 23-24 T and as the volume percentage of powder core increased, from 3.6 to 8%, and the Cu volume percent in the core decreased, from 74 to 56%, the critical current increased. The overall J_c value of the 36-filament, $\sim 0.65\text{mm}$ diameter, wire at 12 T was 600 A/mm^2 . This wire contained 56% Cu, 55% being the minimum for stability, taking that into account the non-Cu J_c would be 1071 A/mm^2 , with a heat treatment performed at $675 \text{ }^\circ\text{C}$ for 48 hours.

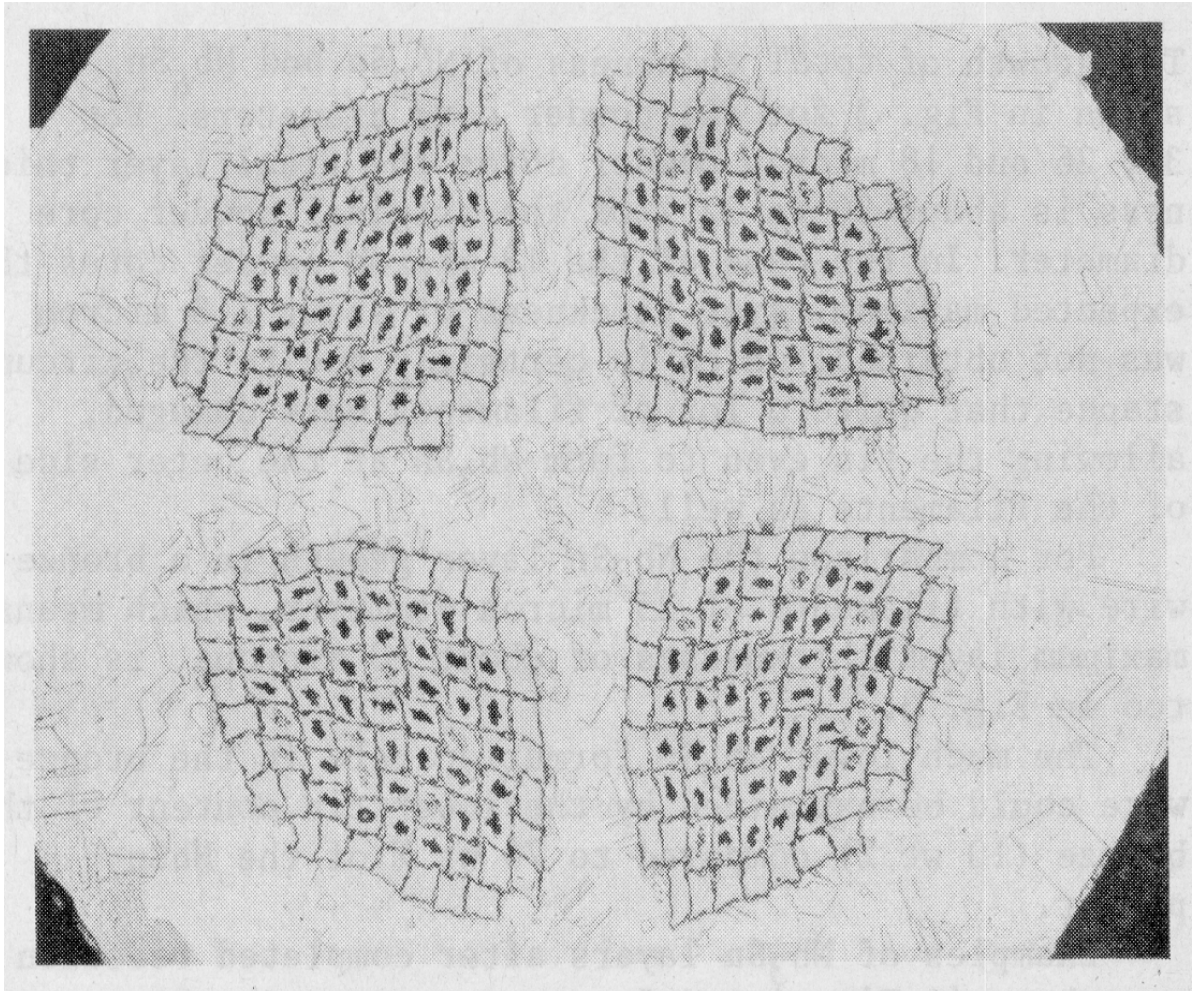


Fig. 2.21 2.3 mm diameter 180-filament wire. Surrounding each bundle of powder core filled Nb tubes is a Nb rod that acts as a diffusion barrier [32].

The decrease in heat treatment time and temperature over the years is due to the optimization of the amount of NbSn_2 and Cu in the powder core (The optimum amount of Cu is not stated specifically in the literature, but it appears to be ~5 at.%. This does not include the Cu tube, that surrounds the powder core, included in certain designs.), and the densification of the powder core prior to heat treatment. The latest PIT wire [38] is a 0.9 mm, 492 and 504-filament wires, 504-filament in Fig. 2.16, with 30 μm diameter filaments.

These wires were heat treated for 47 hours at 675 °C and obtained non-Cu J_c values of 1890 A/mm² at 10 T, in the 492-filament, and 2106 A/mm² at 11 T in the 504-filament [2].

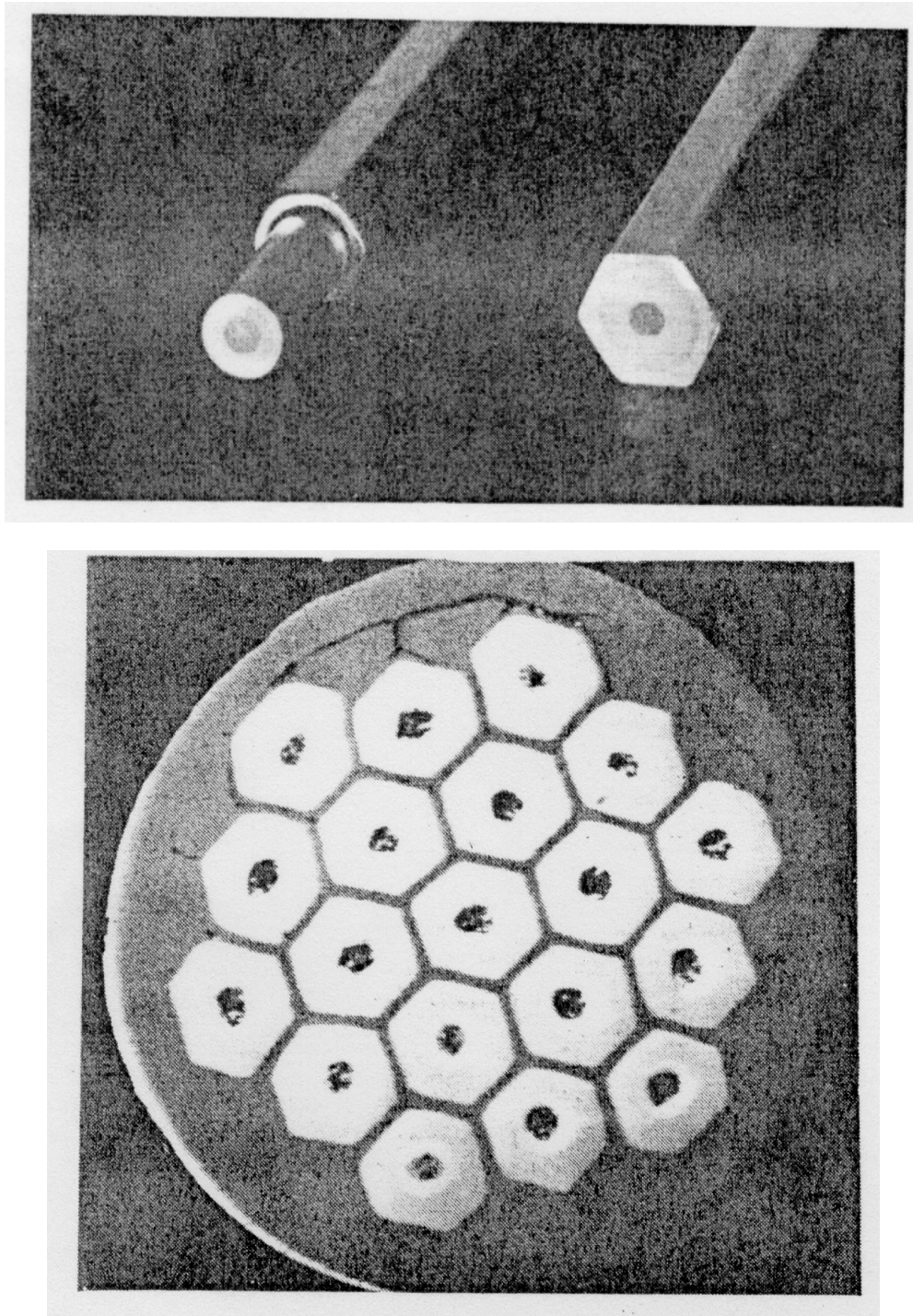


Fig. 2.22 Top image is of the single core rods that make up the filaments in the 0.56 mm 19-filament wire below [41].

Recently Tachikawa et al. [42] has made PIT tapes with excellent properties. These tapes are made by mixing powders of $\text{Nb}_6\text{Sn}_5/\text{Nb}$ in Nb tubes and then groove and flat rolling to a width of 5 mm and a thickness of 0.5 mm. The tapes are then heat treated between 750 °C and 1000 °C. Several variations of this tape have been made, the ones made in [42] include a $(\text{Nb,Ta})_6\text{Sn}_5$ powder mixed with Nb powder in the composition $(\text{Nb}_{0.95}\text{Ta}_{0.05})_3\text{Sn}$, and a Nb-4 at.% alloy powder was mixed with $(\text{Nb,Ta})_6\text{Sn}_5$ powder of in the composition of $(\text{Nb}_{0.96}\text{Ta}_{0.04})_3\text{Sn}$. These powders were encased in Ta tubes. Ta and Sn powders were mixed in the atomic ratio of 6:5 and encased in Nb, Nb-1.8 at.% Ta, Nb-3.3 at.% Ta, or Nb-4.2 at.% Ta tubes. Also, tapes were made by mixing powders of $\text{Nb}_6\text{Sn}_5/\text{Nb}$ in Nb tubes. All tapes were groove and flat rolled to a width of 5 mm and a thickness of 0.5 mm and then heat treated between 750 °C and 1000 °C with no intermediate annealing. Tapes of just $\text{Nb}_6\text{Sn}_5/\text{Nb}$ powder in Nb tubes attain J_c (core) values of 35 A/mm² at 22 T and the tape containing Nb-4 at.% alloy powder was mixed with $(\text{Nb,Ta})_6\text{Sn}_5$ powder of in the composition of $(\text{Nb}_{0.96}\text{Ta}_{0.04})_3\text{Sn}$ had a J_c (core) of 500 A/mm² at 22 T. Both of these tapes were heat treated for 80 hours at 925 °C. The tape with the Nb-3.3 at% Ta alloy tube attained a layer thickness of 80 μm after 80 hours at 900 °C. This tape had a layer J_c of 750 A/mm² at 20 T.

2.3 Summary

The table below summarizes some of the main points about each of the Nb₃Sn manufacturing processes reviewed in this section.

Process	Accessible product forms	Comments
Vapor Phase (CVD) Tapes	Tape	Discontinued in the 1960s.
Nb-Liquid Sn	Tape	Used as recently as the mid 1990s for 4 T MRI systems.
Nb-Sn Powder	Simple wires	Reaction must take place above 930 °C to avoid high Sn Nb-Sn phases.
Bronze Process	Very flexible multifilament geometry	Still widely used today, but limited Sn:Cu ratio means maximum A15 cross-section in Nb/Cu-Sn package is ~30%.
External Sn Process	Simple multifilament geometries	Discontinued due to delamination problems.
Internal Sn Process	Very flexible	Highest present current densities.
Powder-In-Tube Process	Filament size limited to Nb tube size	High current density. Produced by only one company.

All present manufacturing routes utilize solid state diffusion, which leads to built-in composition gradients in the A15 layer. Some gradient appears inevitable in the PIT process because some of the Nb barrier must remain intact in order to serve as a barrier. The goal of the thesis, the study of the inhomogeneity in a PIT conductor, is taken up in the next chapter.

3. Investigations of the Inhomogeneity of a Powder-in-Tube Nb₃Sn Conductor

3.1 Preparation of Conductor

The PIT conductor used in this study was manufactured by ShapeMetal Innovations (SMI), Holland [2], [43]. The conductor contains 504 very uniform filaments, Fig. 3.1. Evidence of the composites careful manufacture is that the average cross-sectional area variation among 50 filaments was found to be less than 5%.

Wires were sealed in evacuated quartz tubes and heat treated at the SMI recommended temperature of 675 °C [2] for up to 263 hours. Heat treatments at 750 °C up to 110 hours were also performed, in order to assess the terminal reaction states of the composite.

3.2 Experiment

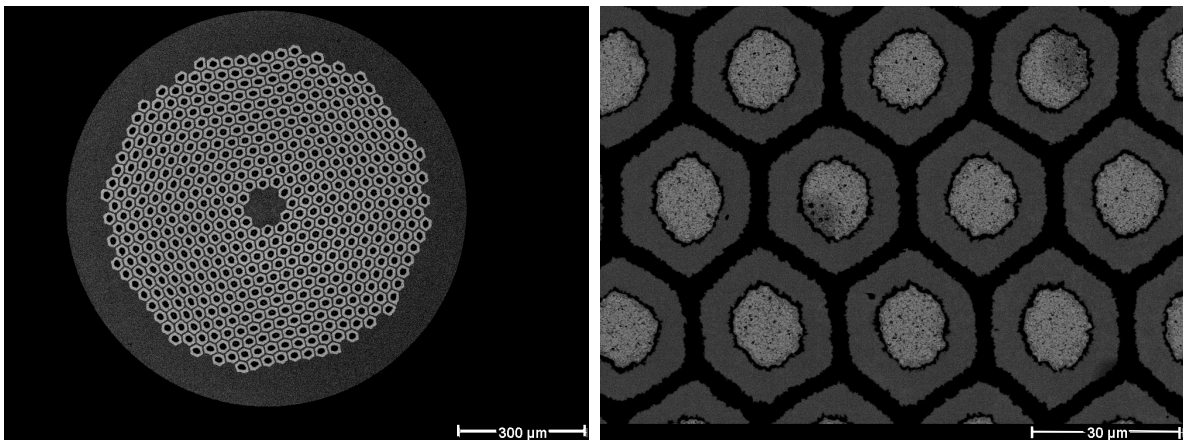


Fig. 3.1 ShapeMetal Innovations, Holland, unreacted 504 filament PIT composite wire. The wire diameter is 0.9 mm and the filament diameter is approximately 30 μm. In the right image the black region is copper, the gray region is niobium, and the light region is the core, which contains NbSn₂ and Cu powder.

3.2.1 Inductive Critical Temperature Measurements

The magnetization of 5-7 mm long sections of reacted wires was measured in a Quantum Design SQUID magnetometer with the applied magnetic field parallel to the wire axis. This geometry has a negligible demagnetization factor because l/d is so large. Full flux shielding can then be calculated rather closely. The samples were cooled to 5 K in zero field and then a 1 mT field was applied, the moment being measured for increasing temperature. A description of the magnetometer measurement and how the critical temperature as a function of filament radius is obtained can be found in the Appendix, section 5.1.

3.2.2 Heat Capacity Measurements

The heat capacity of 3-6 mg wire samples was measured in a Quantum Design Physical Properties Measurement System (PPMS), which utilizes the relaxation method. All samples were measured in zero field, cooling from 30 K or 22 K to 5 K. A description of the PPMS heat capacity measurement system is given in Appendix, section 5.2.

3.2.3 SEM-BSE/EDX Measurements

The backscatter electron signal in the SEM is directly proportional to the atomic number. BSE images of metallographically polished cross-sections were obtained to provide a description of the layer growth. The images were obtained on JOEL JSM-6100 SEM at 10 kV and a working distance of 15 mm. Fracture images were obtained using either a LEO-982 field emission scanning electron microscope (FESEM) or a LEO-1530 FESEM at 3 kV

and a working distance of 3 mm for the LEO-1530 and 6 mm for the LEO-982. Energy dispersive x-ray (EDX) analysis was performed on either the LEO-982 or the LEO-1530 at 8 kV and a working distance of 9 mm. Quantification from the Nb-L and Sn-L peaks by standardless analysis, using filter-fitting and 3 iteration ZAF correction, as supplied in the Voyager analysis system by Noran.

3.3 Results

3.3.1 SEM-BSE/EDX Measurements

Backscatter electron images, Fig. 3.2A, and EDX analysis of the 2 hour heat treatment at 675 °C show that a region of Nb_6Sn_5 forms during the first stages of the reaction between the powder core and the Nb tube. The progress of the reaction at 675 °C of the powder core and the Nb is shown in Figs. 3.2-3.4. After 4 hours (Fig. 3.2 D and E), both Nb_6Sn_5 and Nb_3Sn regions are visible. After 8 hours (Fig. 3.3 A and B), the Nb_6Sn_5 layer has changed from continuous in the 4 hour heat treatment to discontinuous. No Nb_6Sn_5 is visible after 16 hours (Fig. 3.3 C and D). At 47 hours the layer is only a little thicker than at 16 hours, but the A15 phase has clearly reached the Nb-Cu interface (Fig. 3.4 A and B) between the hexagonal edges of each filament. The 47 and 64 hour (Fig. 3.4 C and D) show little difference in the A15 layer thickness.

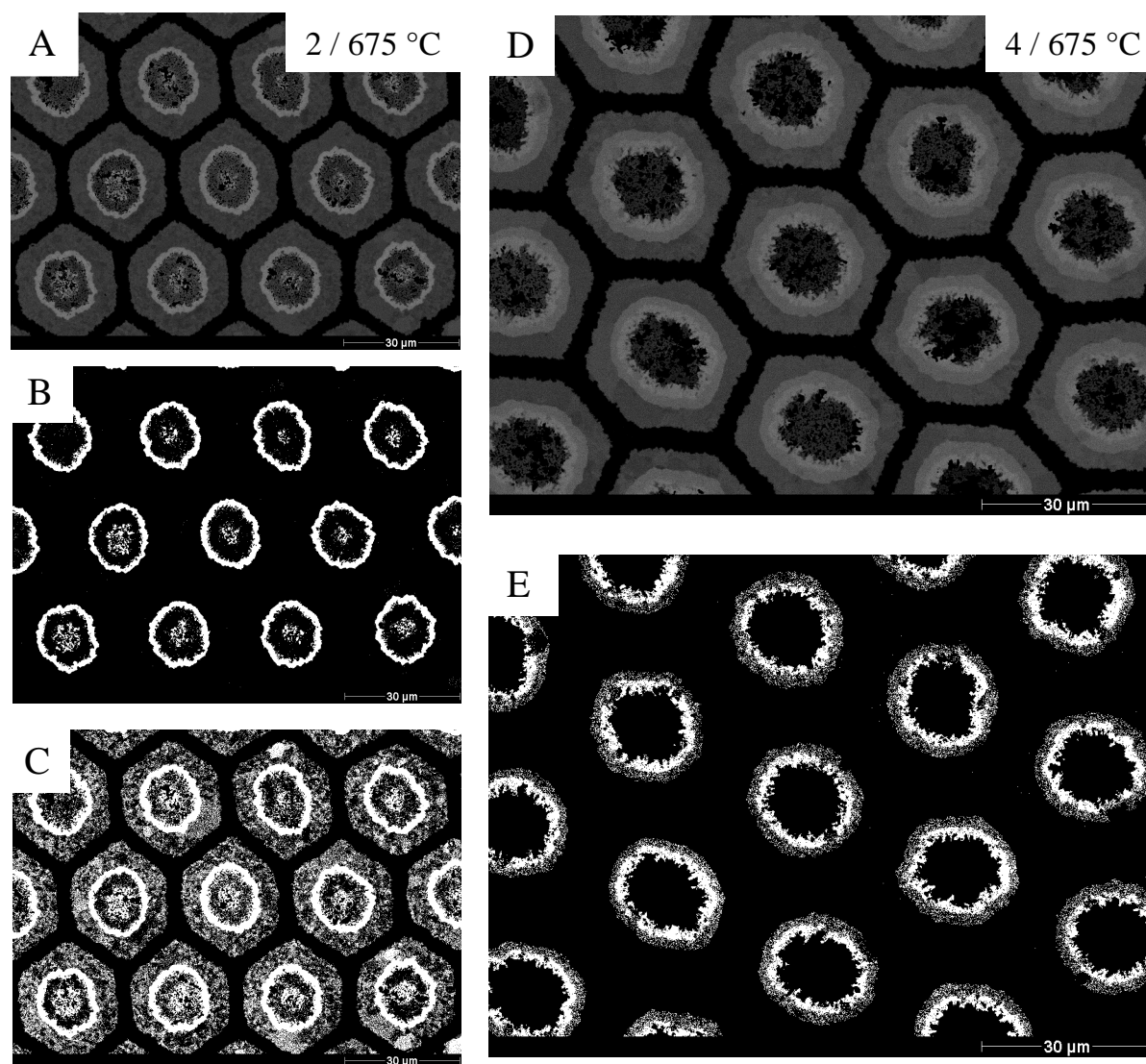


Fig. 3.2 Images A and D are atomic-number-sensitive backscatter electron images taken after the 2 and 4 hour heat treatments, respectively. In images A and D, the black matrix is Cu and the gray is Nb. In image D, the lighter gray region is A15 and the lightest region near the core is Nb_6Sn_5 . In image A, the lighter gray region next to the core is Nb_6Sn_5 , there is no A15 after the 2 hour heat treatment. Image B has had the contrast adjusted so that the Cu and Nb are black and the Nb_6Sn_5 is highlighted in white. Image C has had the contrast adjusted so that the Nb is the broken white region and the Nb_6Sn_5 is the solid region. Image E has had the contrast adjusted so the Cu and core are black, the Nb_6Sn_5 is the solid white region near the core, and the Nb_3Sn is the broken white region.

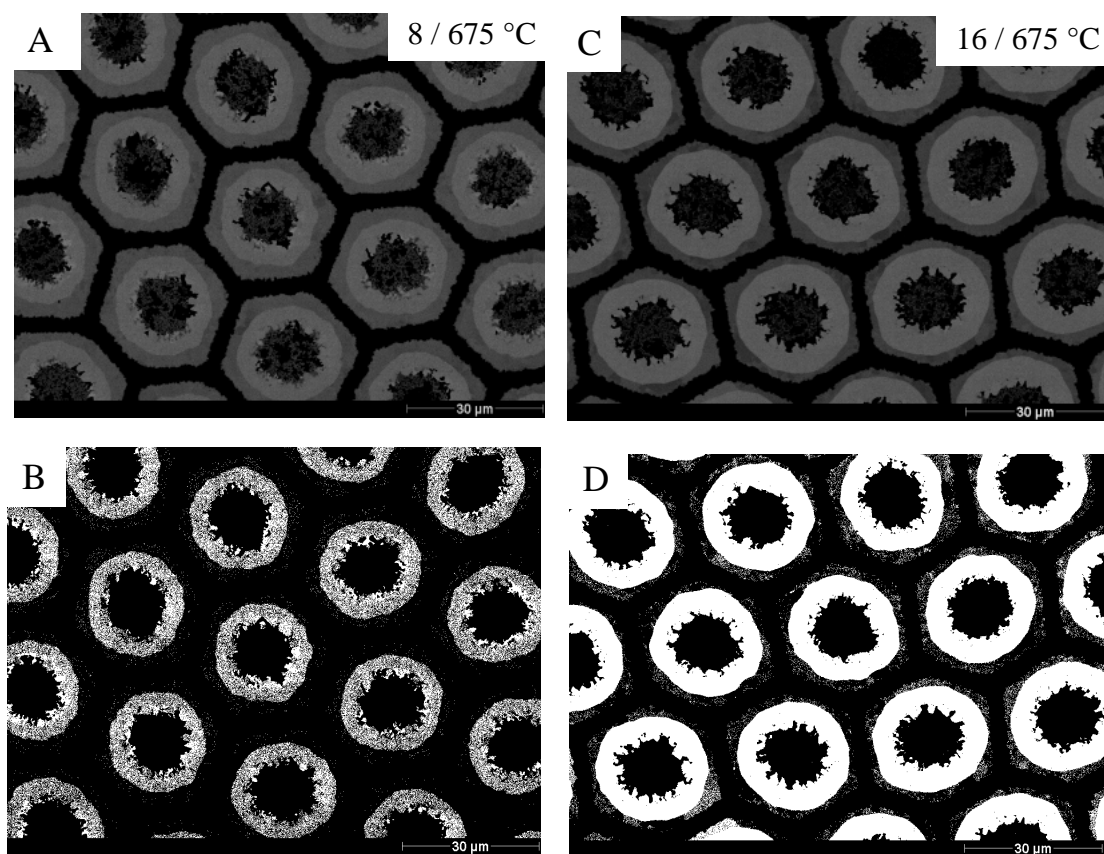


Fig. 3.3 Images A and C are atomic-number-sensitive electron backscatter images of the 8 and 16 hour heat treatments, respectively. In images A and C, the dark matrix is Cu and the gray area is Nb. In image A, the lighter gray region is Nb_3Sn , and the small, scattered, light gray regions near the core are Nb_6Sn_5 . In image C, there is only Nb_3Sn in the light gray region between the core and the Nb. Images B and D have had the contrast adjusted so the Cu and core regions are black, and in image B the contrast has been adjusted so the Nb is black. In image B, the broken white region is Nb_3Sn , while the solid white regions near the core are Nb_6Sn_5 . In image D, the solid white region is Nb_3Sn and the broken white region outside of that is Nb. The Nb_6Sn_5 has all been consumed by the 16 hour heat treatment.

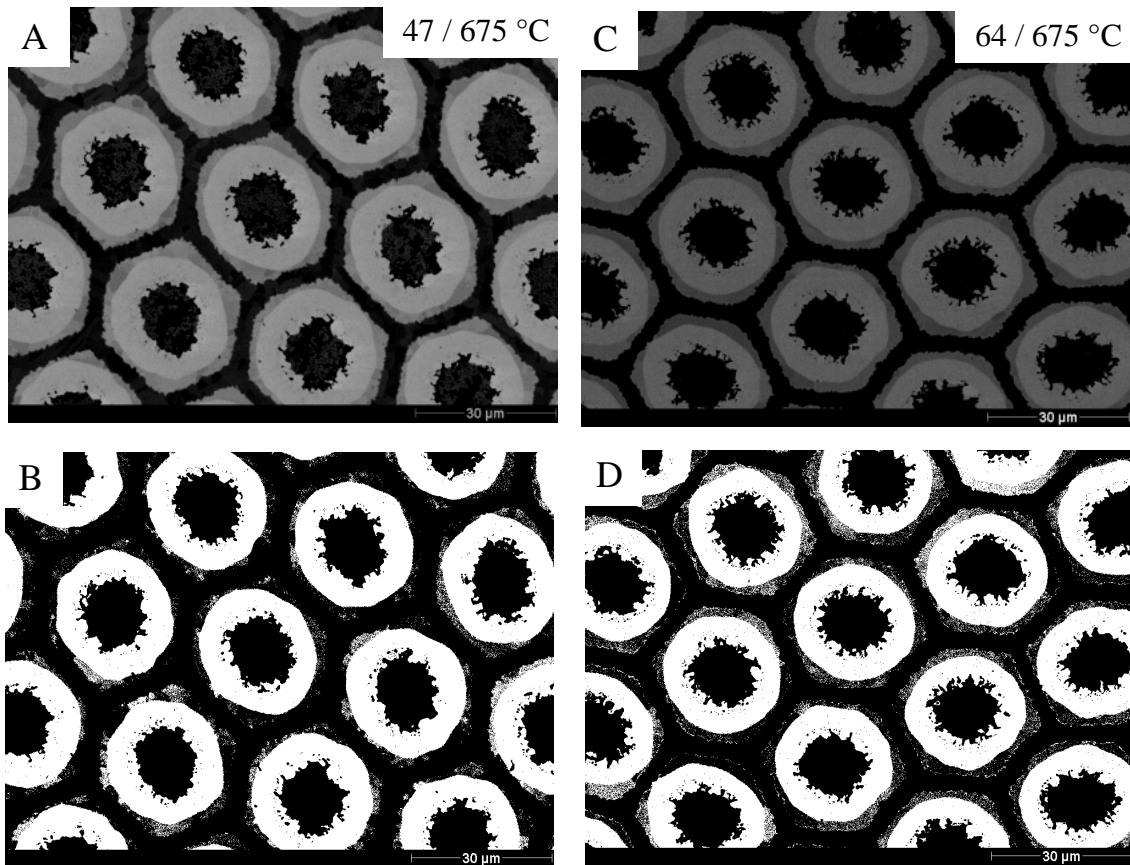


Fig. 3.4 Images A and C are atomic-number-sensitive electron backscatter images of the 47 and 64 hour heat treatments, respectively. In images A and C, the black matrix is Cu, the gray region is Nb, the lighter gray region between the core and niobium is the A15 layer. Images B and D have been contrast adjusted so that the Cu and core regions are black, the Nb₃Sn region is solid white, and the Nb region is broken white. It can be seen that in some places of some the filaments, the Nb₃Sn has fully consumed the Nb and is in contact with the Cu matrix.

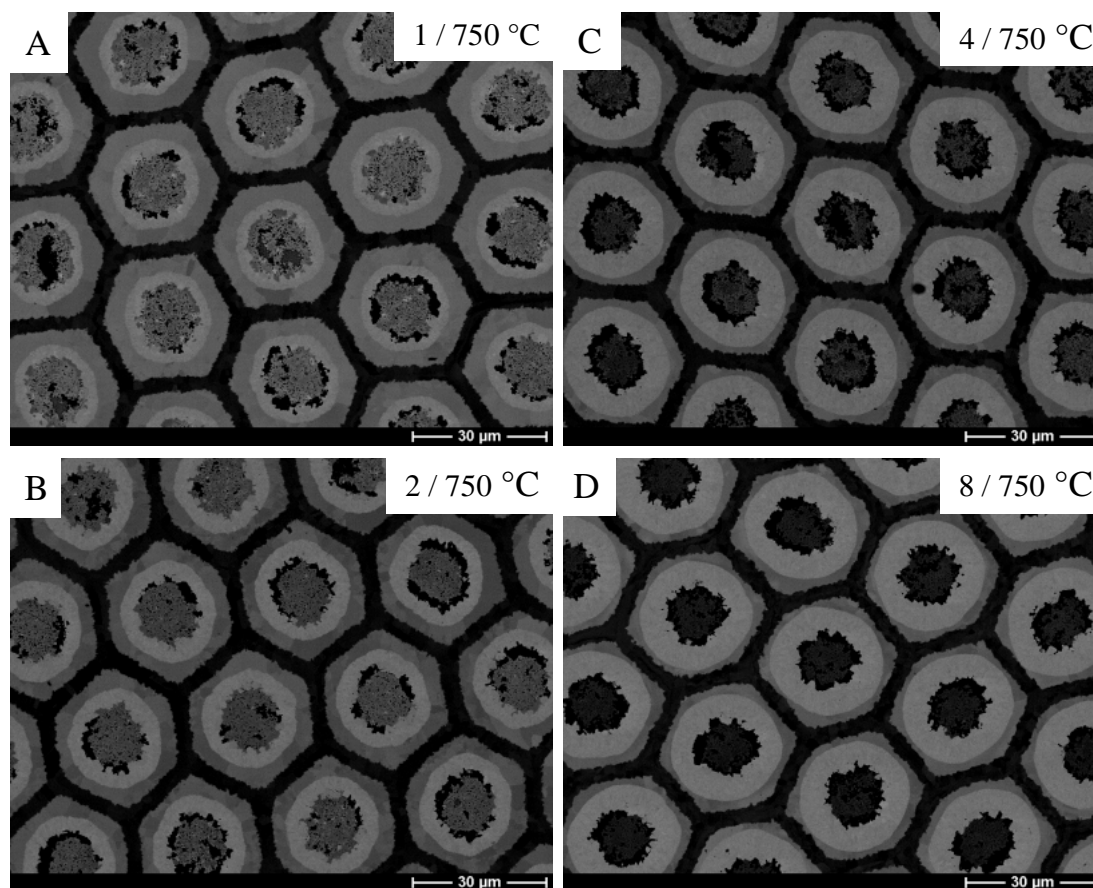


Fig. 3.5 Images A-D are atomic-number-sensitive backscatter electron images taken after the 1, 2, 4, and 8 hour heat treatments at 750 °C. Image A is after 1 hour, image B is after 2 hours, image C is after 4 hours, and image D is after 8 hours. The black matrix is Cu, the darker gray is Nb, and the lighter gray is Nb₃Sn.

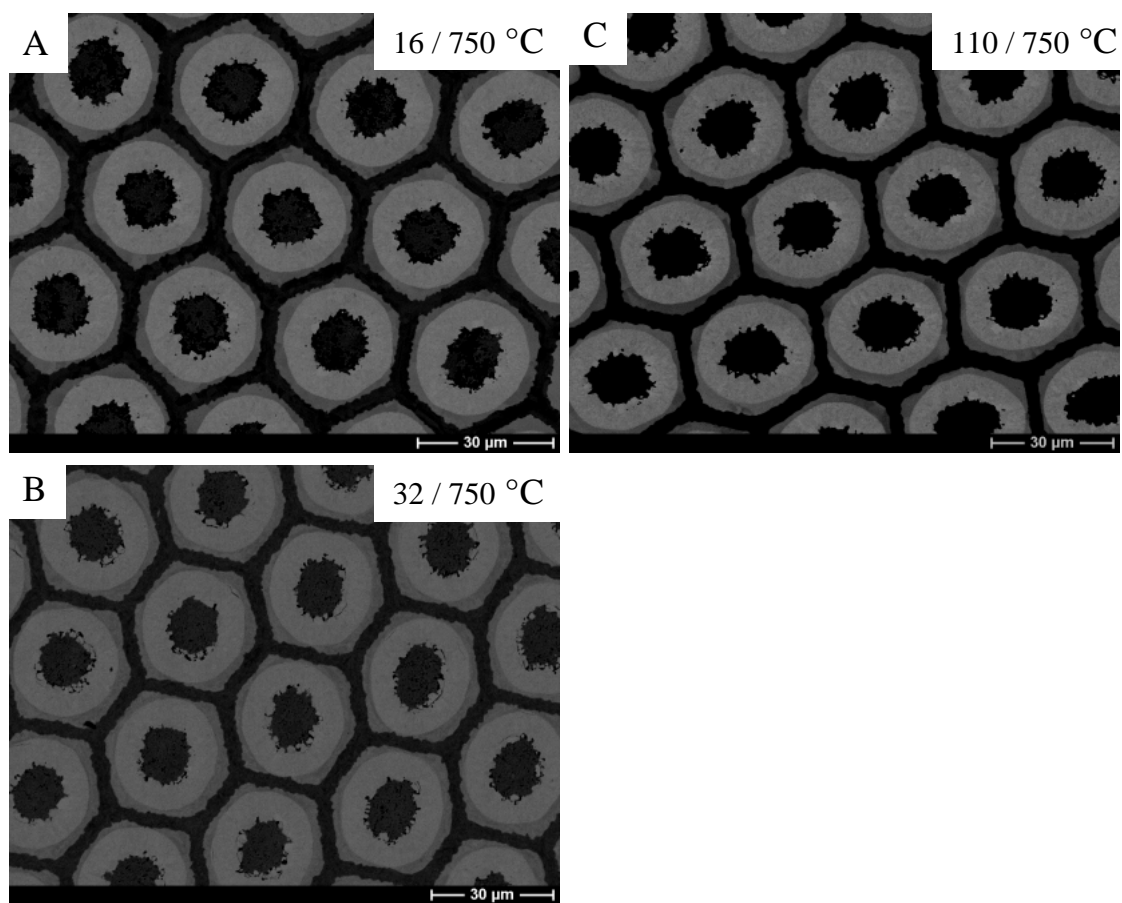


Fig. 3.6 Images A-C are atomic-number-sensitive backscatter electron images taken after the 16, 32, and 110 hour heat treatments at 750 °C. Image A is after 16 hours, image B is after 32 hours and image C is after 110 hours. The black matrix is the Cu, the darker gray region is the Nb, and the lighter gray region is Nb₃Sn.

The progress of the reaction at 750 °C of the powder core and the Nb is shown in Figs. 3.5 and 3.6. After 1 hour at 750 °C an A15 layer has grown and little or no Nb₆Sn₅ is visible. At 16 hours the layer is only slightly thicker than at 8 hours, and the A15 phase has reached the Nb-Cu interface.

From the BSE images, layer growth as a function of heat treatment time can be obtained for the 675 °C and 750 °C heat treatments, Figs. 3.7 and 3.8 respectively. The A15 layer thickness peaks at 47 hours for the 675 °C heat treatment and at 16 hours for the 750 °C heat treatment.

The fracture images in Figs. 3.9 and 3.10 show that both the 8 and 47 hour heat treatments at 675 °C have large grains near the core and finer grains as you proceed outward. After 8 hours at 750 °C the grain size is already larger than that at 47 hours at 675 °C. Continuing heat treatment times at 750 °C show that the grain size over the entire layer continues to grow, possibly on the order of the layer thickness, probably greater than 2 μm.

The results of the EDX analysis are shown in Figs. 3.11 and 3.12. Vertical error bars represent a 2σ (95% confidence) error based in the measured peak intensities, and the horizontal error bars are an estimate of the error in the measurement of the distance from the core to the measured point. The horizontal error bars are obtained from the variation in the core's shape and the spot size left on the layer from the electron beam interaction. The LEO-1530 exhibited stage drift over the course of the measurement. This stage drift resulted in the larger horizontal error bars for the 750 °C / 110 hour heat treatment. A gradient is seen in all measurements, with the shortest time having the steepest gradient. Longer heat treatment times do not show a change in Sn gradient, even though baselines are varying. A line was fit

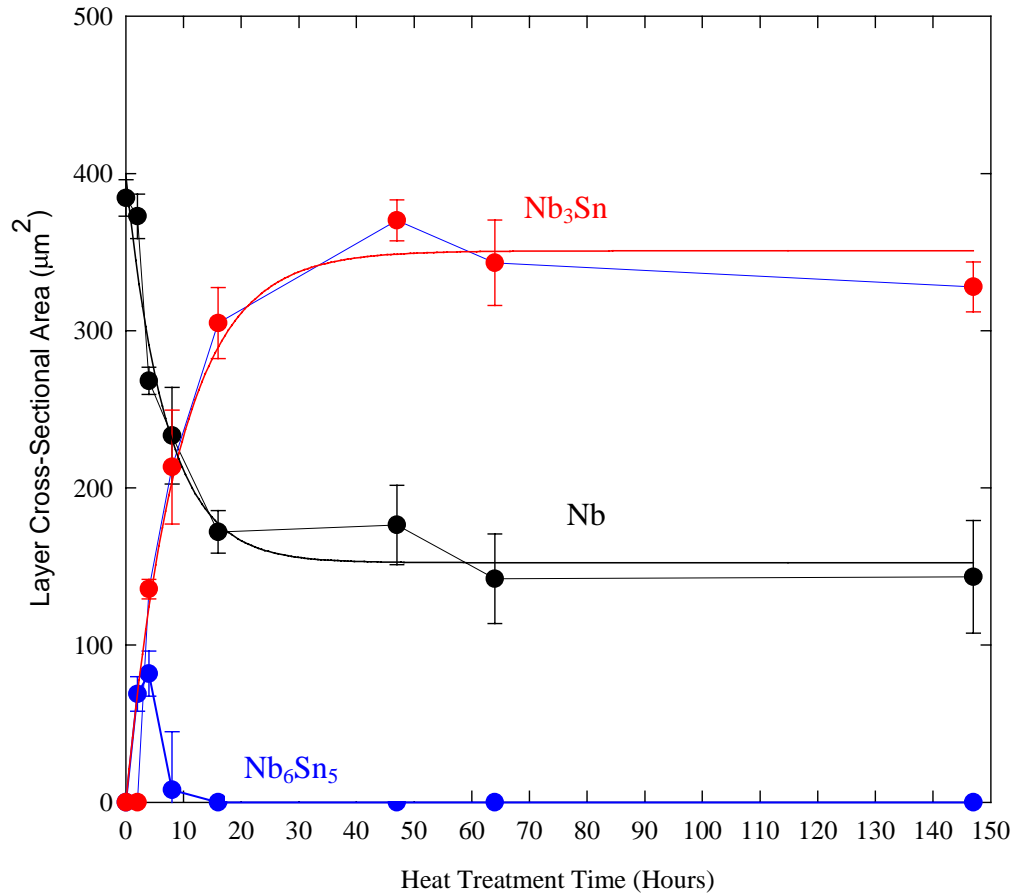


Fig. 3.7 Layer cross-sectional area as a function of heat treatment time for the 675 °C heat treatment.

to the each data set to determine the relationship between the gradient in the A15 layer and the heat treatment time. The fit to the 8 hour data produced a gradient of $-0.92 \text{ at.}\%/\mu\text{m}$, the 16 hour $-0.69 \text{ at.}\%/\mu\text{m}$, the 47 hour $-0.64 \text{ at.}\%/\mu\text{m}$, and the 110 hour $-0.37 \text{ at.}\%/\mu\text{m}$. There is also the possibility that the composition distribution in the samples heat treated at 675 °C is bimodal, due to the grain structure. This possibility will be taken up further in the discussion section.

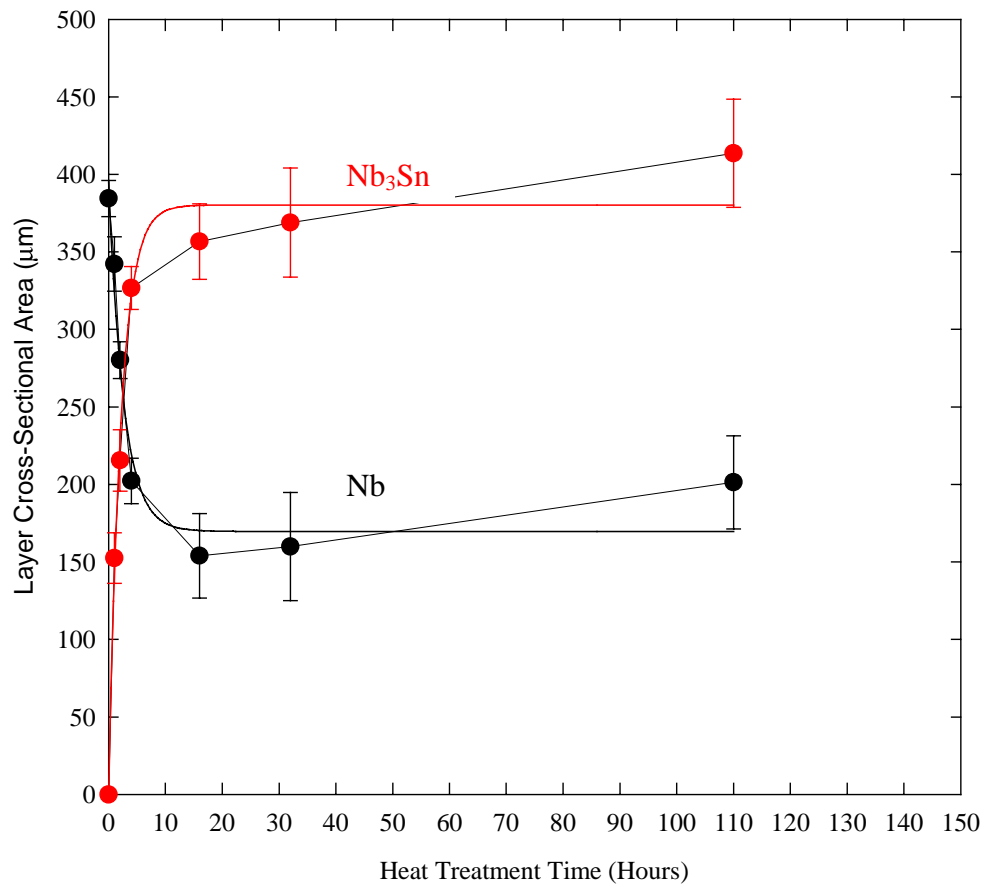


Fig. 3.8 Layer cross-sectional area as a function of heat treatment time for the 750 °C heat treatment.

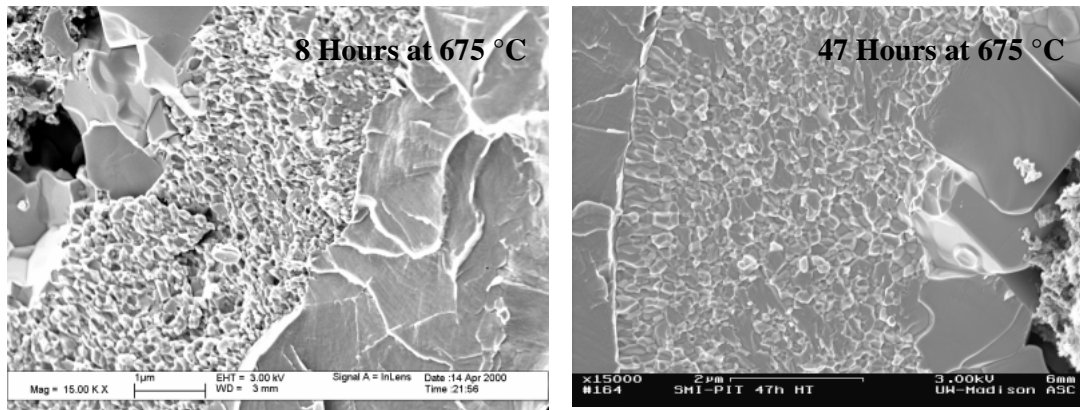


Fig. 3.9 Fracture images of the 8 and 47 hour heat treatments at 675 °C. Magnification is 15,000 \times . The 8 hour heat treatment has a much thinner layer, with much finer grains than the 47 hour heat treatment.

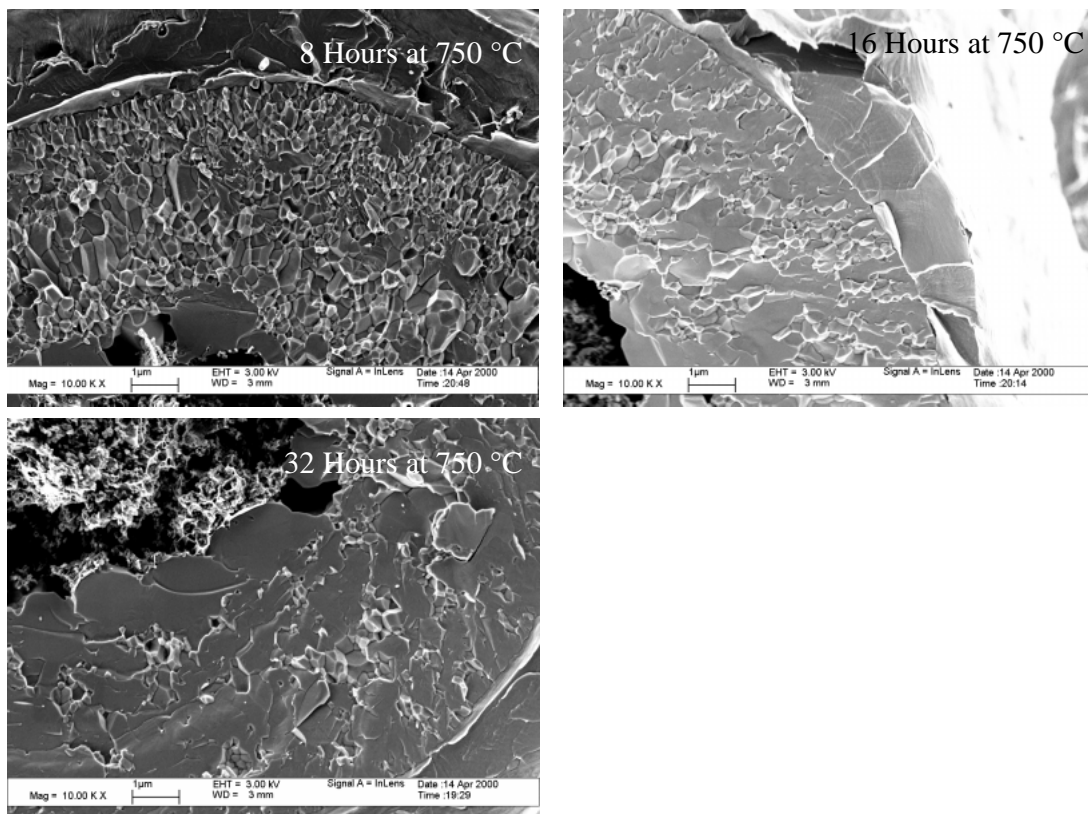


Fig. 3.10 Fracture images of the 8,16, and 32 hour heat treatments at 750 °C. Magnification is 10,000 \times . The 8 hour heat treatment has a much finer grain structure and thinner layer when compared to the 32 and 16 hour heat treatments. The grains in the 8 hour / 750 °C are coarser than those of the 47 hour / 675 °C heat treatment, Fig. 3.9.

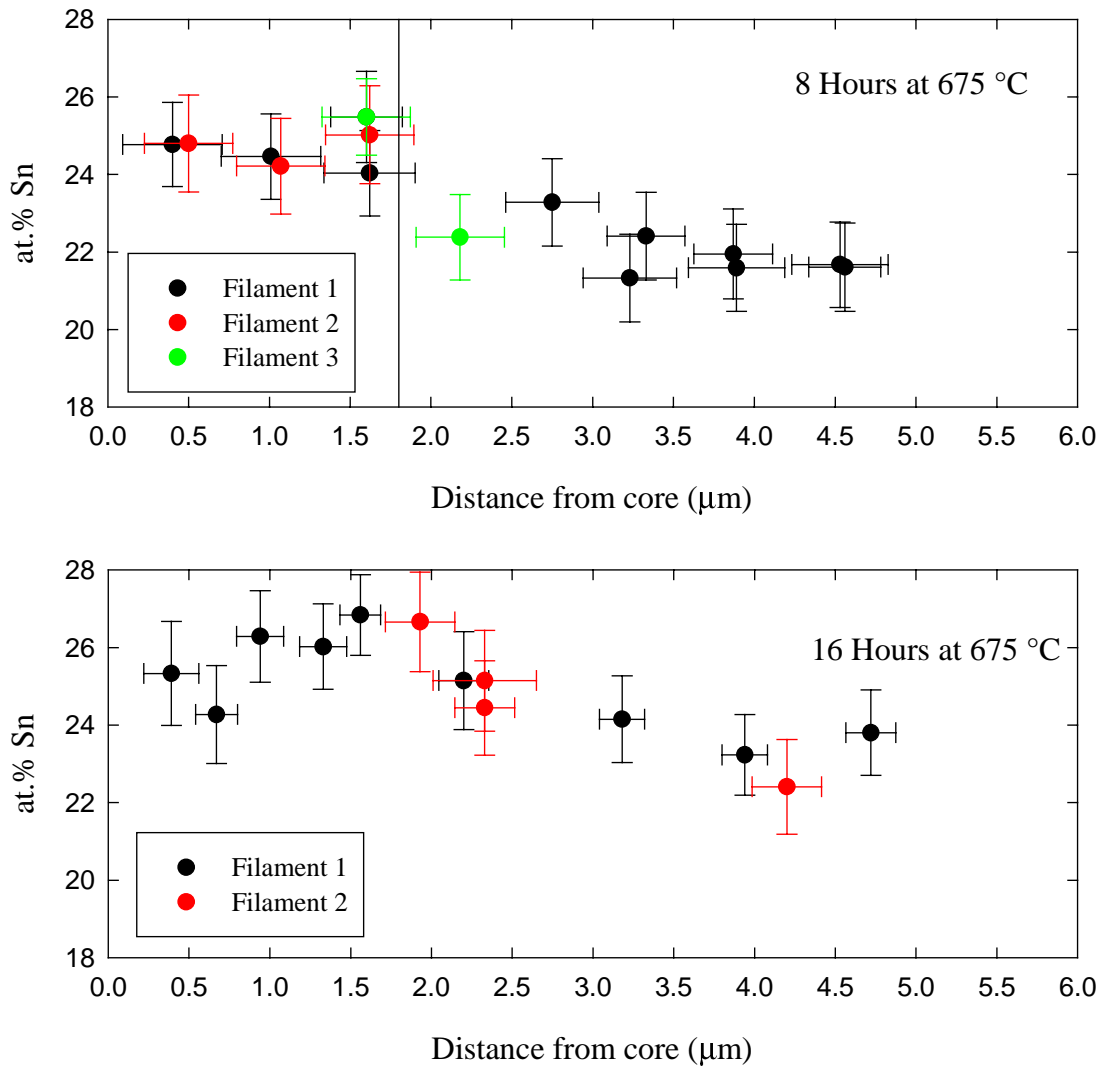


Fig. 3.11 The upper plot is the EDX analysis results for the 8 hour / 675 °C heat treatment. The vertical line is the average distance the large grains extend out from the core. This distance is obtained from the fracture image in Fig. 3.9. A line fit to the data points has a slope of $-0.92 \text{ at.}\%/\mu\text{m}$. The lower plot is the EDX analysis results from the 16 hour / 675 °C heat treatment. A line fit to the data points has a slope of $-0.69 \text{ at.}\%/\mu\text{m}$. Vertical error bars represent 2σ (95% confidence) error and horizontal error bars represent the uncertainty in the distance measurement.

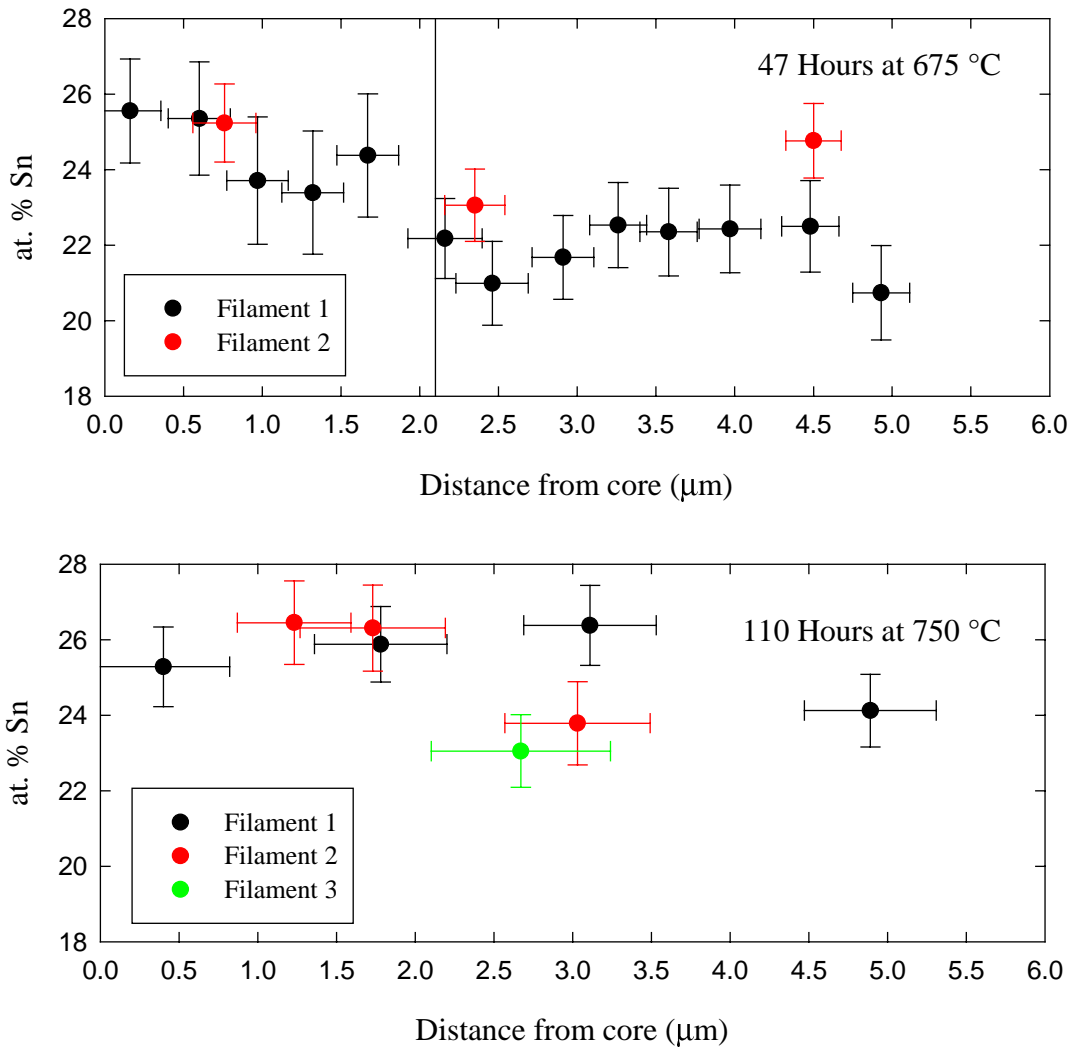


Fig. 3.12 The upper plot is the EDX analysis results for the 47 hour / 675 °C heat treatment. The vertical line is the average distance the large grains extend out from the core. This distance is obtained from the fracture image in Fig. 3.9. A line fit to the data points has a slope of $-0.64 \text{ at.}\%/\mu\text{m}$. The lower plot is the EDX analysis results from the 110 hour / 750 °C heat treatment. A line fit to the data points has a slope of $-0.37 \text{ at.}\%/\mu\text{m}$. Vertical error bars represent 2σ (95% confidence) error and horizontal error bars represent the uncertainty in the distance measurement.

3.3.2 Inductive Critical Temperature Measurements

The steady progress of the A15 layer growth for the 675 °C and 750 °C heat treatment is inferred from the critical temperature plots in Fig. 3.13 and Fig. 3.14, respectively. Full flux exclusion from within each filament was seen at 5 K, the first transition occurring at 9 K when the Nb sheath goes normal. Fig. 3.15 indicates that the “Nb transition temperature” decreases and broadens with heat treatment time. Apparently no significant A15 phase forms after 2 hours at 675 °C. This agrees with the backscatter electron images in Fig. 3.2. However, by 1 hour at 750 °C significant growth has occurred. At 675 °C and 750 °C, increasing heat treatment time results in a steady rise in maximum T_c , a thickening of the layer, and a flattening in the gradient of the A15 T_c profile. The obvious deviation from this trend is the apparent reversal of the layer growth in the 147 hour heat treatment at 675 °C, and the 32 hour and 110 hour heat treatments at 750 °C. At 47 hours a tail below ~ 14 K occurs, this tail also occurs below 9 K. Remember that the continuity of the Nb has now been breached and both Nb and A15 are visible, as shown in Fig. 3.4 A and B. The 64, 147, and 263 hour heat treatments also show this behavior.

The data in Fig. 3.16, 675 °C heat treatment $T_c(r)$ plot, shows that the 4-8 hour plots have a steeper slope, $T_c(r)$, and a slightly lower maximum T_c . Starting at 16 hours, $T_c(r)$ flattens and there is a general rise of T_c as continued layer growth occurs. The growth rate declines after the 16 hour heat treatment. At 47 hours a distinct tail appears in the T_c trace, this behavior is also seen in the 64, 147, 263 hour heat treatments. The apparent thinning of the A15 layer in the 147 hour heat treatment is also seen.

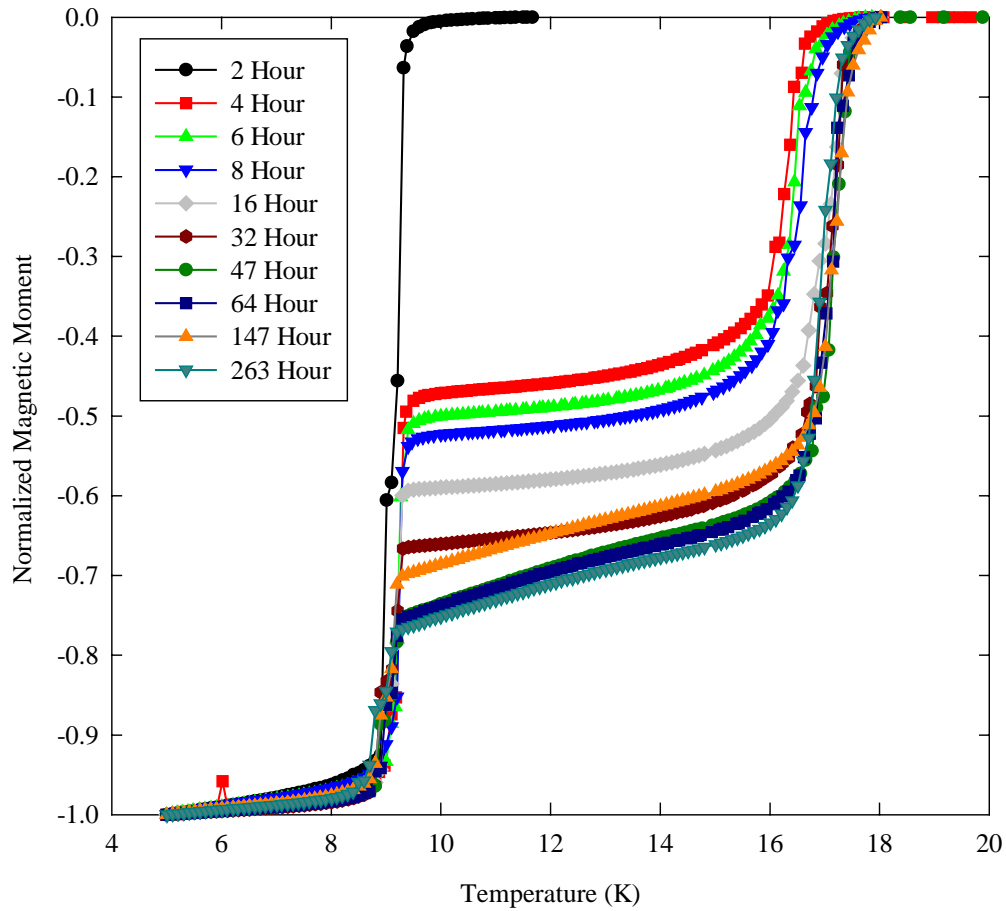


Fig 3.13 Magnetic moment curves for 675 °C heat treatment obtained by zero-field cooling to 5 K and then heating in a field of 1 mT.

In Fig. 3.17, 750 °C heat treatment $T_c(r)$ plot, the results are similar to the 675 °C heat treatment. The 1 and 2 hour plots have a steeper slope, $T_c(r)$, and a slightly lower maximum T_c . Starting with the 4 hour plot, $T_c(r)$ flattens and there is a general rise of T_c as continued layer growth occurs. No tail appears for longer heat treatment times, as is seen starting with the 47 hour heat treatment at 675 °C, but the broadening and shifting of the Nb transition is much more pronounced, and at 110 hours the shift is highly visible. The apparent thinning of the A15 layer in the 32 and 110 hour heat treatments is also seen.

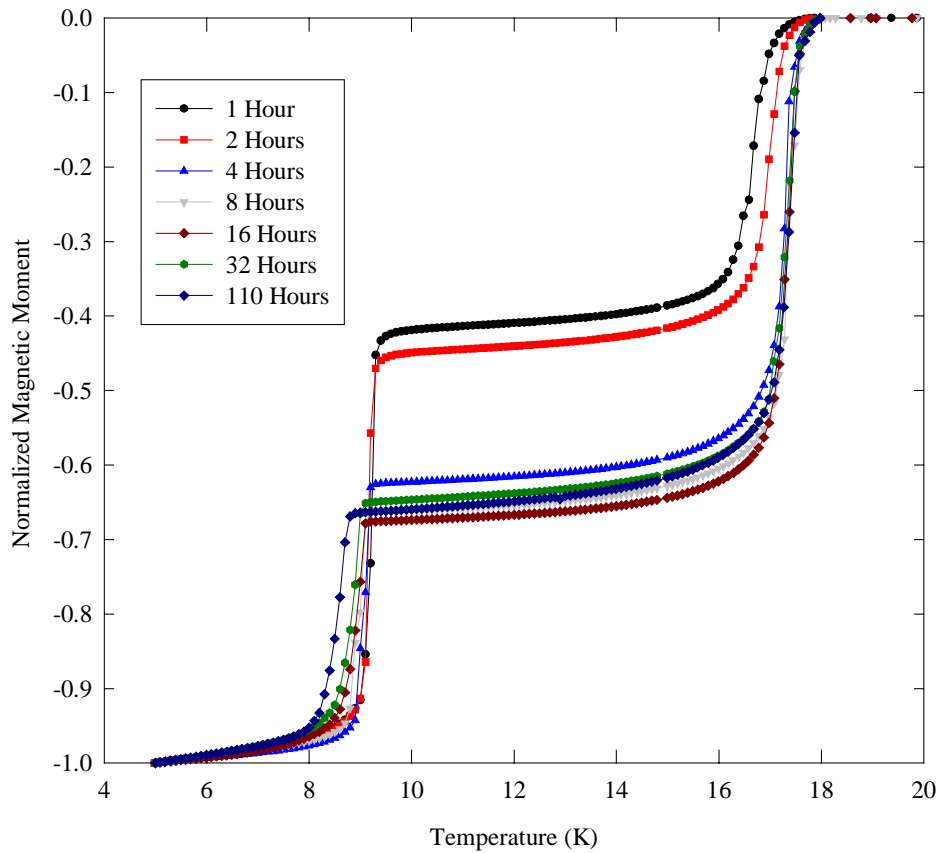


Fig. 3.14 Magnetic moment curves for the 750 °C heat treatment obtained by zero-field cooling to 5 K and then heating in a field of 1 mT.

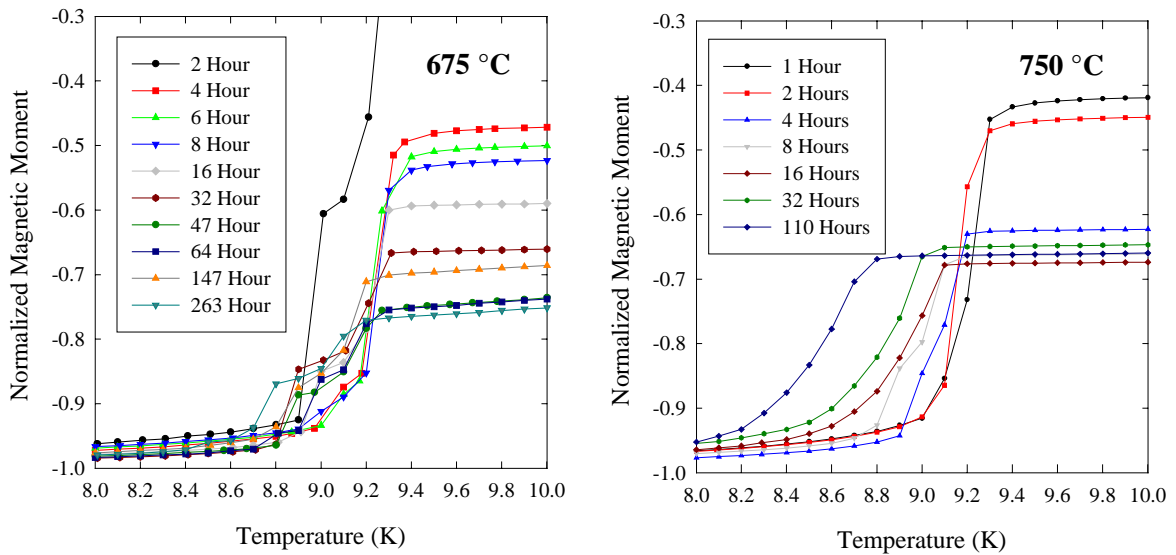


Fig. 3.15 8-10 K range for the 675 °C, left plot, and 750 °C, right plot, heat treatments. Bulk Nb transition ~ 9.2 K. The variation seen in the above plots is due to the formation of low-Sn A15.

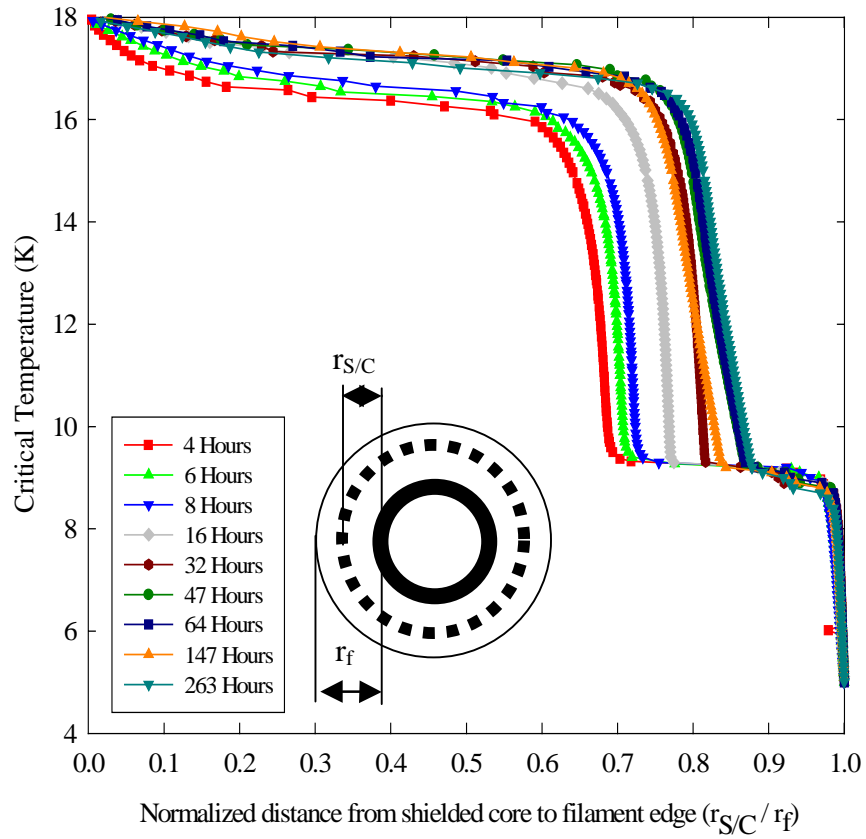


Fig 3.16 Reduced critical temperature versus radius for 675 °C heat treated PIT filaments assuming, (1) circular symmetry, (2) full Meissner shielding by the superconducting layer, and (3) a fully shielded core surrounded by the highest T_c layer.

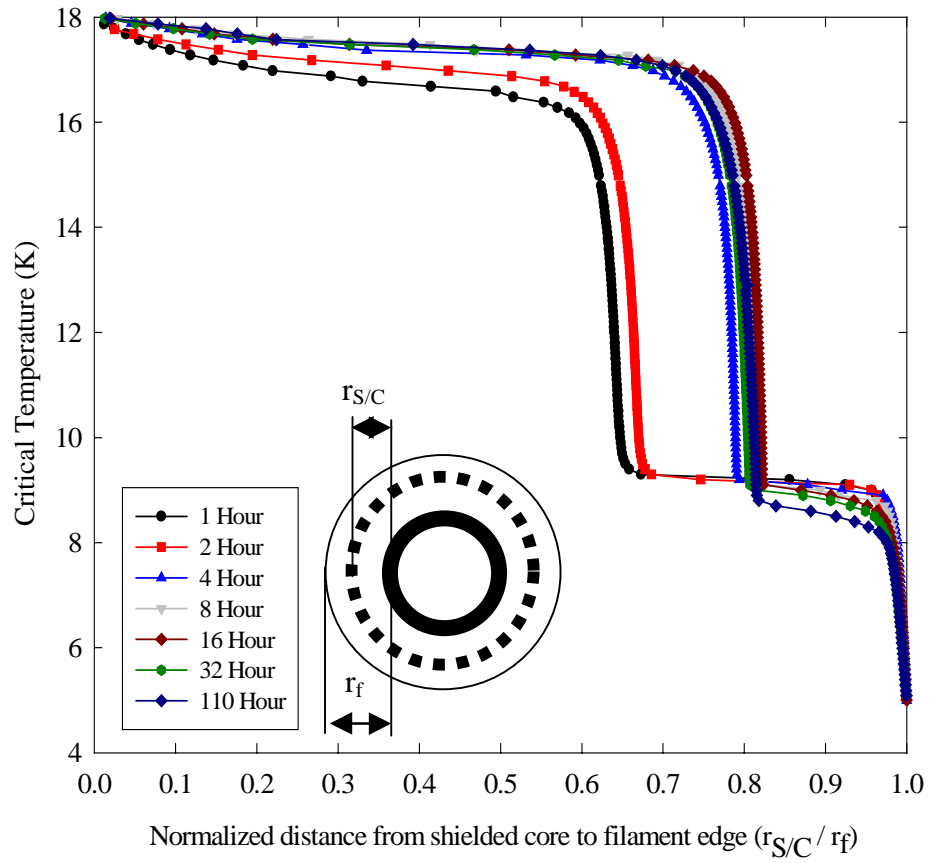


Fig. 3.17 Reduced critical temperature versus radius for the 750 °C heat treated PIT filaments assuming, (1) circular symmetry, (2) full Meissner shielding by the superconducting layer, and (3) a fully shielded core surrounded by the highest T_c layer.

3.3.2 Heat Capacity Measurements

The differences in the magnitudes of the heat capacity curves in Figs 3.18 and 3.19, 675 °C and 750 °C heat treatments, respectively, are due to the differences in each sample's mass. Both figures show that increasing heat treatment time results in a more pronounced transition which moves toward higher temperatures. Fig. 3.20 shows that the Nb transition broadens and moves toward lower critical temperatures, reinforcing the inductive critical temperature data of Fig. 3.15.

A better illustration of the effect of heat treatment time and temperature is given in Figs. 3.21 and 3.22, 675 °C and 750 °C heat treatments, respectively. The data in both plots have been divided by the sample's mass and have had the background signal subtracted from the total signal to obtain only the signal due to the A15 layer. The procedure for doing this is given in the Appendix, section 5.2. Increasing heat treatment time results in a sharper transition, with an increase in the critical temperature of the material over the layer, and in the maximum critical temperature. From Figs. 3.21 and 3.22 it can be seen that the amount of A15 material increases with heat treatment time, and that for both temperatures, they reach approximately the same maximum thickness, maximum heat capacity. It just occurs much faster in the 750 °C heat treatment.

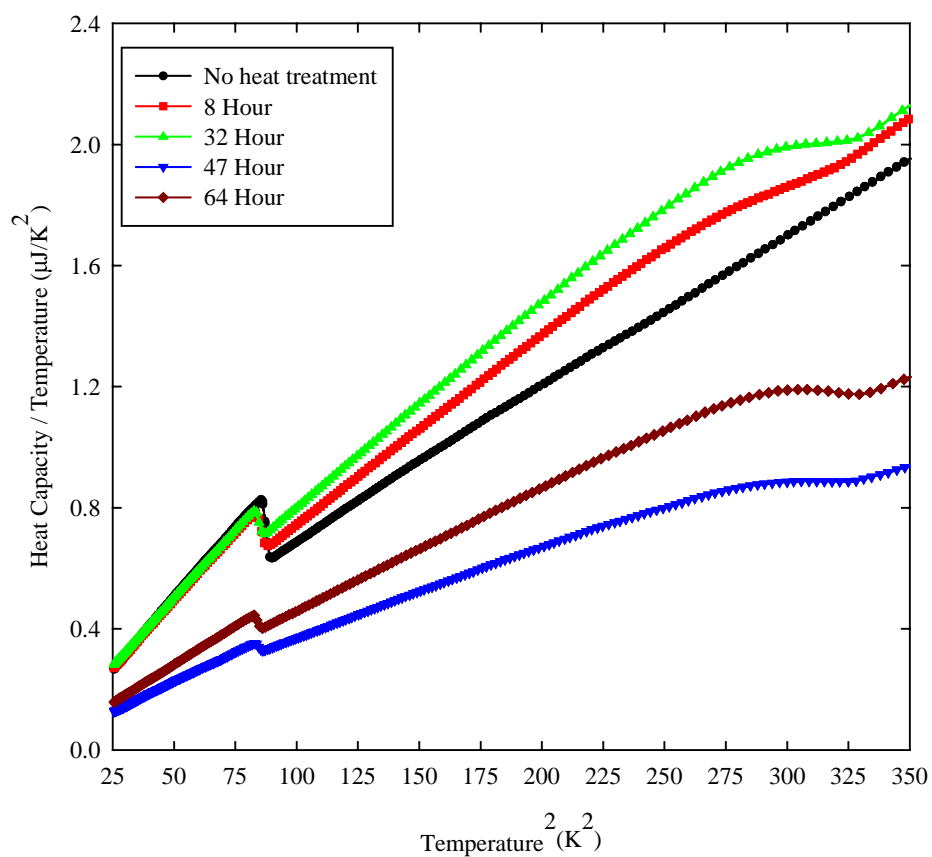


Fig. 3.18 Heat capacity for 675 °C heat treatment. Distribution of sample curves due to differences in sample masses, i.e., the 32 hour sample had the greatest mass and the 47 hour had the smallest mass. With heat treatment time, the A15 transition (~275-325 K²) becomes sharper and moves to the right.

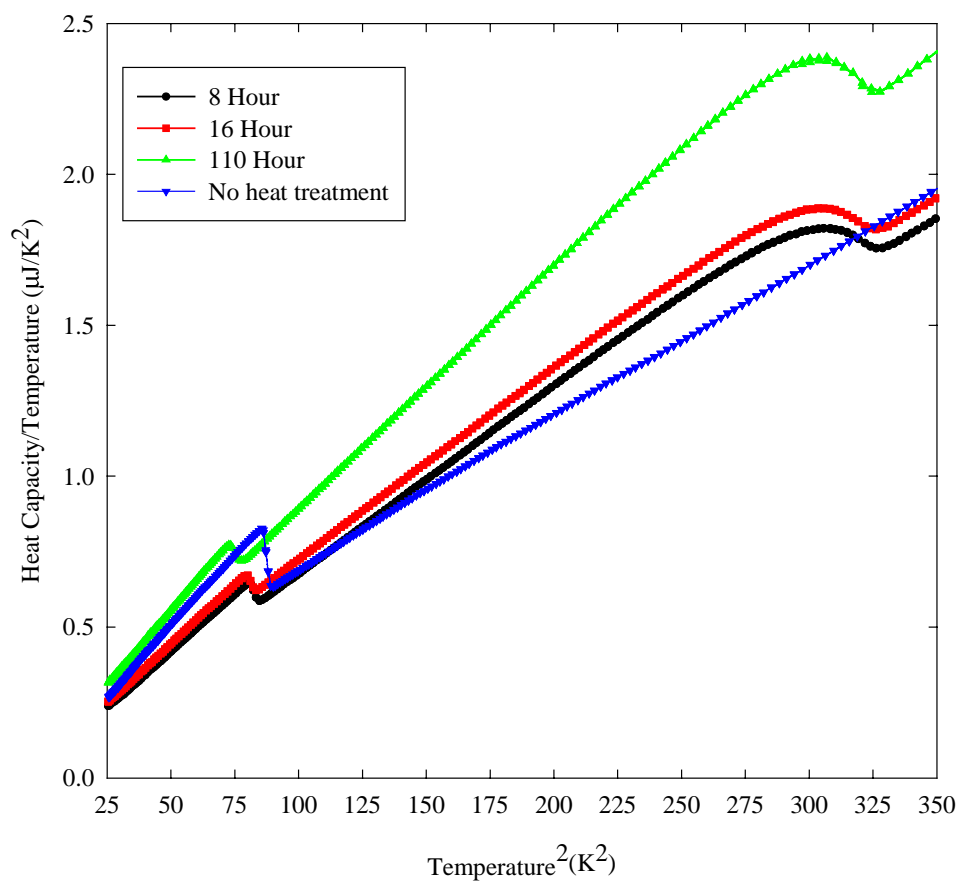


Fig. 3.19 Heat capacity for the 750 °C heat treatment. Distribution of sample curves due to differences in sample masses, i.e., the 110 hour sample had the greatest mass and the 8 hour sample had the smallest mass. With heat treatment time, the A15 transition (~275-325) becomes sharper and moves to the right.

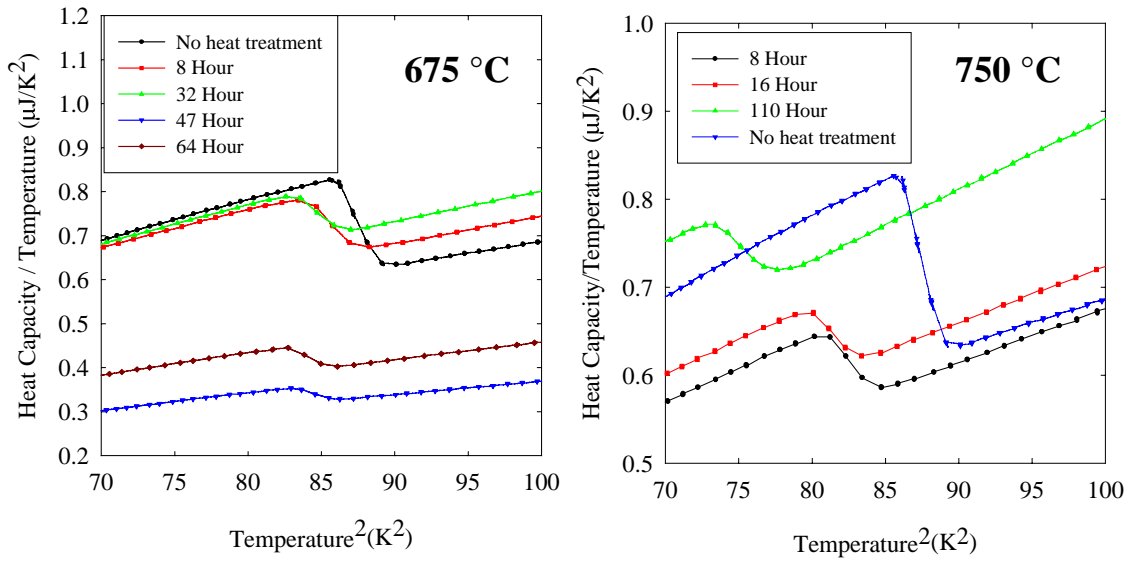


Fig. 3.20 8.4-10 K range for the 675 °C, left plot, and 750 °C, right plot, heat treatments. Bulk Nb transition is ~ 9.2 K. The variation seen in the transitions is due to the formation of low-Sn A15.

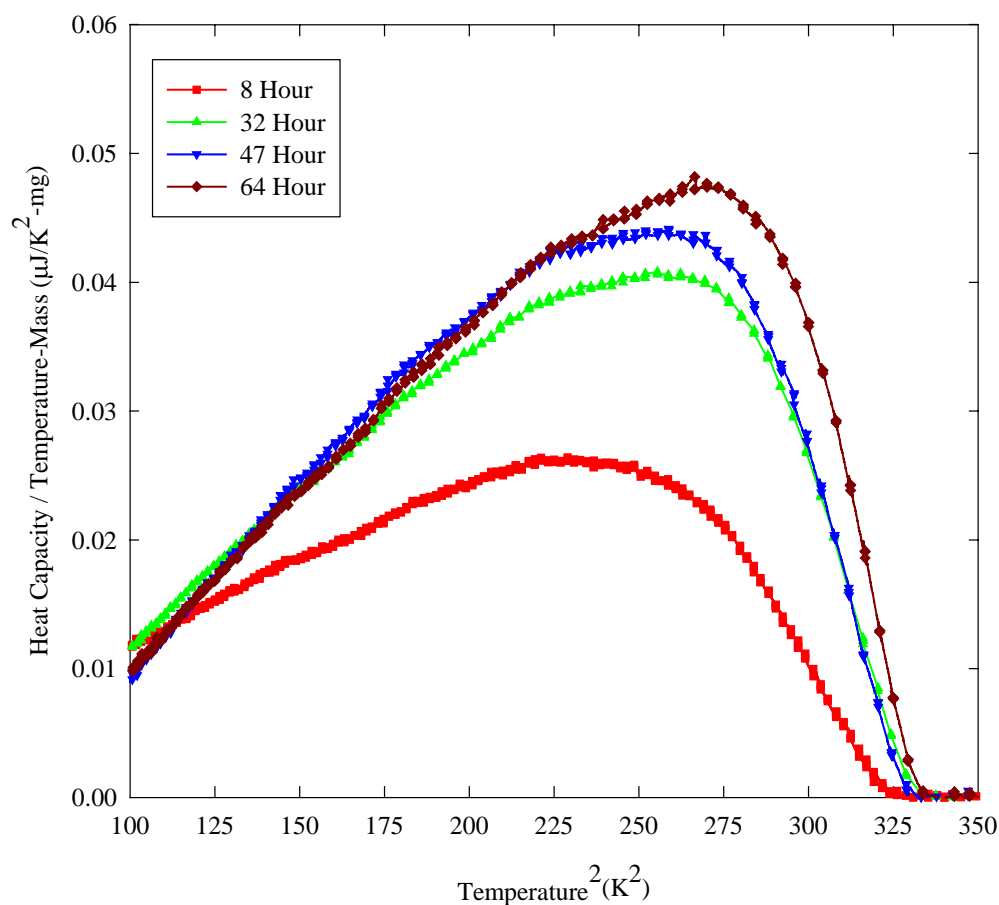


Fig. 3.21 675 °C heat treatment heat capacity data for only the superconducting A15 layer. Heat capacity data to non-A15 material has been subtracted from the raw data, see Appendix section 5.2. Transitions become sharper, move towards higher temperatures, and grow in magnitude with increasing heat treatment time. The differences in the magnitude of the curves are due to increases in the amount of superconductor, not to differences in the total sample mass as in Figs. 3.18 and 3.19.

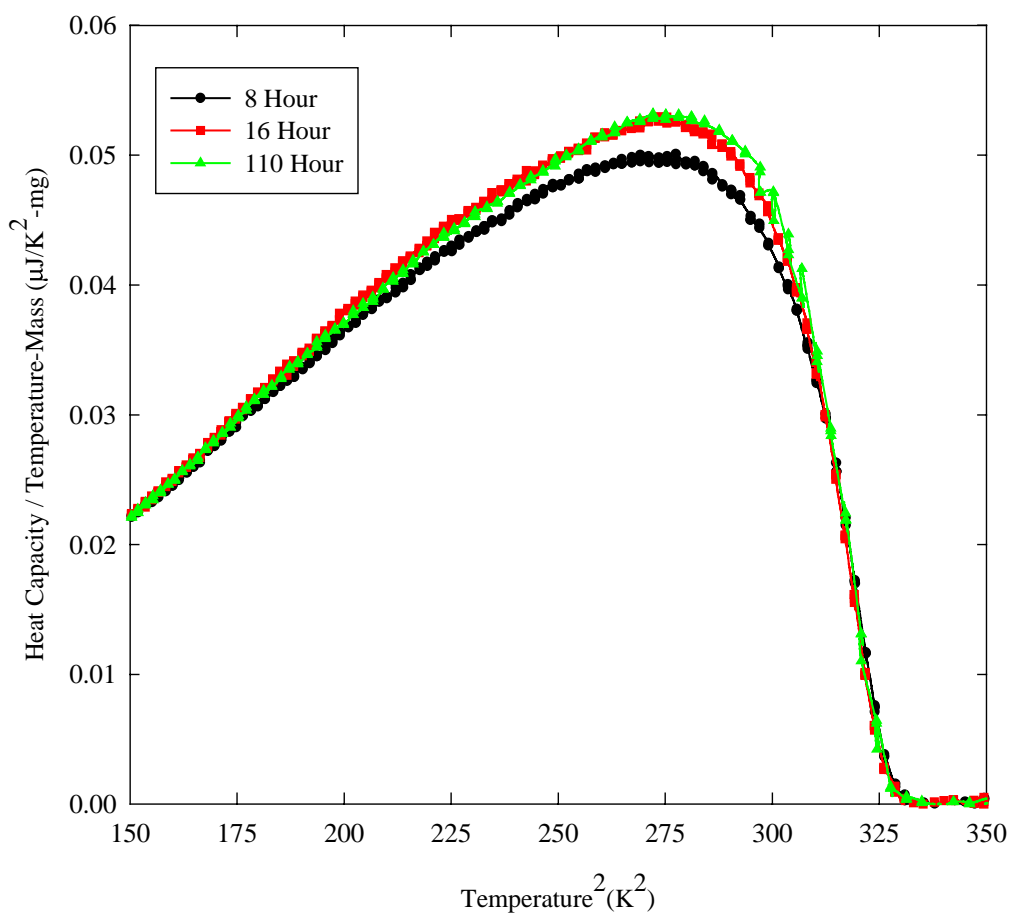


Fig. 3.22 750 °C heat treatment heat capacity data for only the superconducting A15 layer. Heat capacity due to non-A15 material has been subtracted from the raw data, see Appendix section 5.2. Transitions become sharper, move towards higher temperatures, and grow in magnitude with increasing heat treatment time. The differences in the magnitudes of the curves are due to increases in the amount of superconductor, not to differences in the total sample mass as in Figs. 3.18 and 3.19.

3.4 Discussion

An underlying issue in studies of Nb₃Sn is how much more compositionally uniform can the filaments be made and, if they could be made more uniform, how much this would benefit the properties. In fact, the direct correlation of superconducting properties to the local composition of Nb₃Sn filaments is rare [44]-[46] and the results are ambiguous. The fact that a high performance PIT conductor has a magnetically transparent design, a Nb₃Sn layer thick enough to measure by electron probe analysis, and the ability to measure the critical temperature transition using heat capacity is what prompted our interest in renewed study of this issue. These results show that this type of conductor has undoubted advantages for such studies.

Nb₆Sn₅ forms very rapidly, appearing after 2 hours at 675°C and being fully consumed after 16 hours. This is also observed by Veringa, et al. [40]. This rapid reaction helps grow a 5 μm thick A15 layer in approximately 8 hours, a much thicker and more rapidly grown layer than can be formed by bronze or internal Sn processes. This rapid growth is a distinct advantage from many points of view.

The Nb-Sn phase diagram, Fig. 1.12, suggests that the composition of the A15 should lie over the range 25.5 to 18 at. % Sn, causing a T_c variation from 18 to 6 K across such a non-equilibrated layer [17], [36]. How the composition gradient is established across the A15 layer matters greatly, since this should determine the volumetric distribution of T_c , J_c , and B_{c2} . In fact, the results of Figs. 3.11 and 3.12 suggest a linear gradient from 25-25.5 to only 21 at. % over most of the A15 layer, the composition only diving to lower Sn values very close to the A15-Nb or A15-Cu interface. This small variation is supported by the results of the inductive critical temperature plots of Figs.

3.16 and 3.17 which show that the bulk of the change in T_c occurs over the range 18 to ~14 K. Formally, these findings are not what we would expect from the results of [17], [36], which would suggest that a Sn composition of 21 at. % corresponds to a T_c of ~9 K. Thus the influence of the measured composition gradient on the superconducting properties appears to be less severe than expected.

The T_c profile does show a greater broadening at the A15-Nb or the A15-Cu interface with heat treatment time. This broadening extends to the “Nb transition” with heat treatment time and temperature, Figs. 3.15 and 3.20. Since the solubility of Sn in Nb at 675 °C and 750 °C is almost nil (see Nb-Sn phase diagram, Fig. 1.12), the variation is due to Sn-poor A15, and not Nb with a small percent of dissolved Sn. The smearing of the Nb transition could then be explained as a combination of Sn-poor A15, and what little Nb is left after the longer heat treatments. Unfortunately, the spatial resolution of the EDX is not good enough near the Nb-A15 boundary to determine the concentration of Sn, so exact knowledge of why the low temperature transition changes is unavailable.

In fact, a striking feature of this PIT conductor is that high layer J_c values are obtained. Optimum reaction, yielding a non-Cu $J_c(13T)$ of 1274 A/mm² (Layer $J_c = 2450$ A/mm²), was reported to be 47 hours at 675°C [2]. However, it is clear that this reaction causes partial breakthrough of the A15 phase to the Cu matrix, smearing and extending the T_c transition. Thus it seems plausible to expect that significantly better A15 layer properties could be obtained by the PIT process if the composition gradient and its associated T_c and B_{c2} gradient were ameliorated. It is true that the PIT process has an in-built gradient so long as the Nb layer is capable of being brought next to the A15 layer.

However, PIT conductors are by no means unique in being inhomogeneous. Virtually all A15s are inhomogeneous, even with excess Sn. In the study by Marken, et al. [44] on a 4:1 Sn:Nb ratio bronze conductor, a clear benefit for B_{c2} of very extended reactions was seen, but the same reactions (>500 hours) so increased the grain size that J_c was strongly suppressed. Here the slow reaction kinetics of the bronze process appear to harm the flux pinning properties of the Nb₃Sn. In a recent study of ITER and high Sn internal Sn conductors by Lee, et al. [47], Nb₃Sn layer J_c values in filaments made in different ways are quite variable. A15 layer $J_c(13T)$ values of 1600-1950 A/mm² were obtained for bronze and internal Sn ITER conductors, as compared to a value of 2450 A/mm² deduced from J_c measurements by den Ouden [1] on the present PIT conductor. Only a very high Sn (TWC1912), internal Sn conductor achieved a slightly better value of >2800 A/mm² at 13 T.

The fracture images, Fig. 3.9, of the 675 °C heat treatment show coarse grain A15 near the core and a finer grained A15 as you move outward. The EDX data, Figs. 3.11 and 3.12, for the 675 °C heat treatment appears to have a constant composition, or a gradient up to 2 μm, which is approximately the size of the coarse grains. Earlier work with the PIT method [39],[40] show that two grain sizes occur, coarse grains near the core and finer grains as you move outward from the core. Veringa, et al. asserts that the large grain A15 is formed in the presence of a liquid bronze phase, which maybe the reason the grains are so large. This is possible given the reaction temperature for the composite. Veringa, et al. also states that two different values for the critical temperature are found by Suenaga, one at 17.7 K for the fine grained A15 and one at 18.2 K for the coarse grained A15. The reference for the Suenaga results is a personal communication,

so no information as to how these results were obtained is given. The EDX results from the 110 hour / 750 C heat treatment show a gradient which is fairly flat across the layer, the grain size is also much larger, possibly on the order of the layer thickness, probably greater than 2 μm . The large grain size may be the reason why there is no evidence for two composition gradients in the 110 hour / 750° C heat treatment.

The deconvolution of T_c employed here is not very satisfactory in spatial terms, because the assumption of full shielding is not valid for thin layers where T_c is rapidly changing. To fulfill the condition of full Meissner shielding in each shell, about 20 penetration depth (λ) thickness layers are needed. In principle, a rigorous calculation could be done, but in fact knowledge of λ (Sn content) is not known, so such a calculation would hardly be definitive in yielding the radial variation of T_c . Another defect of using a magnetic deconvolution of T_c is that the radial extent of the superconducting layer in Figs. 3.16 and 3.17 is extended due to the shielding of the core. It is clearly seen in the BSE images that the core takes up half the radial distance from the center of the filament to the outside edge of the filament, while the results of the inductive measurements make it appear that the A15 layer is much thicker. From the 147 hour heat treatment in Fig. 3.16 and the 32 and 110 hour heat treatments in Fig. 3.17, it would appear that the A15 layer has thinned compared to the other heat treatments. Backscatter electron images show this not to be the case, and looking at the inductive critical temperature measurements we see that maximum critical temperature has not changed and that the gradient is similar to the rest. Changes in λ near the A15-Nb boundary, thus changing the shielding effects at the interface, may be the cause of this apparent thinning of the A15 layer.

3.5 Conclusions

After viewing the results of this experiment, one may ask, why not perform the heat treatments at 750 °C and obtain a flatter gradient in the critical temperature profile in a shorter amount of time? The reason this is not done is due to the trade-off between the improved composition gradient and a larger grain size in the A15 layer. Maximization of the critical current density at 4.2 K in the 12 to 15 T range involves optimization of the primary superconducting properties, T_c and H_{c2} , and the flux pinning properties of the A15 layer. At the manufacture's recommended heat treatment, 675 °C for 47 hours, there appears to be an empirical optimization which produces a fine grain size, which produces strong flux pinning / J_c , and an acceptably high Sn content and small composition gradient giving high T_c and H_{c2} .

The inductive critical temperature measurements have allowed us to see the growth of the A15 layer in this PIT conductor. The $T_c(r)$ plots obtained from the inductive critical temperature measurements are in agreement with the EDX results. Both results show changes in the composition and critical temperature that coincide well with each other. Some of the drawbacks of this technique are that the information we obtain is semi-quantitative/qualitative due to our lack of knowledge of how λ varies with Sn content and the effect of the shielding of the core by the high Sn material. Another drawback is that this technique can only be used on samples that are magnetically transparent, where the material has the high Sn A15 on the inside and the low Sn A15 on the outside.

The heat capacity measurement technique can be used on any sample geometry, and provides information on the quality of the growing A15 layer along with information on the relative amounts of material being grown. The heat capacity measurement's only drawback is that the information contains no spatial data.

The most surprising, and pleasant, results of this study are that most of the composition gradient occurs at the A15-Nb interface, and that the gradient in most of the layer is flat and of a high quality, high T_c , material. Also, the strong sensitivity of both composition and grain size to heat treatment conditions, provides the potential for further property improvements.

4. References

1. A. den Ouden, S. Wessel, E. Krooshoop, and H. ten Kate, *IEEE Transactions on Applied Superconductivity*, vol. 7, pp. 733-738 (1997).
2. Personal communication between Dr. Peter Lee and ShapeMetal Innovations, Holland.
J.H. Lindenhovius, E. M. Hornsveld, A. den Ouden, W. A. J. Wesswl, and H. H. J. ten Kate, *IEEE Transactions on Applied Superconductivity*, vol. 9, pp. 1451-1454 (1999).
3. K. Tachikawa, M. Natsuume, Y. Kuroda, and H. Tomori, *Cryogenics*, vol. 36, pp. 113-117 (1996).
4. *American Society of Metals: Metals Handbook, Superconductor Materials Science*, 10th edition, vol. 2, pp. 1060-1076 (1990).
5. E.A. Lynton, *Superconductivity*, John Wiley and Sons Inc., New York (1964).
6. M. Tinkham, *Introduction to Superconductivity*, R.E. Krieger Publishing Company, New York (1980).
7. K.J. Faase, *Microstructures and Properties of Nb/Ti Multilayered Thin Films*, Ph.D thesis, Oregon State University (1996).
8. H. Ullmaier, *Irreversible properties of Type II superconductors*, *Springer Tracts in Modern Physics*, Springer-Verlag, Berlin (1975).
9. B.T. Matthias, *Physical Review*, vol. 97, pp. 74-76 (1955).
10. D.B. Samthers, *Profile of a Superconductor-Niobium Stannide*, Ph.D proposal, University of Wisconsin-Madison (1981).
11. J. Labbe and E.C. van Reuth, *Physical Review Letters*, vol. 24, pp. 1232-1235 (1970).

12. M. Soll, K. Boning, and H. Bauer, *Journal of Low Temperature Physics*, vol. 24, pp. 631-643 (1976).
13. B.D. Cullity, *Elements of X-Ray Diffraction*, Addison-Wesley (1978).
14. A. Junod, et al., *Solid State Communications*, vol. 19, pp. 265-267 (1976).
15. R. Flukiger and J.L. Jorda, *Solid State Communications*, vol. 22, pp. 109-112 (1977).
16. R. Mailfert, B.W. Batterman, and J.J. Hanak, *Physics Letters*, vol. 24A, pp. 315-316 (1967).
17. H. Devantay, et al., *Journal of Materials Science*, vol. 16, pp. 2145-2153 (1981).
18. J.P. Charlesworth, I. Macphail, and P.E. Madsen, *Journal of Materials Science*, vol. 5, pp. 580-603 (1970).
19. *Constitution of Binary Alloys 2nd Supplement*, McGraw-Hill, New York, pp 203-207 (1969).
20. R.E. Enstrom, J.J. Hanak, and G.W. Cullen, *RCA Review*, vol. 31, pp. 702-714 (1970).
21. F.R. Nyman, *RCA Superconductive Materials and Magnets*, pp. 7-9 (1967).
22. G.W. Cullen, *Trans. of the Metallurgical Society of AIME*, vol. 240, pp. 1494-1499 (1964).
23. J.J. Hanak, G.D. Cody, P.R. Aron, and H.C. Hitchcock, *Some Physical Properties of Deposited Nb₃Sn*.
24. J.E. Kunzler, et al., *Physical Review Letters*, vol. 6, pp. 89-91 (1961).
25. M.G. Benz, *IEEE Transactions on Magnetics*, vol. 2, pp. 760-764 (1966).
26. D.B. Smathers, et al., *IEEE Transactions on Magnetics*, vol. 19, pp. 1417-1420 (1993).
27. M. Suenaga, et al., *IEEE Transactions on Magnetics*, vol. 11, pp. 231-237 (1975).
28. M. Thoner, et al., *IEEE Transactions on Magnetics*, vol. 27, pp. 2027-2032 (1991).

29. Thoner, et al., Erice (1996).
30. K. Tachikawa and Y. Iwasa, *Applied Physics Letters*, vol. 16, pp. 230-231 (1970).
31. K. Osamura and S. Ochiai, *Proceedings of the 18th International Conference on Low Temperature Physics, Japanese Journal of Applied Physics*, vol. 26, pp. 1519-1520 (1987).
32. K. Tachikawa, et al., *Advances in Cryogenic Engineering: Materials*, vol. 34, pp. 585-592 (1988).
33. M. Suenaga and W.B. Sampson, *Applied Physics Letters*, vol. 20, pp. 443-445 (1972).
34. A.D. McInturff and D.C. Larbalestier, *IEEE Transactions on Magnetics*, vol. 11, pp. 259-262 (1975).
35. Y. Zhang, et al., *IEEE Transactions on Applied Superconductivity*, vol. 9, pp. 1444-1446 (1999).
36. S. Foner and B. Schwartz, *Superconducting Materials Science: Metallurgy, Fabrication, and Applications*, Plenum Press, New York (1980).
37. C.A.M van Beijnen and J.D. Elen, *IEEE Transactions on Magnetics*, vol. 15, pp. 87-90 (1979).
38. J.H. Lindenhovius, et al., *IEEE Transactions on Applied Superconductivity*, vol. 9, pp. 1451-1454 (1999).
39. H. Veringa, et al., *Advances in Cryogenic Engineering Materials*, vol. 30, pp. 813-821 (1984).
40. H. Veringa, et al., *IEEE Transactions on Magnetics*, vol. 19, pp. 773-776 (1983).
41. J.D. Elen, et al., *IEEE Transactions on Magnetics*, vol. 17, pp. 1002-1005 (1981).

42. K. Tachikawa, et al., Preprint from International Cryogenics Materials Conference, Montreal (1999). To be published in *IEEE Transactions on Applied Superconductivity*.
43. A.C.A van Wees, P. Hoogendam, and H. Veringa, *IEEE Transactions on Magnetics*, vol. 19, pp. 556-559 (1983).
44. K.R. Marken, et al., *Advances in Cryogenic Engineering Materials*, vol. 32, pp. 967-975 (1986).
45. J.E. Evetts, et al., *IEEE Transactions on Magnetics*, vol. 17, pp. 360-363 (1981).
46. J.R. Cave and C.A.F. Wier, *IEEE Transactions on Magnetics*, vol. 19, pp. 1120-1123 (1983).
47. P. Lee, A. Squiteri, and D.C. Larbalestier, "Nb₃Sn: macrostructure, microstructure, and property comparison for bronze and internal Sn process strands" in press.
48. M. McElfresh, *Fundamentals of Magnetism and Magnetic Measurement: Featuring Quantum Design's Magnetic Property Measurement System*, Quantum Design (1984).
49. M. McElfresh, S. Li, and R. Sager, *Effects of Magnetic Field Uniformity on the Measurement of Superconducting Samples*, Quantum Design (1996).
50. R.A. Swalin, *Thermodynamics of Solids*, John Wiley & Sons, New York (1972).
51. A. Gurevich, *Extraction of the Volumetric Distribution Function $F(T_c)$ in A15 Composites From Specific Heat Measurements*, presentation at the University of Wisconsin-Madison for DOE-High Energy Physics site visit (2000).
52. *Quantum Design PPMS Hardware and Options Manual*, Quantum Design (1998).
53. R. Bachmann, et al., *The Review of Scientific Instruments*, vol. 43, pp.205-214 (1972).
54. D.L. Martin, *Physical Review*, vol. 141, pp. 576-582 (1966).

5. *Appendix*

5.1 Quantum Design SQUID Magnetometer – Inductive Critical Temperature Measurements

An explanation of how the SQUID magnetometer makes a measurement and how these measurements are applied to obtain our results will be useful in understanding the results of this experiment. A 5-7 mm long section of the SMI wire is mounted onto the sample transport rod. The sample transport rod is centered in the bore of a magnet, parallel to a set of co-axial pickup coils and to the applied magnet field. After the sample has been mounted, the sample space is cooled to 5 K in zero field. At 5 K a 1 mT field is applied. The sample transport rod is moved along the vertical axis of the magnet between the top and bottom pickup coils. As the sample is moved through the pickup coils, the magnetic dipole moment of the sample induces an electric current in the pickup coils. The SQUID (Superconducting QUantum Interference Device) portion of the magnetometer is essentially a highly linear current to voltage converter [48],[49]. Measurement continues every 0.1 K until the transition temperature is exceeded, as measured by the loss of diamagnetic shielding of the superconducting state.

The moment of the sample is determined by the annulus, which is superconducting at any temperature, which of course also includes the volume of the Sn-Cu core shielded by the superconductor. Assuming that the annulus is fully diamagnetic, its susceptibility will be

$$M / H = -1 / 4\pi \quad (5.1),$$

where M is the volume magnetization and H is the applied field. Neglecting the hexagonal symmetry of the Nb filaments, we approximate the superconducting annuli as right circular cylinders, permitting us to write the shielded volume as

$$V = \pi r_{sc+core}(T)^2 l \quad (5.2),$$

where l is the sample length and $r_{sc+core}(T)$ is the radial thickness of the superconductor and the shielded core at temperature T . As noted above, the core must be included, since the highest T_c layer lies right next to the core and thus shields the core up to the maximum T_c . Substituting 5.2 into 5.1, and expressing M in terms of the measured magnetic moment, m ($=MV$) gives

$$r_{sc+core} = 2 \times \sqrt{\frac{m}{Hl}} \text{ (cgs)}. \quad (5.3)$$

5.2. Quantum Design Physical Properties Measurement System – Heat Capacity

Heat capacity is defined as the amount of heat it takes to change the temperature.

Heat capacity can be expressed as

$$C = \frac{dQ}{dT}. \quad (5.4)$$

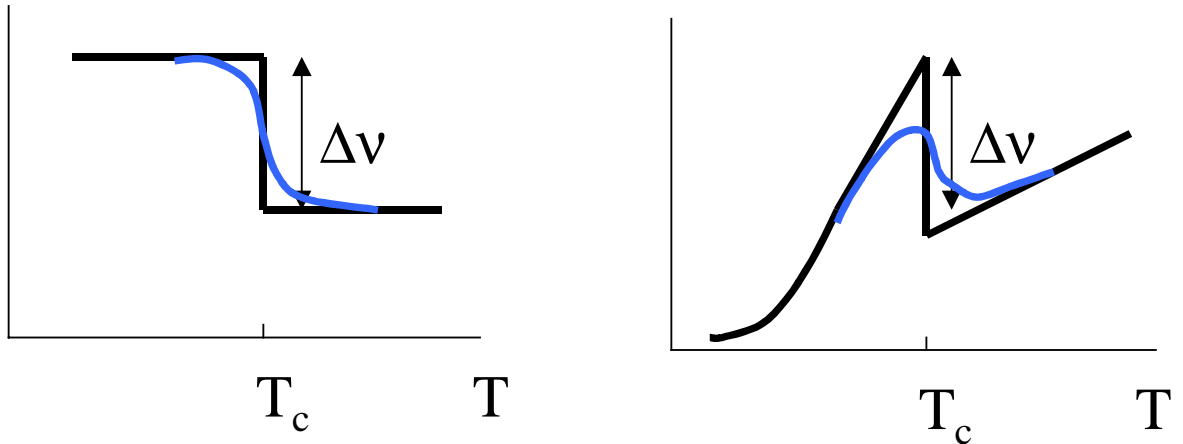


Fig. 5.1 The schematic diagram on the left represents a second order phase transition, for which the idealized curve is a step while the actual transition has some spread. The schematic diagram on the right represents the transition for a superconductor. The sharpness of the curve decreases as the superconductor becomes more inhomogeneous.

Generally heat capacity is measured at constant pressure. There are two contributions to the heat capacity, one from the electrons and the other from the lattice, phonons. The heat capacity then can be expressed as

$$C_p = C_p(\text{lattice}) + C_p(\text{electronic}) = K \left(\frac{T^3}{\theta} \right) + \gamma T \quad (5.5),$$

only at low temperatures ($T \ll \theta$, $\theta \sim 100\text{-}200$ K). Where K is a constant equal to 1940 J/mol-K, θ is the Debye temperature, and γ is the Sommerfeld constant. The lattice contribution is from the absorption of energy by the vibrational modes of the crystal and the electronic term is from absorption of energy by electrons at the Fermi surface [50]. $C_p \approx C_v$ at low temperatures and small coefficients of thermal expansion.

The superconducting phase transition that occurs at the critical temperature is a second-order phase transition. A second-order phase transition is characterized by the jump in the heat capacity at the critical temperature, Fig. 5.1 [51], and no latent heat of vaporization. A material that contains a distribution of critical temperatures will have a broad transition, while a material with a single critical temperature will have a sharp transition, Fig. 5.2.

For this thesis the heat capacity was measured using a Quantum Design PPMS [52]. The QD PPMS measures heat capacity by the relaxation method [52],[53]. In the relaxation method a known amount of heat is applied to the sample at constant power for a fixed time, providing a heating and cooling period of the same duration, during which the temperature of the sample is measured.

The sample is cut or ground down to a size which is suitable to fit on the sample puck, Fig. 5.3 [52]. Apiezon grease is applied to aid in the thermal conductance between the sample and the sample platform. Before performing a sample measurement, a measurement of the platform with just the Apiezon grease is performed. This is known as an addenda measurement. When a heat capacity measurement is taken with the sample on the platform, the total heat capacity of the sample, the sample platform, and the Apiezon grease, is obtained. The addenda is subtracted from the total heat capacity to obtain the sample's heat capacity.

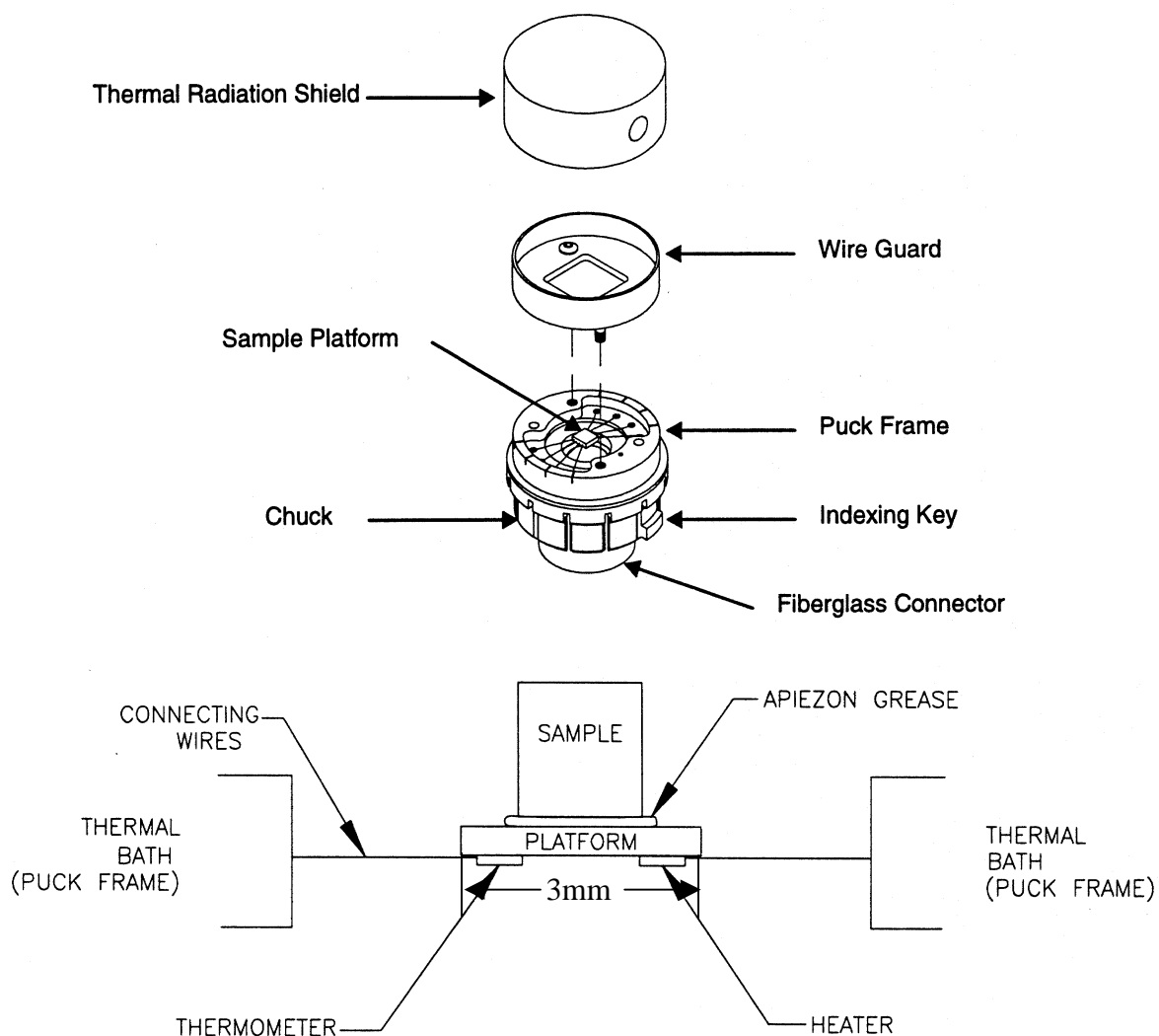


Fig. 5.3 Top figure is a diagram of the actual sample puck used for making heat capacity measurements in the Quantum Design PPMS. Bottom figure is a cross-sectional diagram of the sample puck. The platform is 3 mm on a side and the samples were usually less than 0.9mm tall.

The QD PPMS software uses two different models to analyze the data, the simple model and the two-tau model. The simple model assumes that the sample platform and the sample are in good thermal contact, and that both change temperature together, so that the temperature, T , as a function time, t , is determined by the heat flowing along the leads connecting the sample platform and the thermal sink of the puck frame

$$C_{\text{total}} \frac{dT}{dt} = -K_w(T-T_b) + P(t) \quad (5.6),$$

where C_{total} is the total heat capacity of the sample and sample platform, K_w is the thermal conductance of the supporting wires, T_b is the temperature of the puck frame (thermal bath), and $P(t)$ is the power supplied by the heater. The software applies the simple model to calculate the addenda and the total heat capacity of most samples. If the sample and sample platform are in poor contact, then the two-tau model is applied.

The two-tau model models the situation when the time constant for heat flowing between the sample and sample platform, and that of the leads are distinctly different. The following equations describe the two-tau model:

$$C_{\text{platform}} \frac{dT_p}{dt} = P(t) - K_w(T_p(t) - T_b) + K_g(T_s(t) - T_p(t)) \quad (5.7)$$

$$C_{\text{sample}} \frac{dT_s}{dt} = -K_g(T_s(t) - T_p(t)) \quad (5.8)$$

where C_{platform} is the heat capacity of the platform, C_{sample} , and K_g is the thermal conductance between the two due to the grease. The temperature of the sample platform is $T_p(t)$ and the sample is $T_s(t)$.

The software fits the data using a nonlinear, least squares algorithm. The system compares the solution of the simple model to the actual measurement. The values of the

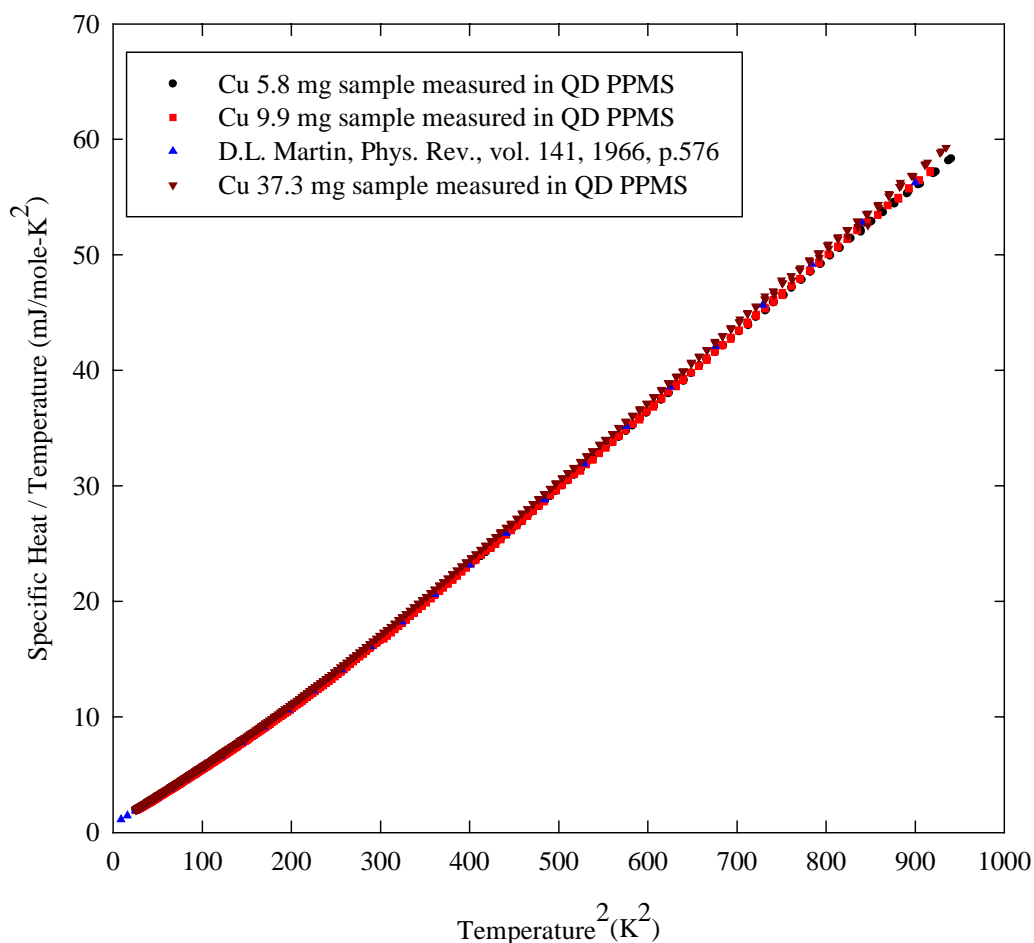


Fig. 5.4 Specific heat of Cu. Three of the samples were measured on the Quantum Design PPMS, each of these is a different mass, and the fourth is from [54].

parameters that give the smallest fit deviation determine the heat capacity. The sensitivity of the fit deviation to small variations in the fitting parameters is used to estimate the standard errors for the heat capacity. The error in the heat capacity is less than 1%. Except when measuring the addenda, a fit to two-tau model is also performed. The two-tau result is only used if its fit deviation is smaller than that of the simple model.

The specific heat of copper was measured using samples with a mass from 6-37 mg and with different addenda. The results are plotted in Fig. 5.4, together with literature [54]

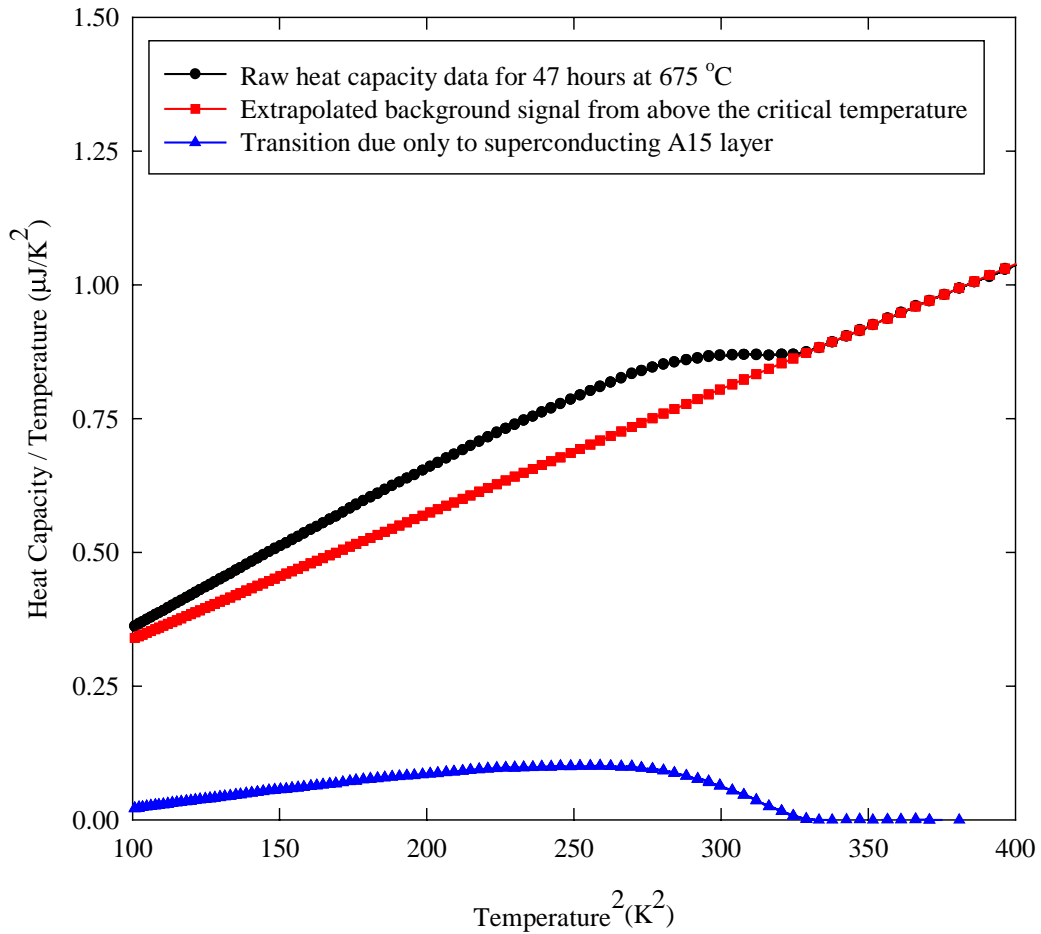


Fig. 5.5 The black curve is the raw heat capacity data for the SMI PIT conductor heat treated at 675 °C for 47 hours. The red curve is the linear extrapolation background signal. The blue curve is the heat capacity data for the A15 layer which results from the subtraction.

results. The measurements are in excellent agreement. At ~ 30 K the maximum difference between the literature value and the QD PPMS was $0.24 \text{ mJ/K}^2\text{-mole}$ and at 10K $0.05 \text{ mJ/K}^2\text{-mole}$. The critical temperature of a pure Nb sample was measured as a reference and the transition of this sample is shown in Fig. 5.2.

The first step in extracting the critical temperature transition due to the A15 phase is to subtract the heat capacity of all non-superconducting material contributing to the measurement, assuming the linearity of C/T vs. T^2 . This is done by subtracting the portion of

the heat capacity curve above the critical temperature from that below. What is left is the heat capacity due to only the superconducting Al₅ portion of the wire. This is shown graphically in Fig. 5.5.